SYNTHESIS AND ELECTRICAL CHARACTERISATION OF LANTHANUM DOPED BARIUM TITANATE ZIRCONATE

A thesis submitted to NIT Rourkela

in partial fulfillment of the requirement for the degree of

Doctor of Philosophy

In

Electrical Engineering

By

Malaya Saurava Dash

Department of Electrical Engineering

National Institute of Technology

Rourkela-769008, India

March 2009

To my parents with love

Acknowledgement

First of all, I would like to express my deep sense of respect and gratitude towards my guide **Prof (Dr) Saradindu Ghosh and Dr Japes Bera**, who have been the guiding force behind this work. I want to thank them for introducing me to the field of "Dielectrics and Insulation" and giving me the opportunity to work. I am greatly indebted to them for their constant encouragement and invaluable advice in every aspect of my academic life. Their presence and optimism have provided an invaluable influence on my career and outlook for the future I consider it my good fortune to have got an opportunity to work with such wonderful persons.

Next, I would like to express my respects to **Prof(Dr.) P. K. Nanda, Prof(Dr.) J. K. Satapathy and Prof(Dr.) S.K. Bhattacharya** for teaching me and also helping me how to learn. They have been great sources of inspiration to me and I thank them from the bottom of my heart.

I would like to thank all **faculty members** and **staff** of the Department of **Electrical** Engineering and **Ceramic** Engineering, N.I.T. Rourkela for their generous help in various ways for the completion of this thesis.

I would also like to mention the names of **Prof (Dr.) S. Adak, Dr. S. Pratihar** and **Dr. K. B. Mohanty** for helping me a lot during the thesis period.

I would like to thank my classmates, especially **Yugo, Rana, P.K. Kanungo and P. K. Roy** from whom I learned a lot and whose companionship I enjoyed so much during my stay at NIT, Rourkela.

I am especially indebted to my parents for their love, sacrifice, and support. They are my first teachers after I came to this world and have set great examples for me about how to live, study, and work.

Malaya Saurava Dash
Roll No: 50402003
Dept of EE, NIT, Rourkela

ABSTRACT

$BaTi_{0.6}Zr_{0.4}O_3$ powder was prepared from powders containing barium oxalate hydrate, zirconium oxy-hydroxide and titanium dioxide. Barium oxalate hydrate and zirconium oxy-hydroxide were precipitated from nitrate solution onto the surface of suspended TiO_2. Phase formation behaviour of the materials was extensively studied using XRD. $BaTiO_3$ (BT) and $BaZrO_3$ (BZ) start forming separately in the system upon calcinations in the temperature range 600–700^oC. BT-BZ solid solution then forms by diffusion of BT into BZ from 1050^oC onwards. The precursor completely transforms into $BaTi_{0.6}Zr_{0.4}O_3$ (BTZ) at 1200^oC for 2 hours calcinations. The activation energy of BT (134 kJ mol^{-1}) formation was found to be less than that of BZ (167.5 kJ mol^{-1}) formation. BTZ formation requires 503.6 kJ mol^{-1} of energy. The sintering kinetics of the powder was studied using thermal analyzer. The mean activation energy for sintering was found to be 550 kJ mol^{-1}.

Lanthanum doped $BaTi_{0.6}Zr_{0.4}O_3$ compositions $Ba_{1-x}La_xTi_{0.6[1-(5x/12)]}Zr_{0.4}O_3$, $Ba_{1-x}La_x(Ti_{0.6}Zr_{0.4[1-(5x/8)]})O_3$ and $Ba_{1-x}La_x(Ti_{0.6[1-x/4]}Zr_{0.4[1-x/4]})O_3$ with x = 0.005, 0.01, 0.02, 0.05 and 0.1 were synthesized. Perovskite phases were observed for all compositions without existence of any secondary phases. A gradual shift of diffraction peak to the higher angle with increasing lanthanum percentage reveals the contraction of perovskite lattice. The sintering behaviour was studied using thermal analyzer. Sinterability of the dielectrics decreases with increasing lanthanum substitution. The frequency dependence of dielectric permittivity and tan δ of the ceramics were investigated. It was found that both dielectric permittivity and tan δ decreases with increase in lanthanum percentage. Room temperature permittivity of lanthanum doped dielectrics was highly stable against change in frequency. The resistivity and current density were measured for the ceramics. It was noticed that resistivity decreases slightly at 0.5 atom % lanthanum substitution and then gradually increases with increasing the concentration. Dielectric measurements were carried on porous samples. It was noted that dielectric permittivity decreases and tan δ increases with increase in porosity.

The temperature dependence of dielectric permittivity and tan δ of lanthanum doped $BaTi_{0.6}Zr_{0.4}O_3$ samples has been investigated. The results show that the phase transition temperature T_m shifts towards low temperature with increasing La content. The dielectric response of the ceramics at various frequencies shows a diffuse phase transition around the transition temperature T_m. The degree of diffuseness of the phase transition implies the existence of a composition-induced diffuse phase transition of the ceramics where relatively large separation between maximum of real and imaginary parts of dielectric spectrum exist. The transition temperature T_m is moved toward higher temperatures with increasing frequency. A γ value of 1.89 from modified Curie-Weiss law implies diffuse phase transition behaviour of the ceramics and show relaxor-like behavior with a strong frequency dispersion of the T_m. The ceramics obey the empirical Vogel–Fulcher relation, which again confirms the relaxor behavior.

In recent years, significant progress has been achieved in the development of a class of artificial intelligent systems. This growing new class of technology has been applied successfully to a wide variety of applications. Artificial neural networks (ANNs) are relatively new computational tools and their inherent ability to learn and recognize highly non-linear and complex relationships makes them ideally suited in solving a wide range of complex real-world problems. Over the last decade chemistry became a field of their wide application. Nevertheless, few have been known of the application of ANN modeling technique in inorganic ceramic materials. The experimental results of undoped and lanthanum doped $BaTi_{0.6}Zr_{0.4}O_3$ were analyzed by back propagation (BP) network modeling. The combination of ANN parameters for best result in modeling was identified. The modeled values closely follow the experimental values suggesting the effectiveness of the proposed modeling and indicate that the ANN with BPA can be used for estimation of electrical properties of the dielectrics. Thus, ANN based modeling proved to be a very useful tool in dealing with problems encountered in dielectric ceramics.

CONTENTS

CHAPTER 3

SYNTHESIS AND CHARACTERISATION OF POWDER

CHAPTER 4

ELECTRICAL CHARACTERIZATION

LIST OF FIGURES

CHAPTER 1

INTRODUCTION AND BACKGROUND

1.1 Introduction

Ferroelectric materials, due to its properties, are used in many applications. Some of the applications include multilayer capacitor, ferroelectric memories, actuator, transducers, detectors, electro-optics, etc. Volumetric efficiencies with low cost make these materials, suitable for electronic and optics applications. It has been extensively used in ferroelectric memories like dynamic random access memory, static random access memory, ferroelectric random access memory etc. Electro-optic applications like wave guides, optical memory and displays, in general use ferroelectric materials. Again medical ultrasound, gas igniter, displacement transducers, accelerometer, impact printer pronounce its applications.

Recent interest in the field of ferroelectricity is highly centered on relaxors. These materials have wide range of applications in various devices like micro-electromechanical systems, actuators, capacitors, detectors and too many. Barium titanate zirconate, a relaxor ferroelectric, find applications in dynamic random access memories, field tunable device and actuators.

The intent of this chapter is to provide a brief description of ferroelectricity and relaxor behaviour in dielectrics.

1.2 Ferroelectricity and polarization

Ferroelectricity is a phenomenon which was discovered by Valasek in 1921[1]. Since then, many essential features of the ferroelectric phenomenon were studied and described. Rochelle salt ($NaKC_4H_4O_6 \cdot 4H_2O$) was the first material found to show ferroelectric properties, such as a reorientable spontaneous polarization (P_s), on cooling below a transition (Curie) temperature. In the ferroelectric phase, relative displacements of ions inside the unit cell results in reversible spontaneous dipole moments (Fig.1.1). The polarization (P) that arises due to dipoles is described by following equation;

$$P = \frac{qr}{V} \qquad (1.1)$$

where q is the electric charge on the displaced ion, r is the relative displacement, and V is the volume of the unit cell.

Fig.1.1. Dipole placed at distance **r**.

This moment is related to the electric displacement (D) as:

$$D = \chi_0 \chi E = \chi_0 E + P \qquad (1.2)$$

where χ_0 and χ are the free space and relative susceptibilities, E is electric field, respectively [2, 3].

1.3 Perovskite crystal structure and ferroelectricity

Most of the useful ferroelectrics, such as barium titanate, lead titanate ($PbTiO_3$), lead zirconate titanate, lead lanthanum zirconate titanate, and potassium niobate ($KNbO_3$) have the perovskite structure.

The perovskite, ABO_3 type structure consists of corner sharing oxygen octahedra (BO_6) arranged in three dimensions with smaller, highly charged cations (B: Ti^{4+}, Zr^{4+}, Sn^{4+}, Nb^{5+}, Ta^{5+}, W^{6+}, etc.) located in the middle of the octahedra and larger cations with smaller charge (A: Na^{+}, K^{+}, Ca^{2+}, Ba^{2+}, Pb^{2+}, etc.) in between the octahedra. The structure is shown in Fig.1.2. Most perovskite-type ferroelectrics are compounds with either $A^{2+}B^{4+}O_3^{\ 2-}$ or $A^{1+}B^{5+}O_3^{\ 2-}$ formula [4].

The perovskite structure can be also regarded as a close-packed arrangement of large A and O ions with smaller B ions filling the octahedral interstitial positions. The structure with cation substitution, may lead to more complex compounds, such as

$(K_{1/2}Bi_{1/2})TiO_3$, $Ba(Ti,Zr)O_3$, $Pb(Fe_{1/2}Ta_{1/2})O_3$, $Pb(Co_{1/4}Mn_{1/4}W_{1/2})O_3$, $Pb(Mg_{1/3}Nb_{2/3})O_3$, and $Pb(Zn_{1/3}Nb_{2/3})O_3$ [4, 5].

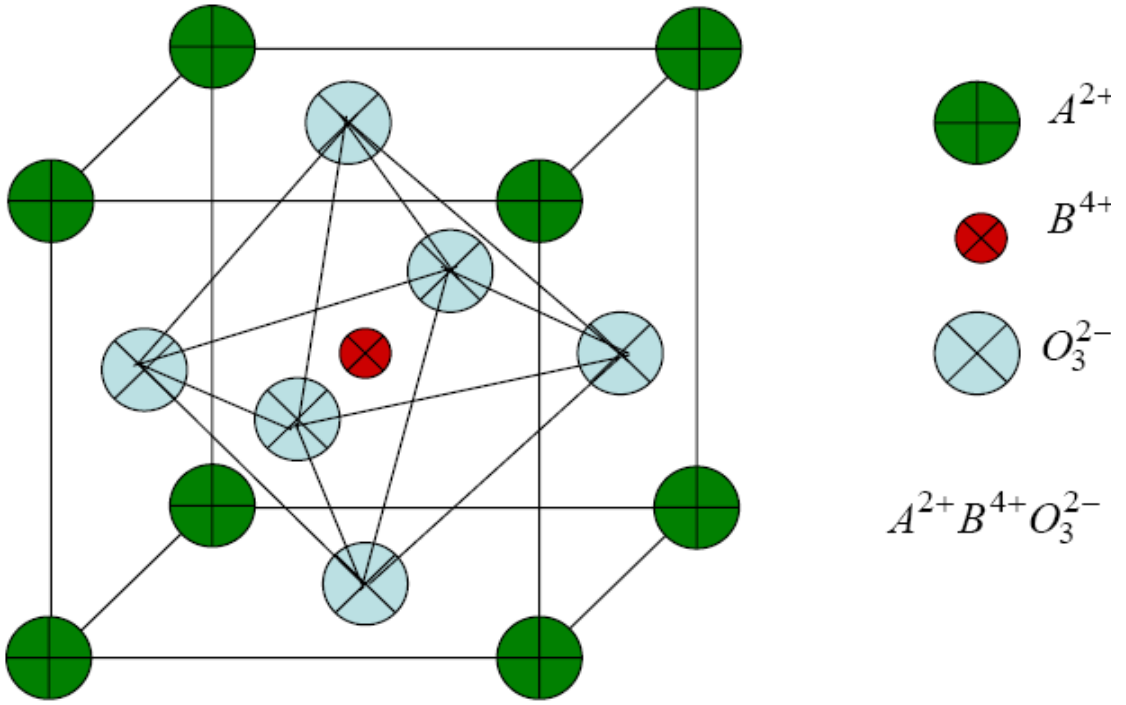

Fig.1.2. ABO_3 perovskite-type unit cell

Barium titanate ($BaTiO_3$) perovskite, the first ceramic material that exhibit ferroelectric behavior, was reported in 1945 [6]. Barium titanate became one of the most extensively studied ferroelectric materials due to its better ferroelectric properties, chemical and mechanical stability [7]. Above 120°C (Curie temperature, T_c), barium titanate has a cubic structure and possesses no spontaneous dipole due to its centro-symmetric structure. Below 120°C, it changes to a tetragonal phase, with an accompanying movement of Ti atoms inside the O_6 octahedra. The dipole moment may be considered to arise primarily due to the movement of Ti atoms with respect to the O atoms in the same plane, but the movement of the other O atoms (i.e. those O atoms above and below Ti atoms) and the Ba atoms are also relevant.

1.4 Ferroelectric phase transitions and Curie-Weiss law

On decreasing the temperature through the Curie point, a ferroelectric crystal undergoes a phase transition from a non-ferroelectric phase to a ferroelectric phase. The variation of the relative permittivity (ε_r) with temperature for $BaTiO_3$ ferroelectric crystal is shown in Fig.1.3. It shows that structure changes from paraelectric cubic phase to the ferroelectric tetragonal, orthorhombic, and rhombohedral phases. Near the phase transition temperatures, thermodynamic properties including dielectric, elastic, optical, and thermal constants show an anomalous behavior. Transition into a ferroelectric phase occurs differently in different type of ferroelectric materials. These transitions may be of first order or second order in classical ferroelectrics [7].

The temperature dependence of the relative permittivity above the Curie point ($T>T_c$) in most ferroelectrics is governed by the Curie-Weiss law [8]:

$$\varepsilon = \varepsilon_o + \frac{C}{(T - T_o)} \qquad (1.3)$$

where ε is the permittivity of the material, ε_0 is the permittivity of the vacuum, C is the curie constant and T_0 is the Curie-Weiss temperature. The Curie-Weiss temperature T_0 is, in general, different from the Curie point T_c. For first order transitions $T_0<T_c$, while for second order phase transitions $T_0=T_c$ [8, 9].

The order of the phase transition is defined by the discontinuity in the partial derivatives of the Gibbs free energy (G) of the ferroelectric at the phase transition temperature [10]. For an n^{th} order phase transition, the n^{th} order derivative of G is a discontinuous function at the transition temperature. Thus, spontaneous polarization and strain change continuously at the phase transition for a ferroelectric with the second order phase transition and are discontinuous at the phase transition temperature for first-order ferroelectrics. Schematic temperature dependence of the dielectric permittivity and spontaneous polarization (P_s) for first-order, second-order and relaxor ferroelectric is shown in Fig 1.4.

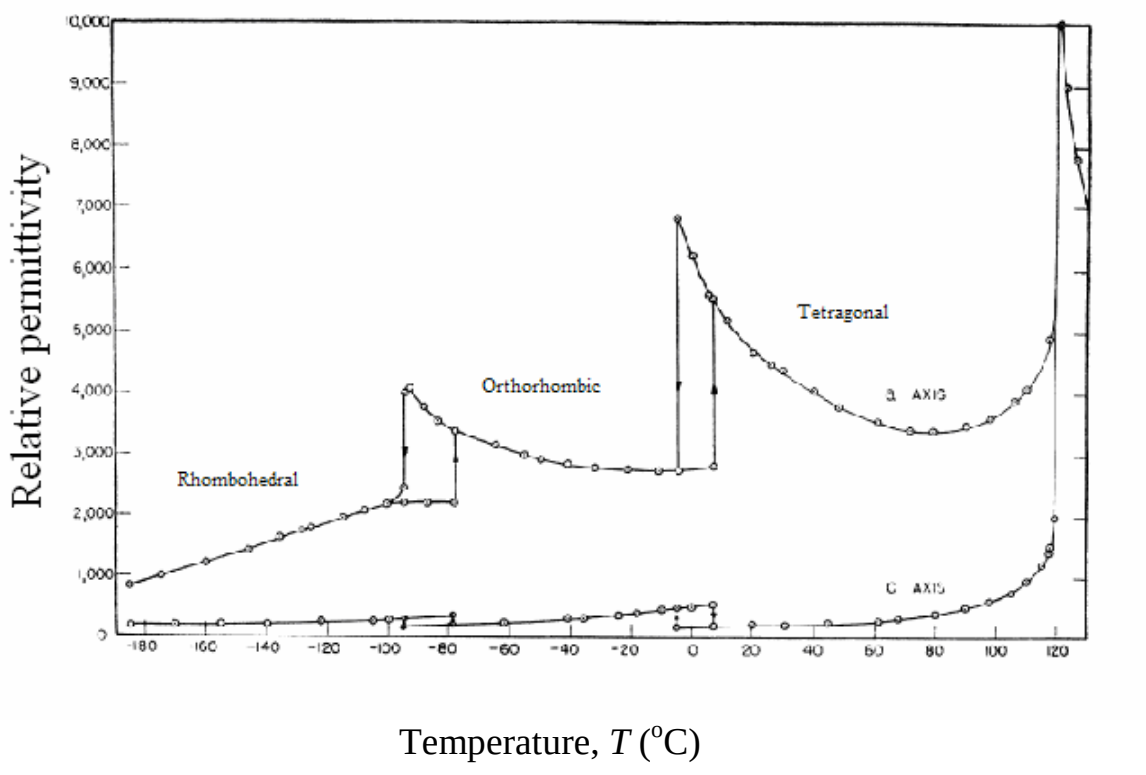

Fig.1.3. Relative permittivities measured along *a* and *c* directions of a poled tetragonal $BaTiO_3$ crystal versus temperature [11].

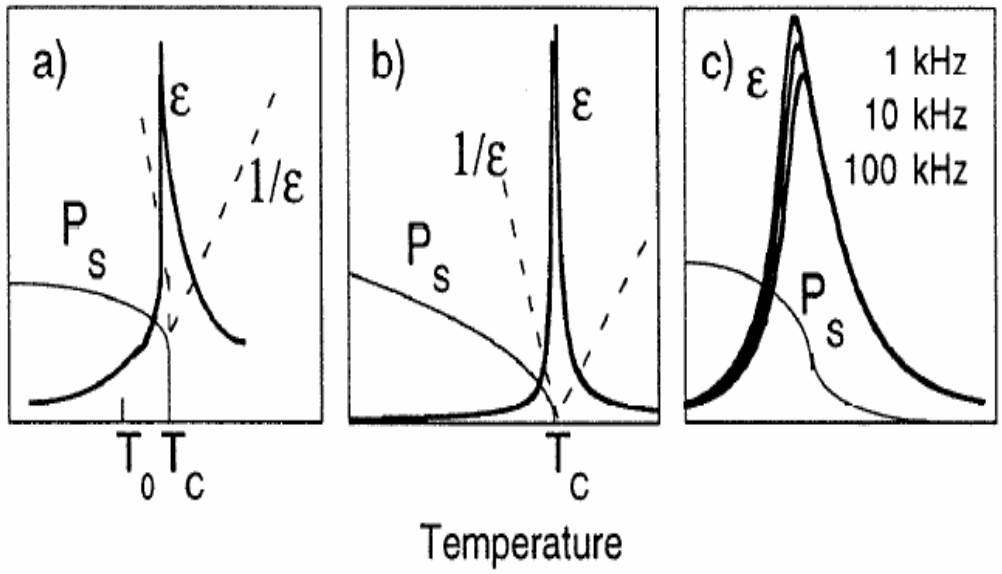

Fig.1.4. Temperature dependence of dielectric permittivity and spontaneous polarization for (a) first, (b) second and (c) relaxor ferroelectric [10].

1.5 Characteristics of relaxor ferroelectrics

Relaxor ferroelectrics can be distinguished from normal ferroelectrics by the presence of a broad, diffused, and dispersive phase transition on cooling over Curie temperature. The ferroelectric properties of relaxors are dependent on the measurement frequency. The temperature T_m at maximum ε_r, shifts to higher temperatures and that for dielectric loss shifts to lower temperature (Fig.1.5) with increasing frequency [12].

For relaxors, which have a diffuse phase transition, the remanent polarization (P_r) gradually decreases to zero on changing the temperature towards T_{max} [13]. There have been numerous theories proposed to explain the relaxor properties, such as compositional fluctuations model [12], super-paraelectricity model [14] and random local field model [15].

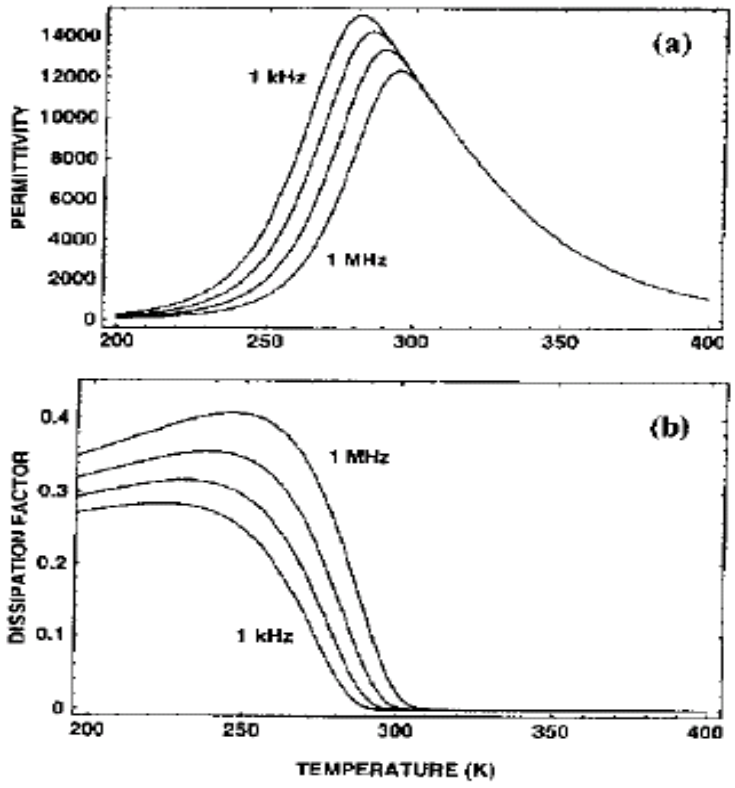

Fig.1.5. Variation of the dielectric properties of a relaxor ferroelectric with temperature at frequencies of 1KHz to 1MHz, (a) dielectric permittivity and (b) dissipation factor [12].

1.6 Structural origin of relaxor ferroelectrics

Relaxor ferroelectrics are a class of ferroelectrics that have a diffuse permittivity maximum which is frequency dependent. Lead magnesium niobate (PMN), Lead lanthanum titanate zirconate (PLTZ) and Lead zinc niobate (PZN), are some of the examples of relaxors. For many practical applications, a very broad permittivity maximum is desirable. Diffuseness can be achieved by making the material deliberately inhomogeneous. As shown in Fig.1.6, the permittivity of a ferroelectric with diffuse

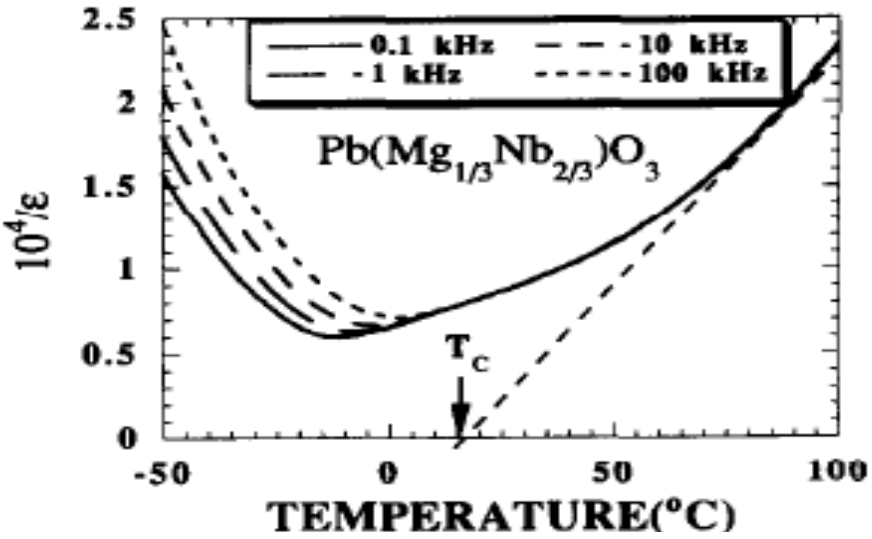

Fig.1.6. Temperature dependence of reciprocal permittivity of $Pb(Mg_{1/3}Nb_{2/3})O_3$ [12].

phase transition (DPT), does not follow the Curie-Weiss law above T_m. The extrapolated Curie-Weiss temperature (T_o) is necessarily higher than the temperature of the permittivity maximum T_m. Relaxors exhibit abnormally strong frequency dependence (dispersion) in the low temperature permittivity; to the extent that T_m is shifted upward with frequency. This is illustrated in Fig. 1.6 using data of $Pb(Mg_{l/3}N_{2/3})O_3$. A correspondingly dispersive behavior is also found in the dielectric loss, as expected from the Kramers- Kronig relations for the dielectric response. However, the peak temperature for dielectric loss does not coincide with T_m. Thus, understanding the origin of dispersion in relaxor is very much interesting and important.

Perovskites that contain *A*-site Pb cations with the general formula of $Pb(B_x'B_{1-x}'')O_3$ and $(Pb,La)(Zr_{1-x}Ti_x)O_3$ series figures prominently as the most widely used

relaxors. For Pb-containing perovskites, the strong Pb-O-*B"* coupling must be broken in order to render the material relaxant. This can be achieved by substitution of Pb^{2+} cation on the *A* -site or by the use of an oversized *B'* cation to attract Pb^{2+} cation away from the undersized *B"* cation.

In the phenomenological theory of ferroelectricity, there exists an energy barrier Φ_b between the un-polarized and polarized state. On an atomic level, ferroelectrically active *B"* cations in most, if not all, occupy off-centered sites even at temperatures well above T_c. In the polarized state, the energy degeneracy of bifurcated states is broken by the Lorentz field in the polarized region. In Fig.1.7(b) the energy of the field bias is denoted as *U* and the modified hopping barrier is denoted as V_o'. The relaxor behavior that shows both temperature diffuseness and frequency dispersion is possible only if V_o' is sufficiently small and broadly distributed. In addition, since all relaxors are solid solutions, *U* must be relatively large in order to effect hopping in this relatively random environment.

It turns out that the relative sizes of *B'* and *B"* have a profound effect on the Pb-O-*B"* coupling and the associated relaxor behavior in $Pb(B_x'B_{1-x}")O_3$. In the case, in which the *B'* cations are larger than the *B"* cations, then the six O^{2-} surrounding a *B'* cation are pushed outward. This has the consequence of decoupling Pb from the smaller *B"* ion. It is then possible for *B"* to have a lower V_o' and make such perovskites with oversized *B'* cations to be relaxors. This is indeed the case, for example, $Pb(In_{1/2},,Nb_{1/2})O_3$, $Pb(Zn_{1/3}Nb_{2/3})O_3$, $Pb(Co_{1/3}Nb_{2/3})O_3$ and $Pb(Ni_{l/3}Nb_{2/3})O_3$ are all relaxors [16]. On the other hand, if the *B'* cation is smaller in size than the *B"* cation, as in $Pb(Fe_{l/2}Nb_{1/2})O_3$, then Pb is attracted to the larger Nb, so the Pb-0-Nb coupling remains intact. Therefore, relaxor behavior is not expected. The requirement of a sufficiently small V_o' demands for *B"* cations be decoupled from Pb. It is only possible if Pb is attracted to an oversized *B'* cation. It has been noted that relaxors having *B"* cations decoupled from Pb, all lack long-range order.

Alloying also contribute inhomogeniety in the structure. All the *A*-site alloying, regardless of type (e.g. donor La^{3+}, acceptor Na^{+}) [17, 18] lowers T_m, and increases diffuseness and dispersion. This can be entirely attributed to the replacement of Pb which weakens both *U* and V_o' locally, while the random locations of Pb replacement broadens the energy spectra. This is termed as the *A*-site dilution effect. Alloying always reduces the relative fraction of each of the constituent phases in the total assemblage. However, large size difference between *B'* and *B"* destroys the random environment and the diffuse phase transition [19].

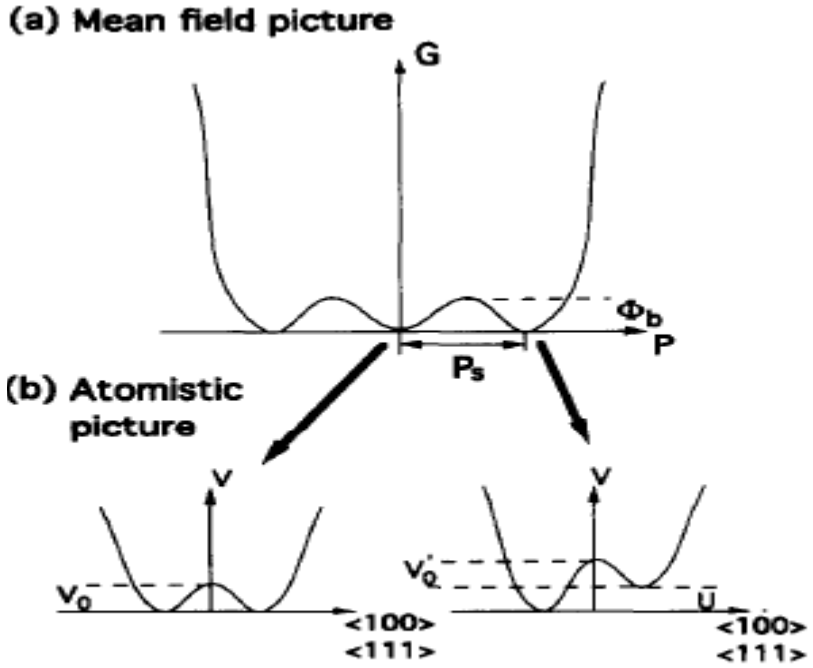

Fig.1.7. (a) Free energy V_s polarization in the phenomenological theory. (b) Local atomic potential along a line through two off-centered *B*-sites [19].

Lead free perovskite like $BaTi_{0.6}Z_{0.4}O_3$, also shows relaxor properties. A broad dielectric anomaly coupled with the shift of dielectric maxima towards a higher temperature with increasing frequency indicates the relaxor behaviour (Fig1.8) of this composition. The index of relaxation (γ) and broadening parameter (Δ) were estimated through linear fit of modified Curie-Weiss law and were found to be 1.79 and 76K

respectively. Again a remarkable good fit to the Vogel Fulcher relation further supports strong relaxor nature [20].

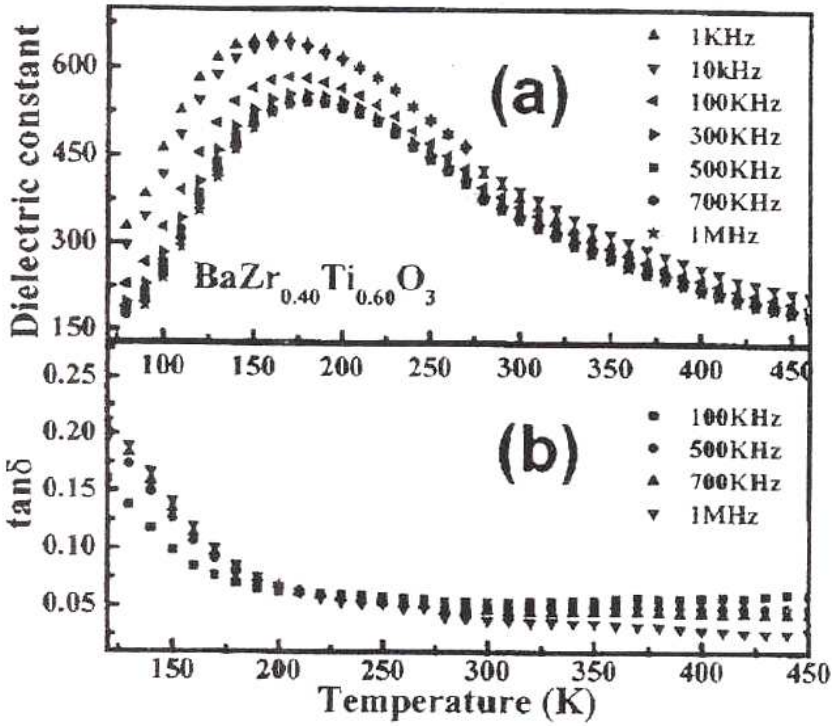

Fig.1.8. Temperature dependence (a) dielectric constant and (b) tan δ of $BaZr_{0.4}Ti_{0.6}O_3$ measured at different frequencies [20].

For the iso-valent substitutional *B*-site solid solutions in $BaTiZrO_3$ type perovskites, this is in good agreement with the fact that the dilution of ferroelectric character does not occur when the substitution Zr^{4+} for Ti^{4+} is weak. It is noted that, the size of Zr^{4+} is higher than that of Ti^{4+}. Introduction of over size Zr^{4+}, dilutes TiO_6 linkage. For small substitution rates, the richest Ti compositions, make possible the displacements of the cations and preserve the long-range spontaneous polarization. The strong quenching effect of Ti makes it difficult to allow relaxor behavior. However, at higher substitution rate, over a critical concentration, relaxor behavior is observed. Regarding the strong decreasing of T_c with increasing Zr, it is due to the larger size of Zr^{4+} than that of Ti^{4+}, entailing a decrease of its displacement in the octahedron [21, 22].

1.7 Organization of the thesis

The thesis has been divided into six chapters:

Chapter 1 presents a brief introduction of ferroelectricity, relaxor behaviour and organization of the thesis.

Chapter 2 deals with detailed literature review. Attempts have been made to systematically classify the available information under different sections. This chapter incorporates background information to assist in understanding the aims and results of this investigation, and also reviews recent reports by other investigators with which these results can be compared.

Chapter 3 enunciates with the detail of synthesis and powder characterization related to this research work.

Chapter 4 describes the electrical characterisation, which has been divided into four sections. First one speaks about the dielectric properties. Second section explains about the effect of porosity on the dielectric properties. Third section describes about the relaxor behaviour of lanthanum substituted $BaTi_{0.6}Zr_{0.4}O_3$. Fourth section narrates about the resistivity and current density characteristics at low electric field.

Chapter 5 elaborates about artificial neural network modeling and its application in predicting the dielectric properties of the ceramics.

Chapter 6 summarizes the concluding remarks and the scope of future work.

A complete list of references has been given towards the end of the thesis. Finally, a concise list of publications in peer reviewed international journals related to present research work has been presented at the end.

CHAPTER 2

LITERATURE REVIEW

2.1 Introduction

Barium titanate zirconate $Ba(Ti,Zr)O_3$ (abbreviated as BTZ) is one of the relaxor ferroelectrics used as base material for DRAM storage capacitors, decoupling capacitor, field tunable element, oscillators, filters, phase shifters etc [23-27]. Low dielectric loss and high breakdown strength make BTZ an efficient alternative to barium strontium titanate (BST) ceramics. Lead free relaxor materials would be particularly interesting for environmental-friendly applications [28]. Many researchers were interested in iso-valent or alio-valent substitutions in perovskite like BTZ, to alter its characteristics [29-31].

There are different synthesis procedures available in the literature for BTZ. Zirconium concentration plays an important role in the properties of BTZ. Porosity brings changes in the electrical properties of dielectrics. Artificial neural network application in different material characterization procedure will be of great interest.

In this chapter, an attempt is made to provide a review for the synthesis, effect of zirconium, lanthanum and porosity on the properties of BTZ ceramics.

2.2 Synthesis of $Ba(Ti,Zr)O_3$

Analytical grade $BaCO_3$, ZrO_2 and TiO_2 were used by Moura *et.al*. [32] to synthesize BTZ by solid state route. The powders were homogenized in a ball mill using isopropyl alcohol. After calcination, the powders were compacted in the form of pellets by isostatic pressing. The pellets were sintered at 1550^oC for 4h in static air.

The BTZ were prepared via conventional mixed-oxide method by Nanakorn *et.al.* [33]. The starting materials $BaCO_3$, TiO_2 and ZrO_2 were weighed based on the stoichiometric compositions of $Ba(Zr_xTi_{1-x})O_3$ with different x values. The weighed batches were ball-milled for 24h. After drying, the powders were calcined at temperatures ranging from 1150^oC to 1250^oC for 2h. The calcined powders were again ball-milled for

24h, dried and pressed into disks. The pellets were sintered at temperatures ranging from 1300^{o}C to 1450^{o}C for 2h.

The raw precursors used by Reymond *et.al* [34], include $BaCO_3$, ZrO_2 and TiO_2 powders. The powders were first mixed, ball milled and calcinated at 1200^{o}C for 15h, then pressed into disk and sintered for 4h at 1400^{o}C.

Tang *et.al* [26] prepared BTZ by taking weighted amounts of the appropriate proportions of high purity barium acetate, zirconium n-propoxide and titanium n-butoxide. Acetic acid and 2-methoxyethanol were selected as solvents. Barium acetate was dissolved in acetic acid, and the two alkoxides were dissolved in 2-methoxyethanol, respectively. By controlling the hydrolysis condition of the complex solution, a BTZ gel was formed. The dry gel was then annealed at 1100^{o}C for 5h in atmosphere. After grinding, BTZ powders were obtained. The powders were pressed into disks and sintered at 1400^{o}C for 5h.

BTZ was synthesized by Dixit *et.al* [35] from barium acetate, zirconium n-propoxide, and titanium isopropoxide. Stoichiometric amount of barium acetate was dissolved in warm acetic acid through continuous stirring. Ethylene glycol was added to the solution for complete dissolution of barium acetate in acetic acid. Inside a moisture-controlled glove box, stoichiometric amount of titanium isopropoxide and zirconium n-propoxide was co-dissolved and chelated with acetic acid. Finally, the Zr–Ti complex sol was added drop wise to barium acetate solution at room temperature with continuous stirring. Samples were calcined at 1100^{o}C for 2h in air for complete perovskite phase formation and better crystallinity. The high-temperature calcination was necessary, as at temperatures below 1100^{o}C, $BaCO_3$ and small amount of other undesirable phases (viz. $BaTi_2O_4$) were present.

[$Ba(CH_3COO)_2$], [$Zr(OC_3H_7)_4$], and [$Ti(OC_3H_7)_4$] were used as starting materials by Zhai *et.al.* [36] and acetic acid was used as solvent. Veith *et.al* [37] and Tang *et.al* [38] prepared $BaTiZrO_3$ ceramics by sol–gel processes.

BTZ were synthesized through the polymeric precursor method (PPM) by Marques *et.al*. [39]. Barium carbonate, titanium(IV) isopropoxide, zirconium(IV) tetra-n-butoxide, ethylene glycol and citric acid were used as starting materials. Titanium citrate and zirconium citrate were formed by the dissolution of, respectively, titanium(IV) isopropoxide and zirconium(IV) n-propoxide in water solutions of citric acid, under constant stirring. These solutions were homogenized and were mixed. The citrate solution was stirred for some hours at 60^{o}C to yield a clear and homogenous solution. Barium carbonate was dissolved in water, after then it was added in a stoichiometric quantity, to the titanium–zirconium citrate solution. After homogenization of the solution, ethylene glycol was added to promote the citrate polymerization by the polyesterification reaction. The citric acid ethylene glycol ratio was fixed at 60:40. The solution became more viscous with heating at around 80 – 90^{o}C.

High-purity $BaCl_2.2H_2O$, $ZrOCl_2.8H_2O$ and $TiCl_4$ were used as precursors by Reddy *et.al.* [40]. $TiCl_4$ was diluted with distilled water to avoid the precipitation during usage as it is highly hygroscopic and susceptible to precipitation of $Ti(OH)_4$ with atmospheric water at room temperature. The dilution procedure consists of adding the concentrated $TiCl_4$ slowly to the distilled water, which is kept close to freezing temperature, under the constant stirring conditions. This results in the diluted $TiCl_4$ solution, which needs to be used immediately as its shelf-life is only a few hours at room temperature. Equal molar concentration solutions of diluted $TiCl_4$ and $ZrOCl_2$ were mixed thoroughly and then, $BaCl_2$ solution added to this mixture. The mixing of these solutions was continued for 1h. NaOH with different molar concentrations was used for precipitation. NaOH solution was heated to 75^{o}C and pH is maintained at >12. The precursor solution mixture was added to NaOH at the rate of 25 ml/min and precipitated. The precipitate was immediately washed to remove the chloride ions and to neutralize the pH. The washed precipitate was dried at room temperature initially to confirm the phase formation and subsequently dried in an oven at 100^{o}C for 10h for quick drying.

Chemical co-precipitation method was used by Woo *et.al*. [41] to synthesize compositionally modified BTZ powders. A peroxo-complex solution of $BaZr_xTi_{1-x}$ was

prepared by adding hydrogen peroxide (H_2O_2) into mixed aqueous solution of $BaCl_2$, $ZrOCl_2$ and $TiCl_4$. The Ba/(Zr_xTi_{1-x}) andh_2O_2/(Zr_xTi_{1-x}) molar ratios were fixed. Amorphous $BaZr_xTi_{1-x}$ peroxo-hydroxide precipitate was formed by adding the peroxo-complex solution of $BaZr_xTi_{1-x}$ in an ammonium solution. The final pH of the solution was maintained at 12. The coprecipitated precursor was used as the starting material for the hydrothermal synthesis. In hydrothermal synthesis, the suspension including co-precipitated precursor was charged into a teflon-lined autoclave of 300 ml capacity with a fill factor of 80 vol. % in the presence of $Ba(OH)_2$. The $Ba(OH)_2$ was used as a mineralizer. The $Ba(OH)_2$/BTZ molar ratio was fixed at 2. The resulting pH in the aqueous solution obtained by addition of $Ba(OH)_2$ was 12.8. Subsequently, the reactor was heated to temperatures between 100 and 130^oC for various reaction times with autogeneous pressure. Maximum autogeneous pressure was 1.5 MPa at 130^oC. The reaction products were filtered and washed with distilled water to remove soluble components, including excess Ba^{2+} and Cl^- and then dried at 90^oC for 12h. The hydrothemally synthesized powders were pressed in the form of discs under a pressure of 80 MPa and sintered at 1150^oC for 1h.

2.3 Synthesis of La doped Ba(Ti,Zr)O_3

The starting material $BaCO_3$, TiO_2, La_2O_3 and ZrO_2 were used by Aliouane *et.al*. [30] to obtain $Ba_{1-x}La_{2x/3}(Ti_{1-y}Zr_y)O_3$ by conventional solid-state reaction route. The ceramics were processed from powders calcined for 12h at 1200^oC, then uniaxially pressed into disks. Finally, they were sintered for 2h at 1400^oC.

Similarly Chou *et.al*. [31] prepared samples by the conventional solid-state reaction method, using $BaCO_3$, ZrO_2, TiO_2 and La_2O_3. Powders of the composition $(Ba_{1-x}La_x)Zr_{0.2}Ti_{0.8-x/4}O_3$ were weighed and mixed for 24h using alcohol and zirconia milling media. After drying, the mixtures were calcined at 1300^oC for 4h. The obtained powders were pressed into disc-shaped pellets at 100 MPa. The green pellets were sintered at 1600^oC for 4h.

2.4 Effect of Zr in $Ba(Ti,Zr)O_3$

In perovskites, the relaxor behavior mainly occurs in lead-based compositions (PMN, PLZT, etc.), with more than one type of ions occupying the equivalent six-coordinated crystallographic sites [5]. Though the large family of lead-based perovskites and relaxors has shown a great potential, lead-free compositions in these families will be of interest because of the obvious environmental concern in the future.

Barium strontium titanate (BST) is ahigh-*K* (dielectric constant) material commonly used to replace silicon dioxide (SiO_2) as the dielectric in advanced memory devices. [26]. The high dielectric constant, high breakdown strength, low leakage current combined with low dissipation factor makes BST one of the promising candidates for dynamic random access memory (DRAM) applications [42]. In spite of this, BST does not provide good electrical properties at high electric field and loss is high.

Recently, BTZ has been chosen as an alternative to BST in the fabrication of ceramic capacitors, dynamic random access memories and tunable microwave devices. The solid solution of barium titanate $BaTiO_3$ and barium zirconate $BaZrO_3$, i.e., $Ba(Ti,Zr)O_3$, shows great similarity to the BST solid solution [43, 44]. In the para-electric state, just above the T_c, BTZ are attractive candidates for making dynamic random access memories and tunable dielectric devices. It provides high dielectric constant, low leakage current and low dielectric dispersion against frequency. While it is difficult to achieve high-quality Pb-based relaxor, $Ba(Ti,Zr)O_3$havehigher success in fulfilling those goals.

In general Zr^{4+} is chemically more stable than Ti^{4+} and has a larger ionic size to expand the perovskite lattice [24, 45-51]. It is believed that the conduction by electron hopping between Ti^{+4} and Ti^{+3} if any, would be supressed by substitution of Ti with Zr [27]. Zr content strongly influences the evolution of the microstructures that is homogeneous and crack-free [35]. Substitution of Ti^{4+} with Zr^{4+} exhibits several interesting features in the dielectric behavior of $BaTiO_3$ ceramics. The nature of the ferroelectric phase transition at the transition temperature (T_m) of BTZ bulk ceramics is known to change strongly with Zr content. The phase transition temperature (T_m) is

suppressed with increasing Zr content. When the Zr content is less than 10 at. %, the BTZ ceramics show normal ferroelectric behavior and the dielectric anomalies corresponding to the cubic to tetragonal (T_c), tetragonal to orthorhombic (T_2), and orthorhombic to rhombohedral (T_3) phases have been clearly observed [52]. For Zr contents of 8 at. %, the BTZ bulk ceramics show a broad permitivity-temperature (ε~T) curve near T_m, which is caused by the inhomogeneous distribution of Zr ions on Ti sites and mechanical stress in the grain [49].

As the Zr content increases, the phase transition temperatures approach each other, until at a Zr content of 20 at. %, only one phase transition exists [44]. BTZ with 20 at. % of Zr, shown a ferroelectric to paraelectric transition in the vicinity of room temperature. The degree of diffuseness of the phase transition is more pronounced for higher Zr content, implying the existence of a composition-induced diffuse phase transition of the ceramics with Zr from 20 to 35 at. %. At around 27 at. %, Zr-doped BTZ ceramics exhibit typical diffuse paraelectric to ferroelectric phase transition behavior, whereas Zr-richer compositions exhibit typical relaxor-like behavior in which T_c shifts to higher temperature with increase in frequency [52].high tunability and figure of merit for BTZ compositions makes the ceramics promising materials for tunable capacitor applications [26].

More importantly BTZ shows very stable and highly insulative characteristics against applied voltage without any sign of abrupt increase of leakage current or electrical breakdown [27].

2.5 Effect of La doping in $Ba(Ti,Zr)O_3$

For the stoichiometric compositions $Ba(Ti_{1-y}Zr_y)O_3$, in the well-known binary system $BaTiO_3$–$BaZrO_3$, the perovskite phase exists for $0<y<0.42$ [23]. Concerning the non-stoichiometric compositions, $(Ba_{1-x}La_{2x/3}\square_{x/3})(Ti_{1-y}Zr_y)O_3$, from defect chemistry viewpoint, the room temperature tetragonal symmetry was confirmed in $0<x<0.35$ and

$0<y<0.25$ [30]. In $(Ba_{0.95}La_{0.1/3})(Ti_{1-y}Zr_y)O_3$ for the smallest substitution in *A*-sites, associated with relatively small substitutions in *B*-sites ($0.05<y<0.15$), the temperature dependence of ε'_r at different frequencies exhibited no significant dispersion. This was not the case for the temperature dependence of ε''_r. Frequency dispersion was detected in the range of 10^2–10^5hz.however, for the two parts of dielectric permittivity, one single peak was observed and the temperature where the maximum of dielectric constant occurs was independent on frequencies. A very small deviation from the Curie–Weiss law was noticed. Such behaviour indicated a relatively diffuse phase transition; however the ferroelectric phase was not a relaxor. Upon further increasing substitutions in B-sites (y=0.20 and y=0.25), the frequency dispersion becomes stronger and was accompanied with a shifting of T_m to higher values for increasing frequencies. The value of the Curie temperature T_0 was greater than that of T_m. This behaviour characterizes a ferroelectric relaxor [30].

In $(Ba_{0.9}La_{0.2/3})(Ti_{1-y}Zr_y)O_3$, the temperature and frequency dependences of ε'_r and ε''_r exhibited only one phase transition. With increasing 'y', the ε'_r peak became more and more smooth and the frequency dispersion stronger. A deviation from the Curie–Weiss law was found. The value of T_m decreased when 'y' increased. The increasing degree of frequency dependence, which can be observed below T_m was in agreement with a relaxor behaviour [30]. In $(Ba_{1-x}La_{2x/3})(Ti_{1-y}Zr_y)O_3$ with $0.15<x<0.35$ and $0.05<y<0.35$, for higher composition ranges of x, the behaviour of the transition temperature was the same as that of the previous line (x=0.10), indicating clearly a relaxor behaviour. The strong frequency dispersion was observed particularly at the low-temperature slope of the peak of ε'_r [30].

Recently, the ferroelectric relaxor behavior and dielectric properties of $Ba_{1-x}La_xZr_{0.2}Ti_{0.8-x/4}O_3$ ceramics, with the Ti-vacancy defects compensation model, have been investigated by X. Chou *et.al* [31]. La^{3+} ions substitute for *A*-site Ba^{2+} ions to form solid solution and induce the occurrence of ferroelectric relaxor behavior. The temperature dependence dielectric constant and loss reveals that $Ba_{1-x}La_xZr_{0.2}Ti_{0.8-x/4}O_3$ ceramics have a typical relaxor behavior and diffuse phase transition characteristics and

the degree of ferroelectric relaxation behavior is enhanced with the increase of La dopant concentration. The Curie temperature (T_c) of $Ba_{1-x}La_xZr_{0.2}Ti_{0.8-x/4}O_3$ ceramics is remarkably shifted to lower temperature and the dielectric constant can be tailored from thousands to hundreds with the increase of Lanthanum. The dielectric loss of the ceramics is obviously improved by La doping.

2.6 Effect of porosity on the electrical properties

It is well known that the relative permittivity decreases with increasing porosity in polycrystalline ceramics. The porosity introduces in-homogeneity in bulk, which alters the mechanism of leakage [53]. The incorporation of pores significantly degrades the electrical characteristics and breakdown strength of the material. However, using various levels of porosity in order to alter the effective dielectric constant in the same material allows patterning different dielectric constants into a single material. Thus, controlling the porosity can yield a spectrum of dielectric constants from a single material [54]. Enhanced electric field in the pores increases the probability of bond breakage on the pore walls and leads to the lowering of the overall breakdown strength [53, 55].

2.7 Artificial neural network application

$BaTiO_3$ based materials are widely used as positive temperature coefficient resistance (PTCR) thermistors and as multilayer ceramic capacitors (MLCC) [56]. In order to satisfy different requirements and to enhance the dielectric performance of this kind of material, addition of different dopants is usually an effective way. However, because the dielectric properties of the material are very sensitive to the dopants and there may exist complex reciprocal actions between them, it is usually difficult to explain their functions in the system. The ever-increasing need to discover ceramic formulation with good electric properties requires considerable precise mathematical models in general. It would be intractable for us to develop a reliable modeling for the ceramic compounding without enough knowledge before doing the job by using conventional method. Computer modeling is becoming more and more important to scientists and engineers in allowing them a way to ‘‘picture’’ what might be happening. But very few are known of the use of artificial neural network (ANN) technique in ceramics although it is often

invoked in diverse areas in chemistry. As reviewed by Zupan *et.al*. [57], its application can improve, shorten, or bring new insight into old ways offhand ling experimental data.

For the last couple of years, extensive research works has been carried out on the application of neural network in various fields. As a result, the literature on neural network is growing very rapidly. Artificial neural network have been tried successfully on a very wide range of applications [58] including machine vision [59], speech processing [60, 61], sonar analysis [62], radar analysis [63], pattern recognition [64], robotic control [65] etc. In electrical power systems, artificial neural network have been used for accurate load forecasting [66-69], security evaluation [70, 71], capacitor control [72], alarm processing [73] etc. In high voltage systems, applications of neural network have been reported for pattern recognition of partial discharges [74, 75]. Other applications of neural network include pattern recognition and classification, voice and image processing, prediction [76], digital communications [77], and nonlinear system identification and control [78].

Artificial neural network has emerged as a highly effective tool suitable to perform non-linear, complex, and dynamic tasks with high degree of accuracy. This technique is endowed with certain unique attributes: the capability of universal approximation, the ability to learn from and to adapt to its environment, and the ability to invoke weak assumptions environment, and the ability to invoke weak assumptions generation of the input data. It is capable of learning complex input – output mappings from a set of training data and it has built-in capability to adapt to the changes in the environment [76].

Among the various neural network structures, the multilayer feed forward network is used for supervised learning. To determine the connection weights of the network, the back propagation algorithm [79] is employed in the training process. The convergence property of the learning process is affected by various network parameters.

Many problems such as classification, transformation, and modeling can be handled by this type of network. Abundant examples can be easily seen in subfields of

chemistry (analytical, organic, pharmaceutical and biochemistry) and chemical engineering, etc. However, very few literatures are available in the field of ceramics. Hechi-Nielsen *et.al.* [80]had proved in 1989 that a continuous function in closed interval can be approximated using a three-layer feed forward network with back propagation (BP) of errors. It does not require knowledge of the mathematical function known in advance.

2.8 Summary and scope of work

The solid state synthesis has advantages with respect to the use of relatively low-cost raw materials and simple processing steps. On the other hand, chemical solution methods produce more homogeneous, finer particle size and low impurity level powders. So, to get some of the benefits of the solid state and chemical route, a synthesis method in between the two routes may be adopted for economic production of the dielectrics.

Literature review shows that lanthanum substitutions enhances the relaxor properties and suppress the dielectric losses in ferroelectric ceramics. So, there is enough scope to study the effect of lanthanum substitution in BTZ ceramics.

Conventional ceramic processing of dielectrics leads to a porous body. The incorporation of pores significantly degrades the electrical characteristics of the dielectrics. Therefore, the study related to the effect of porosity on dielectric properties of BTZ ceramics will be of great interest for its practical applications.

Artificial neural network with back propagation learning has emerged as a highly effective technique suitable to perform non-linear, complex, and dynamic tasks with high degree of accuracy. It has been used in diverse areas of science and technology to predict the function, where equation describing the function is unknown. So, it will be interesting to apply artificial neural network technique in predicting electrical properties of BTZ ceramics.

2.9 Objectives of present work

Based on the review of literature, the objectives for the present investigations are listed as follows:

- Synthesis of Lanthanum doped $BaTi_{0.6}Zr_{0.4}O_3$ dielectrics through modified solid state route.
- Electrical characterization of Lanthanum modified $BaTi_{0.6}Zr_{0.4}O_{3.}$
- Study the diffuse phase transition and relaxor behaviour of modified dielectrics.
- Study the effect of porosity on the electrical properties.
- Apply artificial neural network technique to predict the dielectric properties.

CHAPTER 3

SYNTHESIS AND CHARACTERISATION OF POWDER

3.1 Introduction

The $BaTiO_3$–$BaZrO_3$ solid solutions were conventionally synthesized through solid state route [81-83]. Chemical solution methods are also used to produce more homogeneous, finer particle size and low impurity level powders than that produced by the solid state method [38, 84, 85]. Precursors like, barium acetate, zirconium propoxide and titanium n-butoxides, used in chemical route, are relatively costlier and the chemical method is more complex. On the other hand, the solid state synthesis has advantages with respect to the use of relatively low-cost raw materials and simple processing steps. In the present synthesis $Ba(NO_3)_2$, $ZrOCl_2.8H_2O$, TiO_2 and La_2O_3 (In case of La doped BTZ), powders are used for the preparation of BTZ and La doped BTZ to get some of the benefits of both solid state and chemical route. Use of TiO_2 powder, instead of its organometallic salt, can effectively reduce the powder synthesis cost. This type of powder synthesis has been reported earlier in the literature especially for $SrTiO_3$ and $BaTiO_3$ [86, 87].

3.2 $Ba(Ti_{0.6}Zr_{0.4})O_3$

Aqueous solution of $Ba(NO_3)_2$ and $ZrOCl_2.8H_2O$ are used to precipitate barium oxalate hydrate and zirconium oxy-hydroxide onto the surface of suspended TiO_2 particles, to get more homogeneous mixing of raw materials than that obtained in solid powder mixing. Reports on BTZ formation from barium oxalate hydrate, titanium dioxide and zirconium oxy-hydroxide precursor mixture is not available in the literature. In the present work, the $Ba(Ti_{0.6}Zr_{0.4})O_3$ powder was synthesized from the precursor containing solution precipitated barium oxalate hydrate, zirconium oxy-hydroxide and TiO_2. The decomposition behavior of precursor was investigated. The BTZ solid solution formation mechanism and its kinetics were studied. Finally, the sintering kinetics of the powder was investigated.

3.2.1 Experimental procedure

Powder synthesis: Analytical grade barium nitrate ($Ba(NO_3)_2$), titanium dioxide (TiO_2), zirconium oxy-chloride ($ZrOCl_2.8H_2O$), ammonia (NH_4OH) and oxalic acid ($(COOH)_2.2H_2O$) were used as raw materials in this process. All the chemicals were from Merck, India (GR grade with 99% purity). To prepare 20gm $Ba(Ti_{0.6}Zr_{0.4})O_3$, 0.0798 mol of barium nitrate, 0.0478 mol of titanium dioxide, 0.0319 mol of zirconium oxy-chloride and 0.08 mol of oxalic acid were taken.

An aqueous solution of 0.12 M barium nitrate was prepared using de-ionized water in a glass beaker. The exact molar concentration of the solution was determined by the chemical analysis. Required amount of $ZrOCl_2.8H_2O$ was dissolved in the above barium nitrate solution with constant stirring. Appropriate amount of TiO_2 was added to 0.15 M oxalic acid solution with continuous stirring to form a suspension. The suspension was treated in ultrasonic bath for 10 min to break soft agglomerates. The solution containing barium nitrate and zirconium oxy-chloride was added drop-wise into the suspension of TiO_2 in oxalic acid solution under vigorous stirring. Finally, the pH of the resultant mixture was adjusted to 8 by adding ammonia solution. This process precipitates barium oxalate hydrate and $ZrO(OH)_2$ on the surface of TiO_2 (acting as seed) particles by heterogeneous nucleation. It is well known that heterogeneous nucleation is used in coating of ceramic particles with another ceramics. The necessary condition is that the super-saturation must be controlled so that only heterogeneous nucleation on the seed takes place. If super-saturation is too high, homogeneous nucleation may take place [88]. In the present case super-saturation was suppressed and controlled by the use of dilute solutions.

The resulting precipitate was filtered out and then washed repeatedly using deionized water followed by isopropyl alcohol. The precipitate was dried at 50^oC for 24 h in an oven. The filtrate solution was chemically analyzed to find out the presence of Ba^{+2} and Zr^{+4} ions. No evidences of their presence were identified within the limit of chemical analysis. For Ba^{+2} ions, the filtrate was titrated by standard EDTA solution after mixing with few ml of NH_4Cl-NH_4OH buffer and solochrome-black-T indicator. For Zr^{+4}, first

the filtrate was concentrated by boiling and then phosphoric acid was added. No precipitate of ZrP_2O_7 was found.

Decomposition behaviour: The dried powder was characterized by differential scanning calorymetry (DSC) and thermo gravimetric (TG) analysis using NETZSCH STA, Model No 409 C, in air atmosphere with the heating rate of 10^oC/min.

DSC is a thermo analytical technique in which the difference in the amount of heat required to increase the temperature of a sample with respect to reference (here Al_2O_3) are measured as a function of temperature and time. When a material undergoes physical or chemical change it absorbs or releases thermal energy. Exothermic or endothermic changes are shown in opposite directions in DSC graph. This technique is excellent for determining the presence and quantity of hydrated water and gives an idea about decomposition behavior, phase transitions, formation of products, etc.

TGA is a simple analytical technique that measures the weight loss (or weight gain) of a material as a function of temperature. As materials are heated, they can lose weight due to drying, or by decomposition reactions that liberate gasses. Some materials can gain weight by reacting with the atmospheric gases in the testing environment.

Phase and crystallite size analysis: Phase content of precursor and phase formation behaviour in calcined precursor samples were analysed by the powder x-ray diffraction performed with a Philips diffractometer (model: PW-1830, Philips, Netherlands). For quantification of the diffracted x-rays, an electronic detector is placed on the other side of the sample from the x-ray tube, and the sample is rotated through different Bragg's angles. The goniometer keeps track of the angle, and the detector records the x-rays in units of counts/sec and sends this information to the computer. The operating parameters were; 40 kV and 35 mA with the Cu target, a step size of 0.02 (degree) and a count time of 4 s per step. After scan of the sample, the x-ray intensity (counts/sec) was plotted against the angle two-theta (2θ). The angle (2θ) for each diffraction peak was then converted to d-spacing, using the Bragg equation.

The identification of different phases was carried out by Hanawalt method using Philips high score software. The powder pattern is characterized by a set of line position 2θ and a set of relative line intensities I. But the angular positions of the lines depend on the wavelength used, and a more fundamental quantity is the spacing d of the lattice planes forming each line. Each pattern is described by listing the d and I values of its diffraction lines. Each substance is characterized by the d values of its 3 strongest lines. The d values together with the relative intensities are sufficient to characterize the pattern of an unknown.

The crystallite sizes of the precursor and calcined powder samples were determined from x-ray line broadening using the equation as follows:

$$t = \frac{0.9\lambda}{BCos\theta} \tag{3.1}$$

Where, t is the crystallite size, λ is the wavelength of the radiation, θ is the Bragg's angle and B is the full width at half maximum. Line broadening due to instrument was subtracted from the peak width before calculating the crystallite size using the following formula:

$$B^2 = B^2_{meas} - B^2_{equip} \tag{3.2}$$

Where, B_{meas} = measured full width at half maximum from peak, B_{equip}= instrumental broadening [Standard silicon sample was used, whose B value was 0.09821 at 2θ= 29° for (111) reflection].

Lattice parameters were determined using following relationship for cubic structure:

$$a^2 = \frac{[\lambda^2(h^2 + k^2 + l^2)]}{4[Sin^2\theta]} \tag{3.3}$$

Where, a is lattice parameter, λ is the wavelength of the radiation, θ is the Bragg's angle and (hkl) is Miller index.

Densification study: Densification kinetics of compact samples was investigated by NETZSCH dilatometer model DIL 402 C. In the dilatometer, the specimen is kept in a specimen holder in the centre of the furnace. The linear dimensional change i.e. shrinkage or expansion of the specimen is transmitted through the push rod (pressed against the sample inside the furnace) to the measuring head. The linear variable differential transducer (LVDT) details the change in length and produces an analogue signal through a measuring amplifier. The digitally displayed signal is in analogue form on a recorder.

The calcined powder was ball milled for 24 hours inside polyethylene jar using zirconia balls and acetone as medium. The milled powder was dried at 50^{o}C. The dried powder was then mixed with 0.5 wt.% PVA. The powder was then granulated by sieving and the granules were uniaxially pressed to square rods at 3.5 ton pressure by cold isostatic pressing. The rod sample was having width and breadth of 5mm and length of 20mm. The measurement was carried out from room temperature to 1300^{o}C at different heating rates; 5, 10, 15^{o}C per minute in air atmosphere.

3.2.2 Results and discussion

Decomposition behaviour: The decomposition behavior of precursor was characterized using thermo-gravimetric (TG) analysis and differential scanning calorimetry (DSC) from room temperature up to 1300^{o}C. Fig.3.1 shows the DSC-TG tracing of the precursor as a function of temperature. TG graph shows the weight loss in various stages. The first major weight loss of about 2.9% within the temperature range 100-300^{o}C, corresponds to an endothermic reaction in the DSC curve. This weight loss may be attributed to the decomposition of $BaC_2O_4.xH_2O$ to BaC_2O_4.

The second weight loss of about 2.4% appearing in the temperature range 300-425^{o}C, corresponds to a small endothermic reaction in the DSC curve. This weight loss may be attributed to the dehydration of $ZrO(OH)_2$ to ZrO_2. The third major weight loss of about 8.7% is found in the temperature range 425-600^{o}C, which corresponds to an exothermic reaction in the DSC curve. This weight loss may be attributed to the decomposition of barium oxalate to barium carbonate as per the reactions:

$$BaC_2O_4 \longrightarrow BaCO_3+CO \quad (3.4)$$

$$2CO+O_2 \longrightarrow 2CO_2 \quad (3.5)$$

Reaction (3.4) is an endothermic one. However, at the same time CO is converted exothermically to CO_2, taking oxygen from air. The huge exothermic peak appears at 508^{o}C is due to the reaction (3.5), which suppresses the endothermic peak of reaction (3.4). A sharp endothermic peak at 811^{o}C corresponds to the polymorphic transformation of whitrite to α-$BaCO_3$ [81]. The fourth major weight loss of about 14%, started from around 700^{o}C, is due to the decomposition of $BaCO_3$ and formation of BT and BZ. The figure also shows that the $BaCO_3$ decomposition completed up to 1000^{o}C. However, in pure $BaCO_3$ the decomposition peak occurs at about 1187^{o}C. This indicates that $BaCO_3$, which formed intermediately in the precursor, decomposes at lower temperature due to the presence of acidic TiO_2, fine particle size and better homogeneity in the mixture [87].

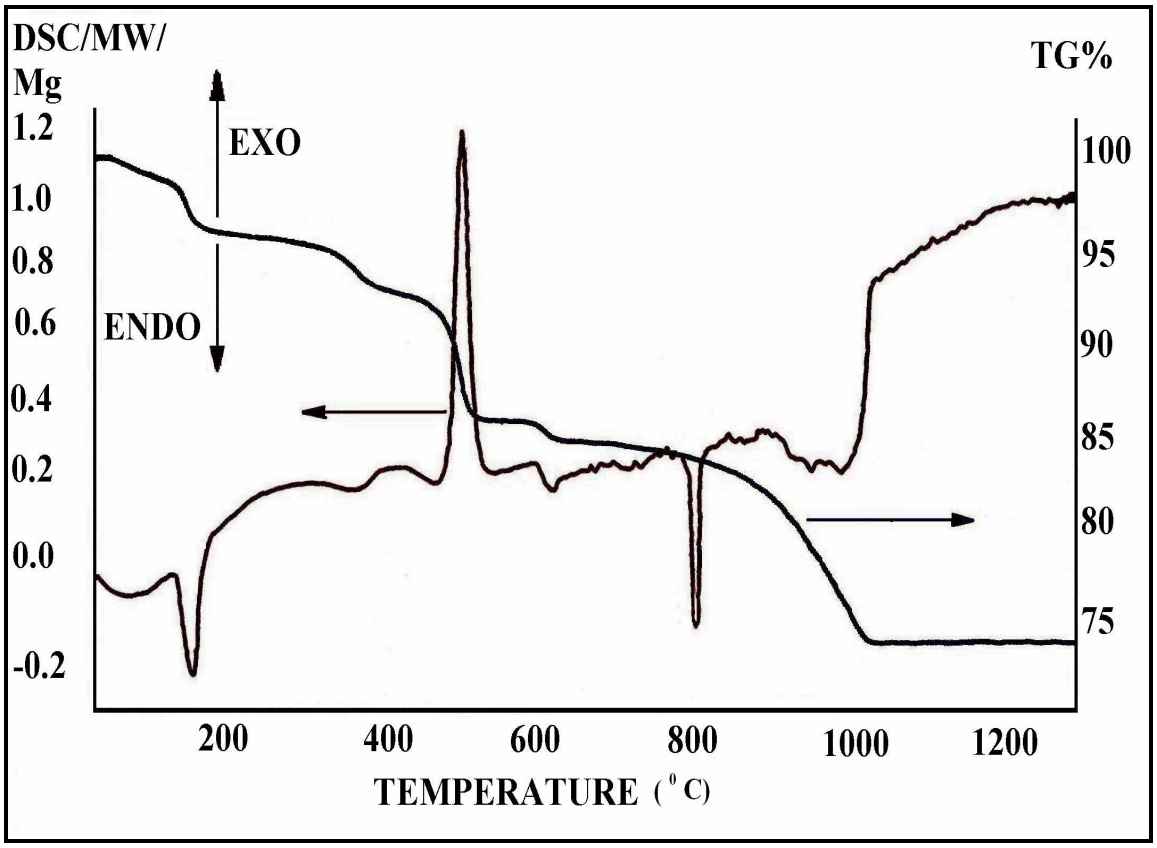

Fig.3.1. DSC-TG tracing of precursor powder for $Ba(Ti_{0.6}Zr_{0.4})O_3$ synthesis.

To understand the fundamental issues of BTZ formation, the precursors were heated in air at different temperatures and then were analyzed by XRD. Fig. 3.2 shows the XRD patterns of the precursor heated at different temperatures. The analysis of raw powder shows the presence of $BaC_2O_4.0.5H_2O$ (PDF No. 20-0134) and TiO_2 (Fig. 3.2(a)). The presence of $ZrO_2C_2O_4.xH_2O$ type phases in the precursor had not been detected within the limit of XRD. $BaC_2O_4.0.5H_2O$ was converted to BaC_2O_4 (PDF No. 37-0674) upon calcinations at 400^{o}C (Fig. 3.2(b)). This confirms the first weight loss in TG analysis is due to the loss of crystalline water of barium oxalate hydrate. The presence of $ZrO(OH)_2$ as well as ZrO_2 was not detected by XRD analysis. It is supposed that both of them remain in amorphous state. The 700^{o}C calcined precursor shows the presence of $BaCO_3$ and TiO_2. The material in the final product (1200^{o}C/2h) was identified (Fig. 3.2(d)) as BTZ by comparing with standard pattern for $Ba(Ti_{0.75}Zr_{0.25})O_3$ (PDF No. 36-0019).

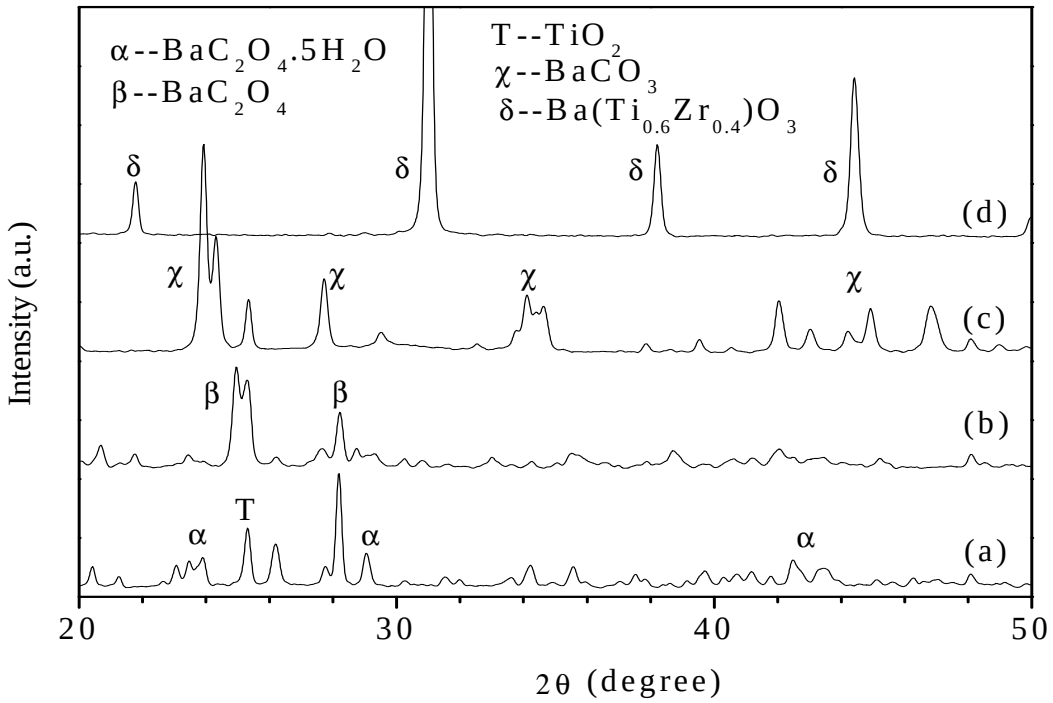

Fig.3.2. XRD pattern of (a) precursor powder and precursor calcined at (b) 400^{o}C, (c) 700^{o}C, (d) 1200^{o}C.

Phase transformation behaviour and kinetics: To study the phase transformation behavior and reaction kinetics, the precursor powder was calcined at different temperatures for 2 hours. Fig. 3.3 shows the XRD pattern of calcined product, which suggests that BT and BZ form separately in the system and then BTZ forms by inter-diffusion between BT and BZ. Slow step scanning XRD analysis reveals that BT and BZ starts forming simultaneously in the temperature range 600^{o}C-700^{o}C by the reaction:

$$2BaCO_3(s) + ZrO_2(s) + TiO_2(s) = BaTiO_3(s) + BaZrO_3(s) + 2CO_2(g) \qquad (3.6)$$

Formation of intermediate BaO or other phases, like Ba_2ZrO_4, Ba_2TiO_4 or $BaTi_3O_7$ had not been observed within the detection limit of XRD. The precursor was completely transformed into single phase, cubic structure BTZ at 1200^{o}C for 2h calcinations.

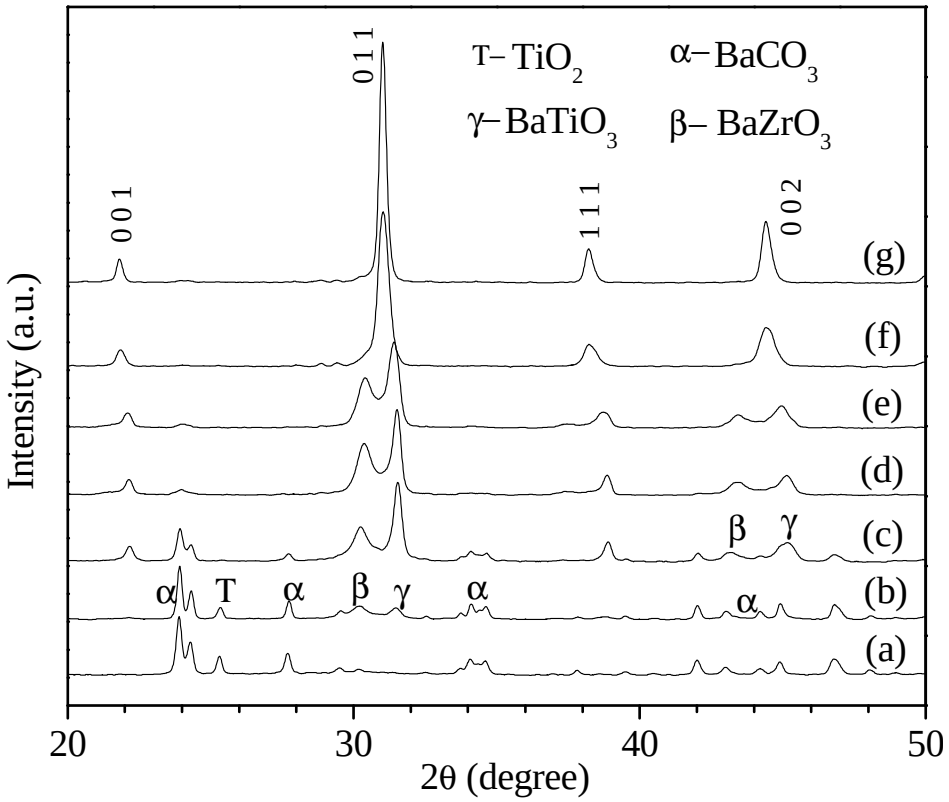

Fig.3.3. XRD patterns of precursor powder calcined for 2h at (a) 600^{o}C, (b) 700^{o}C, (c) 800^{o}C, (d) 900^{o}C, (e) 1100^{o}C, (f) 1200^{o}C and (g) for16h at 1200^{o}C.

For quantitative estimation of phases, the calcined powders were uniformly mixed with an internal standard and the resulting mixture was analyzed by XRD. The relative weight fractions were quantified from the ratio of peak areas, according to the process described by S. Kumar *et.al.* [89]. The variation of phase content with calcinations temperatures is presented in Fig. 3.4. As may be seen from the figure, the rate of decomposition of barium carbonate is higher in the temperature range 600^{o}C-800^{o}C. It also shows that the amount of BZ formation is less than that of BT at initial stage. This may be due to the higher reactivity of $BaCO_3$ with TiO_2, as Ti is more electronegative than Zr. At the later stage (850^{o}C–1000^{o}C), the amount of BZ formation exceeds that of BT, which is in contrast to the result reported earlier for the mixed oxide route BTZ synthesis [81]. The reason behind this is (a) high reactivity of very fine homogeneously mixed ZrO_2 particles as it was formed through solution precipitation, de-hydroxylation

and (b) finishing of the lower size particle fraction of TiO_2 in the mixture. However, the rate of BT formation increases rapidly above 1000^{o}C. The amount of BZ decreases slightly at 1050^{o}C, which may be due to the formation of BTZ. The BTZ starts forming from 1050^{o}C onwards. The amount of BT and BZ decreases sharply above 1100^{o}C and formation of BTZ increases rapidly due to inter diffusion reaction between BT and BZ.

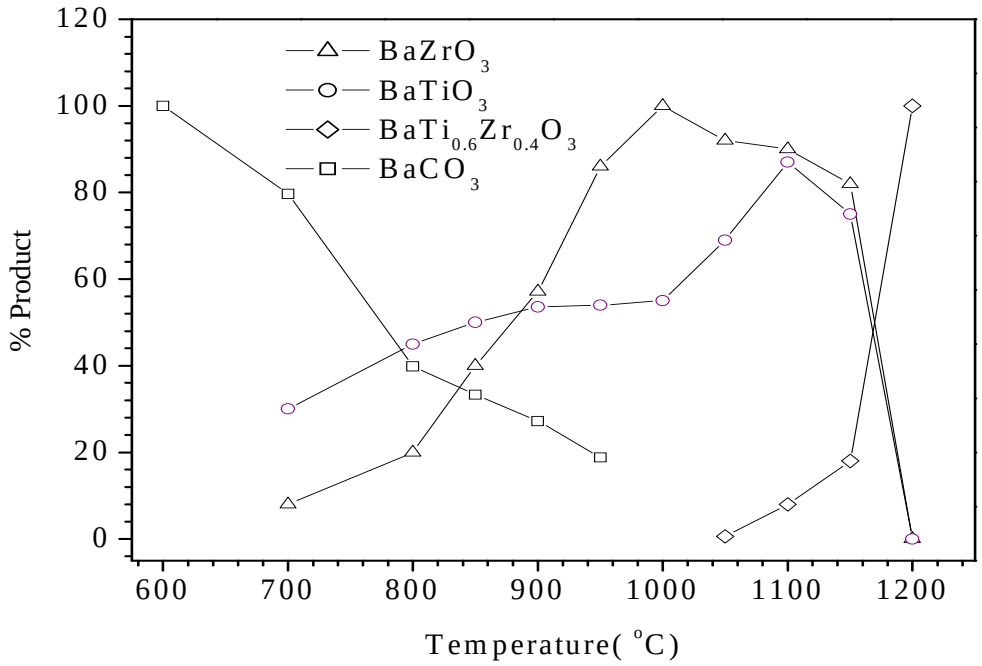

Fig.3.4. Non-isothermal transformation kinetics of precursor in static air.

This powder synthesis is a route in between conventional solid state and chemical synthesis. So the route is expected to produce powder better than solid-state route and the results are in accordance with this. A comparison with [81], reported that BTZ was formed at 1500^{o}C-1550^{o}C for 1 hour calcinations where as in this case it was formed at 1200^{o}C for 2 hours. About 90% of BT and BZ are formed at about 1300^{o}C for solid state route but here 90% BZ is formed at 1000^{o}C and that of BT at 1100^{o}C. So it indicates that the phase formation was better for the present synthesis route. Compared with chemical route, the calcinations temperature for phase formation by this route (1200^{o}C for 2h) is slightly higher than, for example, 1100^{o}C for 5 h that reported for sol-gel synthesis of BTZ [26].

To check the phase formation kinetics, the concentrations of phases were used to measure the activation energy for their formation using the following relationship [90]:

$$k = \left(\frac{2.303}{t}\right)\log\left(\frac{a}{a-x}\right) \tag{3.7}$$

where k is the velocity constant of first order reaction, t is the time in second, a is the initial concentration and x is the concentration after time t. The activation energy (Q) for different phase formation reactions were derived using:

$$\log k = \left(\frac{-Q}{2.303R}\right)\frac{1}{T} + \log A \tag{3.8}$$

where T is the temperature in Kelvin, and A is a constant called the frequency factor. Log k versus $1/T$, plot as shown in Fig. 3.5, represents Arrhenius type dependency of reaction rate on calcinations temperature for BT, BZ and BTZ formation. It shows that BT formation requires less activation energy 134 KJ mol^{-1} in the temperature range 950^{o}C to 1100^{o}C, than that of BZ formation (167.5 KJ mol^{-1} in range 800^{o}C to 1000^{o}C). BT formation activation energy in the temperature range 700^{o}C to 950^{o}C is not evaluated here due to its temporary slow down in formation kinetics.

Phases were formed in this system through inter-diffusion between different particles. Inter-diffusions take place with different ions limiting the speed of diffusion. The phase formation reactions may be limited by the diffusion of Ti for BT and Zr for BZ formation, respectively. In this case, Ba and O are assumed to be immobile because their concentrations are spatially invariant. That is, two reactions are occurring in the same environment of $BaCO_3$. Since BT and BZ are formed by reacting respective constituents with $BaCO_3$, which is uniformly distributed in the precursor mixture, effect of Ba and O on the phase formation of BT and BZ is considered to be equivalent and hence neglected. Since, Zr^{4+} has higher ionic radius than Ti^{4+}, its diffusion requires higher energy to form perovskite phase. BTZ solid solution formation requires much higher activation energy 503.6 KJ mol^{-1}. However, that is less than 556.8 KJ mol^{-1} reported earlier by J. Bera *et. al.* [81], for solid-state synthesis route. For BTZ formation reaction, the rate may be limited by the diffusion of Ba and/or O movement, which were proposed to be moveable during inter-diffusion experimental study in doped BT–BZ perovskite [83].

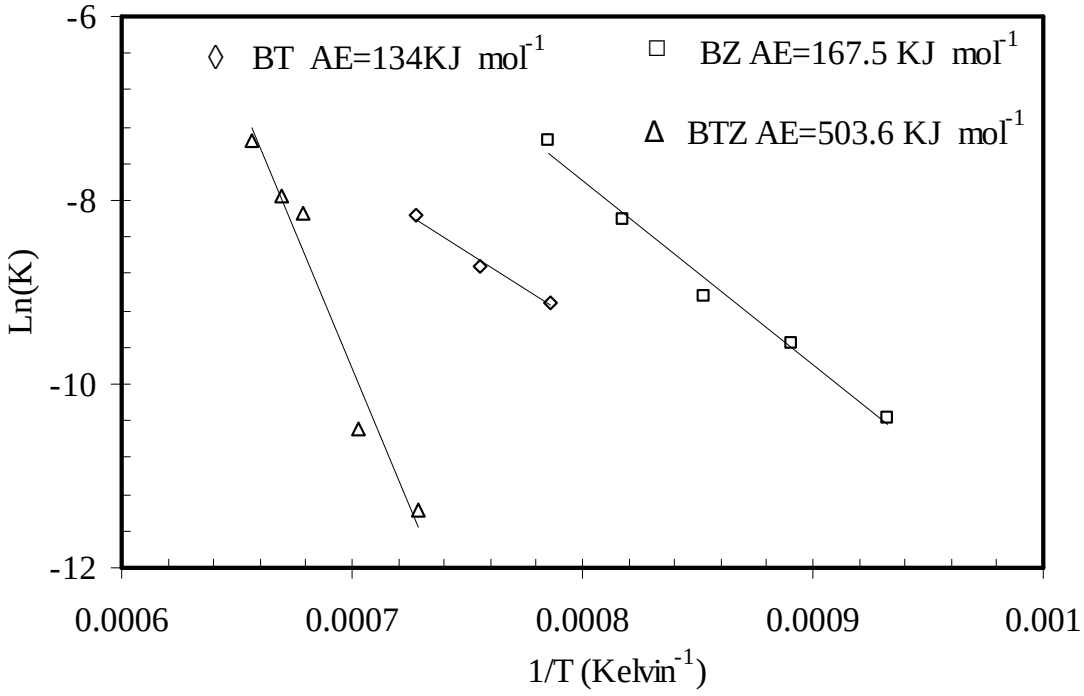

Fig.3.5. Arrhenius dependence of reaction rate on calcinations temperature for the transformation of precursors to $BaTiO_3$ (◊) and $BaZrO_3$ (□) and then to $BaTi_{0.6}Zr_{0.4}O_3$ solid solution (Δ) and their calculated activation energy (AE).

The lattice parameter of BT (a_o= 4.0161±10) remains more or less constant in all temperature ranges up to 1150^{o}C. In case of BZ, it is almost constant (a_o= 4.182±08) up to 1000^{o}C and decreases (a_o= 4.1382) as the temperature increases to 1150^{o}C. It is supposed that titanium from BT inter-diffuses in to BZ after 1050^{o}C, which is responsible for this decrease in lattice parameter. From the XRD, it is found that [110] peak of BZ shifts to higher angle with increase in calcinations temperature from 1050^{o}C to 1150^{o}C. It indicates the decrease in unit cell volume due to the incorporation of smaller Ti^{4+} ions. The lattice parameter of BT remains constant indicating there is no diffusion of Zr^{4+} ion into BT lattices.

The lattice parameter of BTZ (a_o= 4.0832(37)) decreases to (a_o= 4.0811(19)) with the increase in reaction time from 2 hours to for 16 hours at 1200^{o}C. This confirms the diffusion of titanium from BT in to BZ. It indicates that the initial solid solution was

higher in Zr^{4+} ion content than the final equilibrium one. So it may be considered that solid solution grows on BZ lattices having a coherent interface with BZ crystal. As BT decomposes and Ti diffuses into BZ, the lattice parameter of BZ decreases and that of BT remain constant. Moreover the lattice parameter a_o=4.0811 of BTZ indicates a good stoichiometry of the compound compared with reported parameter for $BaTi_{0.65}Zr_{0.35}O_3$ (a_o=4.0683) by Sciau *et.al.* [24] and for $BaTi_{0.6}Zr_{0.4}O_3$ (a_o=4.08) by Pantou *et.al.* [91].

Densification behaviour: To understand the sintering behavior, linear shrinkage of powder compact was measured up to 1450^{o}C at different heating rates as described by J. Jean *et al* [92]. Fig. 3.6 shows shrinkage behavior of compact powder at different constant heating rates. The shrinkage seems to start from around 1150^{o}C onwards. The onset sintering temperature is around 1300^{o}C and materials can be sintered within 1400^{o}C, which is lower than solid state synthesized power [83]. As expected the shrinkage curve shifted to higher temperature with increase in heating rate. The activation energy for the densification has been calculated from the equation as [92]:

$$Ln\left[T\frac{d\left(\frac{\Delta L}{Lo}\right)}{dT}\right] = Ln\left[\frac{1}{n}Ko^{\frac{1}{n}}\right] - \frac{1}{n}Ln(a) - \frac{Q}{nRT} \qquad (3.9)$$

where $\frac{\Delta L}{Lo}$ is the fractional shrinkage over time, T is the temperature, n is the experimental exponent, K_o is the pre-exponential term, a is the heating rate, Q is the apparent activation energy of sintering and R is the gas constant. The value of n can be determined from Fig. 3.7 by re-plotting the data in Fig. 3.6 as $Ln\frac{d\left(\frac{\Delta L}{Lo}\right)}{dT}$ versus $Ln(a)$ at different temperatures.

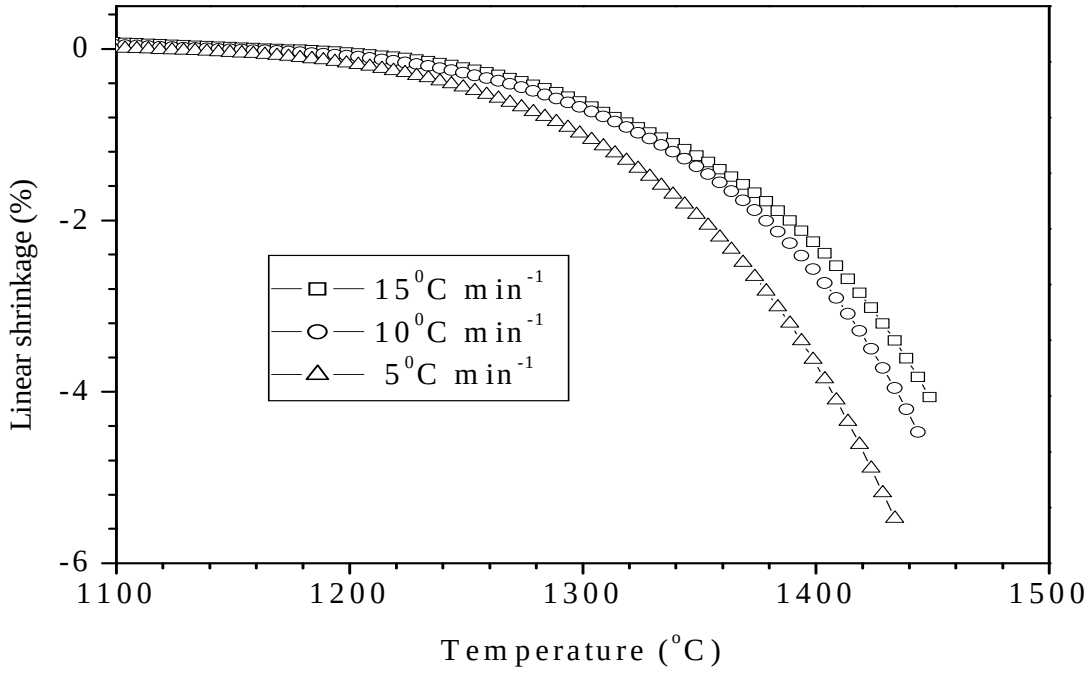

Fig.3.6. Shrinkage curves for $Ba(Ti_{0.6}Zr_{0.4})O_3$ ceramics at different constant heating rates.

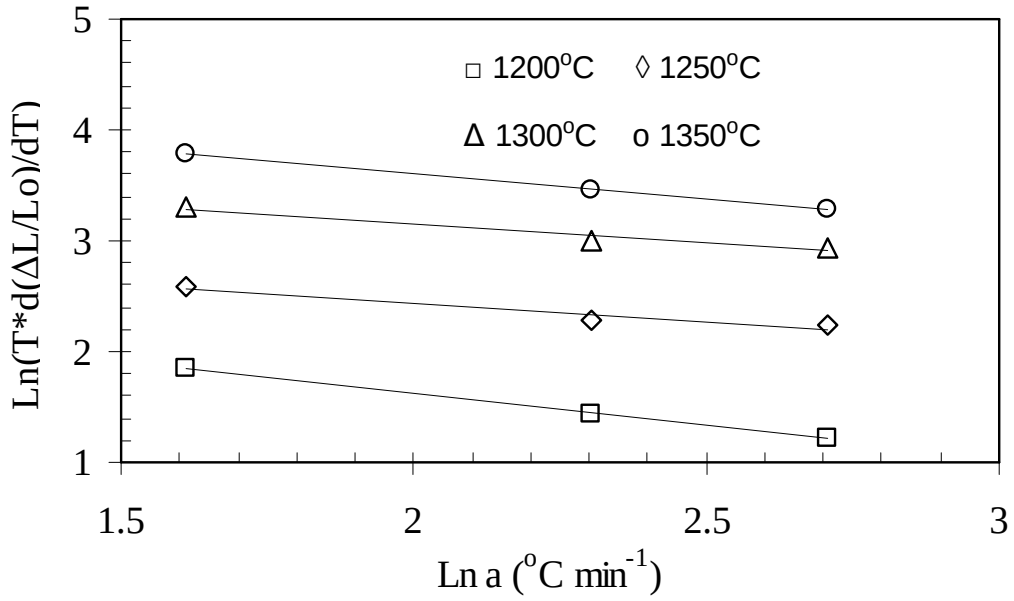

Fig.3.7. Data in figure. 3.6. replotted according to equation (3.9)

No significant change in slope ($-\frac{1}{n}$) is observed when the temperature is increased from 1150°C to 1350°C. These slopes have a range of $\frac{1}{1.8}$ to $\frac{1}{2.2}$ and a mean

value of $\frac{1}{2}$. With the knowledge of the value '*n*', the value of *Q* of the rate-limiting step during constant-rate heating is determined by re-plotting the data used in Fig. 3.6 as $Ln\frac{d\left(\frac{\Delta L}{Lo}\right)}{dT}$ versus $\frac{1}{T}$ at different heating rates (Fig. 3.8). The activation energy at different heating rates is determined from the slopes ($\frac{-Q}{2R}$) of these straight lines. The mean activation energy was calculated to be 550 KJ mol^{-1}. Here again, the rate may be limited by the diffusion of Ba and/or O movement, as the activation energy is similar to that found for the BTZ phase formation.

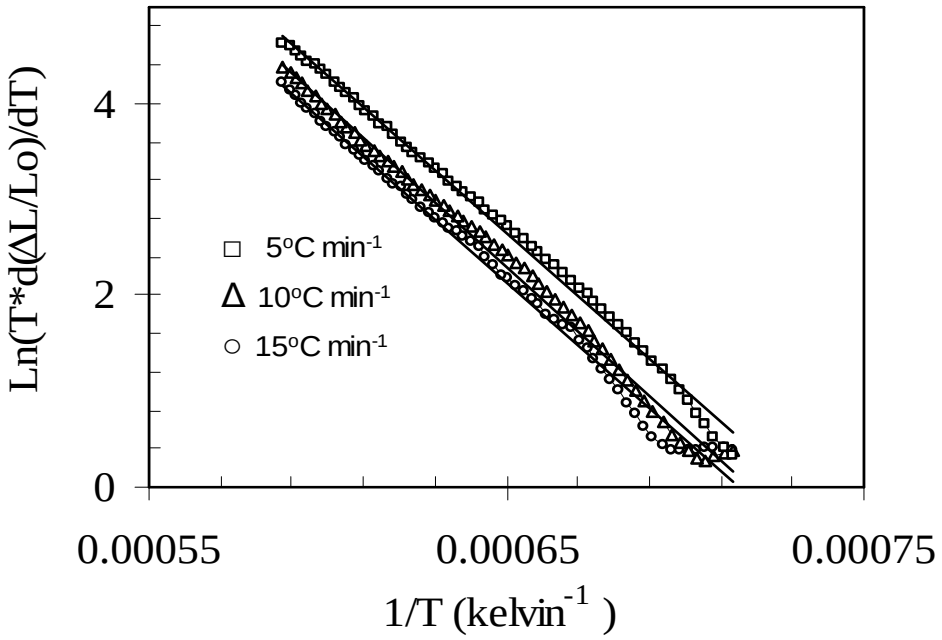

Fig.3.8. Determination of activation energy at different constant heating rates for the shrinkage data obtained non-isothermally as represented in Fig 3.6.

The section of shrinkage curve used in the activation energy calculation is from initial and intermediate stages of sintering, where neck growth and removal of porosity are the main reason for the shrinkage. Though, a small amount of grain growth takes place, which is well known to be the main process during final stage of sintering, it is expected to have negligible contribution towards shrinkage. That is why shrinkage, in this

case, is due to the removal of pores by diffusion of materials. Our investigation shows that the onset sintering temperature is around 1300^{o}C and materials can be sintered within 1400^{o}C, which is lower than solid state synthesized power sintering temperature. For example the sintering temperature of $BaTiO_3$ in solid state reaction route is around 1400^{o}C and that of BZ is 1500^{o}C [93]. So BTZ formation temperature lies between 1400^{o}C -1500^{o}C.

3.2.3 Conclusion

$BaTi_{0.6}Zr_{0.4}O_3$ perovskite has been synthesized from the mixture of barium oxalate hydrate, titanium dioxide and zirconium oxy-hydroxide. Studies on phase formation mechanism show that, the BT and BZ phases are formed separately in the system. Then, $BaTi_{0.6}Zr_{0.4}O_3$ was formed by the reaction between BT and BZ. Formation of intermediate phases likes Ba_2ZrO_4, Ba_2TiO_4 or $BaTi_3O_7$, etc., has not been detected. BT formation activation energy, 134 KJ mol^{-1}, was lower than BZ formation energy, 167.5 KJ mol^{-1}. That may be due to the difference in their ionic radius. BT–BZ solid solution was formed mainly by the diffusion of titanium from BT into the BZ lattice, where the latter phase acts as diminishing core. Activation energy for BTZ solid solution formation was 503.6 KJ mol^{-1}, which may be due to the diffusion of Ba and/or O ions through solid solution interface. The mean activation energy for sintering of compact powder was evaluated to be 550 KJ mol^{-1}.

3.3 La doped $Ba(Ti_{0.6}Zr_{0.4})O_3$

3.3.1 Introduction

Doping of ABO_3 and $A(B'B'')O_3$ based perovskite ferroelectrics is of great importance in the material technology of ferroelectric devices. Because of intrinsic capabilities, different dopants can be substituted in the lattice. The mechanism of dopant incorporation into the lattice has been extensively investigated and the behaviour of some transition metal ion as well as that of larger rare-earth ions has been elucidated by different researcher. However, the effect of the specific dopant on the electrical properties depends on the substitution site as well as on the nature of the lattice/electronic charge compensation defect.

In $Ba(Ti,Zr)O_3$, a trivalent ion behaves as an acceptor when substitution occurs at Ti/Zr site or as donor when it substitutes at the Ba sites. The ionic radius is the parameter which mainly determines the substitution site. Because of their small size, transition series ions like; Cr^{4+} (0.55Å), Fe^{3+} (0.64Å), Co^{3+} (0.63Å), Mn^{3+} (0.64Å), Mn^{4+} (0.53Å), Nb^{5+} (0.64Å), and Ta^{5+} (0.64Å) etc, prefers substitution on the Ti site. For Y^{3+} and lanthanide ions of intermediate size (from Sm^{3+} (1.04Å) to Er^{3+} (0.96Å)), there are some indication that, the substitution site is not exclusive, but is affected by dopant concentration, sintering temperature, sintering atmosphere and Ba/Ti molar ratio. However, La^{3+} (1.15Å) and Nd^{3+} (1.08Å) are exclusively incorporated at the Ba^{2+} (1.35Å) site, as their size is incompatible with that of Ti^{4+} (0.68Å) [94-97]. Buscaglia *et.al*. [94] had prepared samples according to five formulations corresponding to different potential incorporation mechanism for Erbium in $BaTiO_3$ with different values of the Ba/Ti molar ratio. The mechanisms are stated below:

Case 1: Barium substitution electron compensation with formula $A_{1-x}Er_xe_xBO_3$, where free electrons are added into the lattice, for which there is no need of vacancy compensation. This is also called electron donor doping.

Case 2: Barium substitution titanium vacancy compensation with general formula $A_{1-x}Er_xB_{1-x/4}O_3$, where erbium substitution at Ba site needs vacancy compensation in Ti site.

Case 3: Barium substitution barium vacancy compensation with general formula $A_{1-3x/2}Er_xBO_3$, where erbium substitution at Ba site needs vacancy compensation in Ba site.

Case 4: Self compensation with general formula $A_{1-x/2}Er_xB_{1-x/2}O_3$, where erbium substitutes both Ba and Ti site and the charge is being compensated within itself.

Case 5: Titanium substitution oxygen vacancy compensation with general formula $AEr_xB_{1-x}O_{3-x/2}$, where erbium substitution at Ti site needs vacancy creation in oxygen site.

The compensation mechanism as stated in case 2 above has been adopted in the present investigations because that generate most insulating dielectrics due to the B site vacancy compensation mechanism [98]. B site in the present dielectrics BTZ contains Ti and Zr. So the charge compensation can be done by creating vacancy (i) at Ti only, (ii) at Zr only and (iii) at both the Ti and Zr. The material has been synthesized by modified solid state route considering above three B site compensation mechanisms. The phase formation characteristics were investigated. The shrinkage behavior of the powder was studied.

3.3.2 Experimental procedure

Lanthanum doped $BaTi_{0.6}Zr_{0.4}O_3$ composition $Ba_{1-x}La_xTi_{0.6[1-(5x/12)]}Zr_{0.4}O_3$, $Ba_{1-x}La_x(Ti_{0.6}Zr_{0.4(1-5x/8)})O_3$ and $Ba_{1-x}La_x(Ti_{0.6(1-x/4)}Zr_{0.4(1-x/4)})O_3$ with x = 0.005, 0.01, 0.02, 0.05 and 0.1 were prepared. The compensation mechanism formulae are derived as follows:

The general formula with this compensation mechanism is $Ba_{1-x}La_x(Ti_{0.6}Zr_{0.4})_{1-x/4}O_3$ with ([Ba+La]/[Ti+Zr])>1. There are three possible cases of vacancy compensation, according to vacancy creation at Ti and/or Zr.

1. Vacancy creation only at Ti.

$$Ba_{1-x}La_x(Ti_{0.6}Zr_{0.4})_{1-x/4}O_3 = Ba_{1-x}La_x(Ti_{0.6(1-x/4)}Zr_{0.4(1-x/4)})O_3$$
$$= Ba_{1-x}La_x(Ti_{0.6(1-x/4)}Zr_{(0.4-0.4x/4)})O_3$$
$$= Ba_{1-x}La_x(Ti_{(0.6(1-x/4)-(0.6*(0.4/\ 0.6)x/4))}Zr_{0.4})O_3$$
$$= Ba_{1-x}La_x(Ti_{0.6(1-x/4-x/6)}Zr_{0.4})O_3$$
$$= Ba_{1-x}La_x(Ti_{0.6(1-5x/12)}Zr_{0.4})O_3 \quad (3.10)$$

2. Vacancy creation only at Zr site.

$$Ba_{1-x}La_x(Ti_{0.6}Zr_{0.4})_{1-x/4}O_3 = Ba_{1-x}La_x(Ti_{0.6(1-x/4)}Zr_{0.4(1-x/4)})O_3$$
$$= Ba_{1-x}La_x(Ti_{0.6-0.6*x/4}Zr_{0.4(1-x/4)})O_3$$
$$= Ba_{1-x}La_x(Ti_{0.6}Zr_{(0.4(1-x/4)-\ (0.4*(0.6/\ 0.4)x/4}O_3$$
$$= Ba_{1-x}La_x(Ti_{0.6}Zr_{0.4(1-x/4\ -\ 6x/16)})O_3$$
$$= Ba_{1-x}La_x(Ti_{0.6}Zr_{0.4(1-5x/8)})O_3 \quad (3.11)$$

3. Vacancy creation both at Zr and Ti site.

$$Ba_{1-x}La_x(Ti_{0.6}Zr_{0.4})_{1-x/4}O_3 = Ba_{1-x}La_x(Ti_{0.6(1-x/4)}Zr_{0.4(1-x/4)})O_3 \quad (3.12)$$

Analytical grade barium nitrate ($Ba(NO_3)_2$), lanthanum dioxide (La_2O_3), titanium dioxide (TiO_2), zirconium oxy-chloride ($ZrOCl_2.8H_2O$), ammonia (NH_4OH) and oxalic acid ($(COOH)_2.2H_2O$) were used as raw materials in this process. All the chemicals were from Merck, India (GR grade with 99% purity).

To prepare 20gm batch of the composition $Ba_{1-x}La_xTi_{0.6[1-(5x/12)]}Zr_{0.4}O_3$ with x=0.05, 0.0759 mol of barium nitrate, 0.0469 mol of titanium dioxide, 0.0039 mol of lanthanum dioxide, 0.0319 mol of zirconium oxy-chloride and 0.08 mol of oxalic acid were taken.

In $Ba_{1-x}La_x(Ti_{0.6}Zr_{0.4(1-5x/8)})O_3$ with x=0.05, 0.0761 mol of barium nitrate, 0.0481 mol of titanium dioxide, 0.004 mol of lanthanum dioxide, 0.031 mol of zirconium oxy-chloride and 0.0801 mol of oxalic acid were taken.

Similarly, in $Ba_{1-x}La_x(Ti_{0.6(1-x/4)}Zr_{0.4(1-x/4)})O_3$ with x=0.05, 0.0760 mol of barium nitrate, 0.0474 mol of titanium dioxide, 0.004 mol of lanthanum dioxide, 0.0316 mol of zirconium oxy-chloride and 0.08 mol of oxalic acid were taken.

The synthesis and characterization was the same as discussed in the section 3.2.1. Prior to the addition of $ZrOCl_2.8H_2O$ into the barium nitrate solution, required amount of lanthanum dioxide was added along with small amount of HNO_3. Nitric acid helps in dissolving lanthanum dioxide into the solution.

3.3.3 Results and discussion

Phase formation behaviour: Fig.3.9. shows the XRD patterns of the precursor for the composition $Ba_{0.98}La_{0.02}(Ti_{0.595}Zr_{0.4})O_3$ heated at different temperatures. The analysis of raw powder shows the presence of $BaC_2O_4.0.5H_2O$ and TiO_2 (Fig. 3.9(a)). $BaC_2O_4.0.5H_2O$ was converted to BaC_2O_4 upon calcinations at 400^oC (Fig. 3.9(b)). The 700^oC calcined precursor shows the presence of $BaCO_3$ and TiO_2. The precursor changed to pure phase upon calcination at 1200^oC for 4hours.

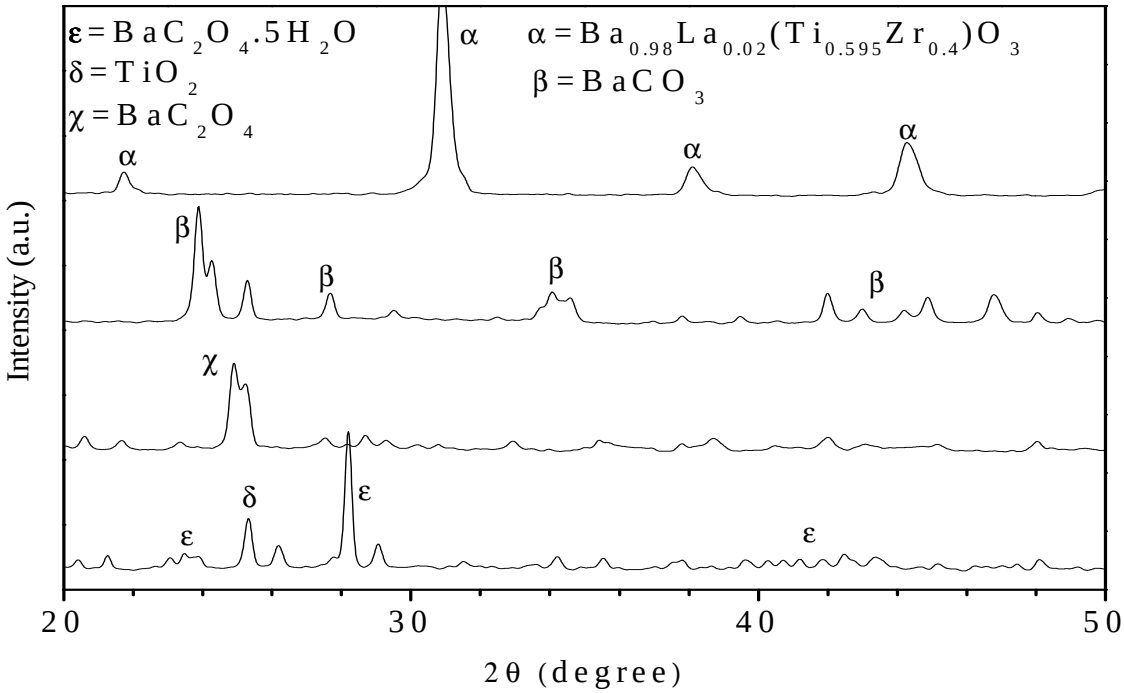

Fig.3.9. XRD patterns for (a) raw precursor and precursors calcined at (b) 400^{o}C, (c) 700^{o}C, (d) 1200^{o}C of the composition $Ba_{0.98}La_{0.02}(Ti_{0.595}Zr_{0.4})O_{3}$.

Fig.3.10 shows the phase formation of the composition $Ba_{0.98}La_{0.02}(Ti_{0.595}Zr_{0.4})O_3$ at different temperatures. (Fig. 3.10(a)) show the existence of both BT and BZ, which indicates that BT and BZ form separately in the system. This is almost similar to the phase formation of BTZ discussed in section 3.2.2.

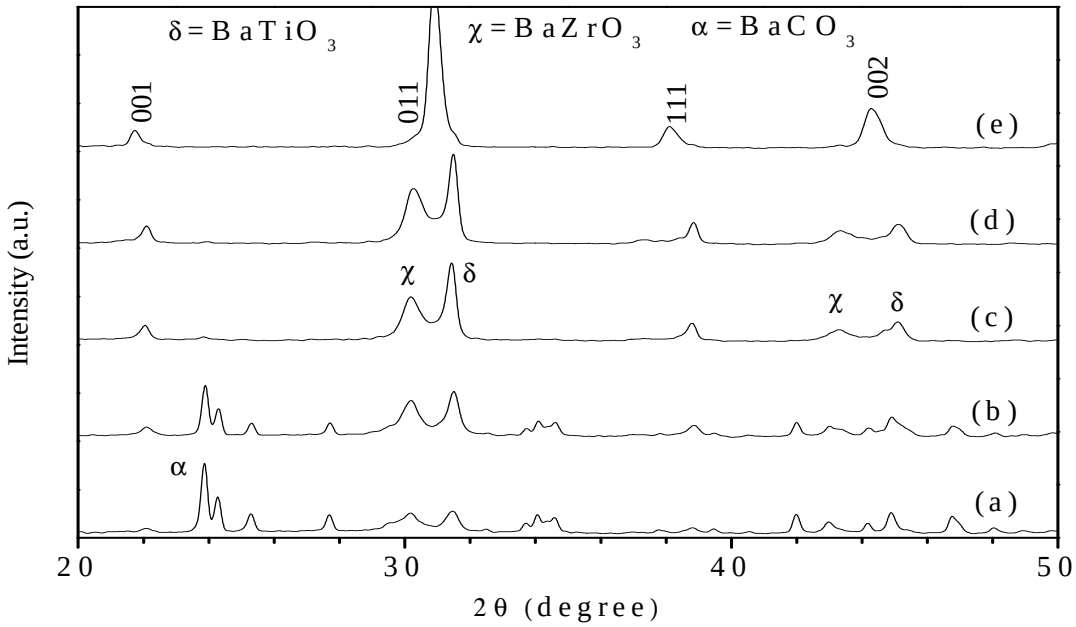

Fig.3.10. XRD patterns of $Ba_{0.98}La_{0.02}(Ti_{0.595}Zr_{0.4})O_3$ precursor powder calcined for 2h at (a) 750^{o}C, (b) 850^{o}C, (c) 1000^{o}C, (d) 1100^{o}C, and (e) calcined for 4h at 1200^{o}C.

To get phase pure product, the dry powder was calcined at 1200^{o}C for 2-16 hours depending upon composition in the furnace. A rather long calcination time was adopted for higher lanthanum substitutions to ensure a homogeneous dopant distribution in the final composition.

Fig.3.11 and Fig.3.12 shows the XRD patterns for the composition $Ba_{(1-x)}La_xTi_{0.6[1-(5x/12)]}Zr_{0.4}O_3$ and $Ba_{1-x}La_x(Ti_{0.6}Zr_{0.4[1-(5x/8)]})O_3$, respectively with x values 0, 0.005, 0.01, 0.02, 0.05 and 0.1. The lanthanum doped BTZ composition was found to be cubic. Reduced lattice parameter is obtained for higher substitution of lanthanum. A gradual shift of peak 2Θ angles to the higher angle with increasing lanthanum percentage reveals the contraction of perovskite lattice due to the smaller size of La^{3+} compared to Ba^{2+}.

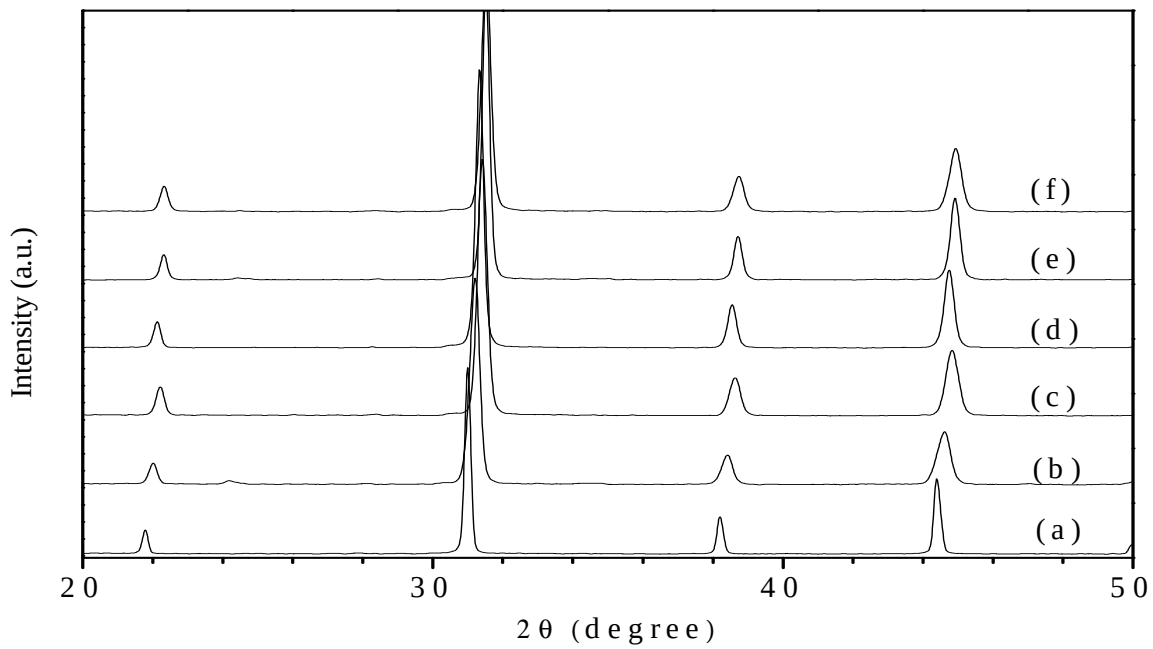

Fig.3.11. XRD patterns for $Ba_{(1-x)}La_xTi_{0.6[1-(5x/12)]}Zr_{0.4}O_3$ with x values (a) 0, (b) 0.005, (c) 0.01, (d) 0.02, (e) 0.05 and (f) 0.1.

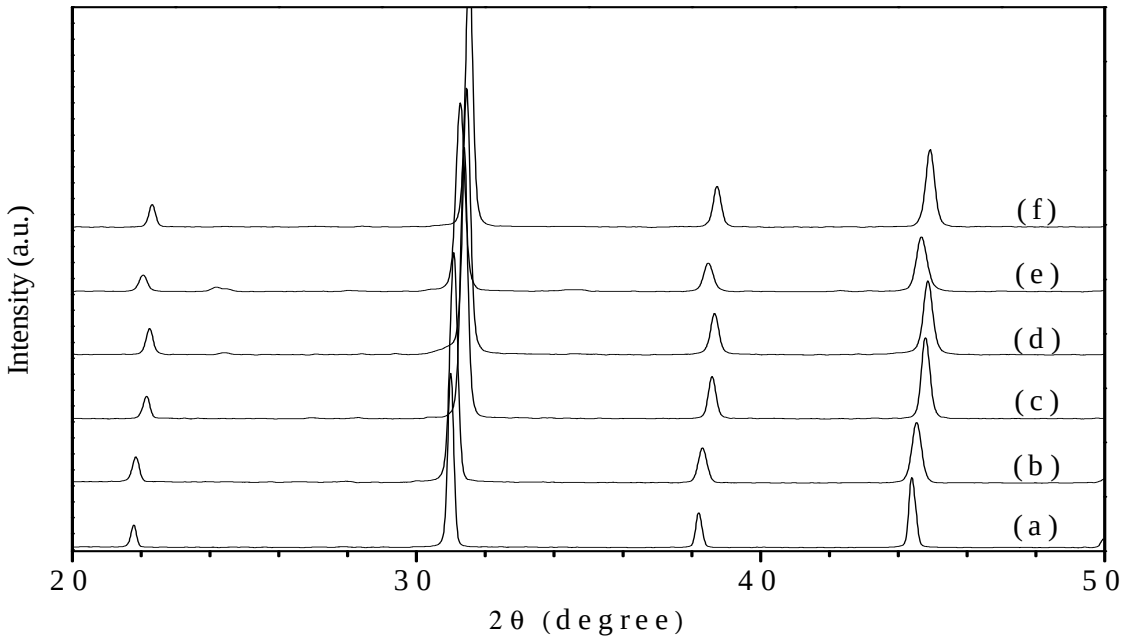

Fig.3.12. XRD patterns for $Ba_{1-x}La_x(Ti_{0.6}Zr_{0.4[1-(5x/8)]})O_3$ with x values (a) 0, (b) 0.005, (c) 0.01, (d) 0.02, (e) 0.05 and (f) 0.1.

Fig.3.13 shows the shrinkage curves for the composition $Ba_{1-x}La_x(Ti_{0.6}Zr_{0.4})_{1-x/4}O_3$ with x values 0, 0.02 and 0.1, at constant heating rate of 10^oC/min. It shows the sinterability of $BaTi_{0.6}Zr_{0.4}O_3$ is good compared to $Ba_{0.9}La_{0.1}(Ti_{0.585}Zr_{0.39})O_3$. Which implies lanthanum substitution decreases sinterability of BTZ ceramics.

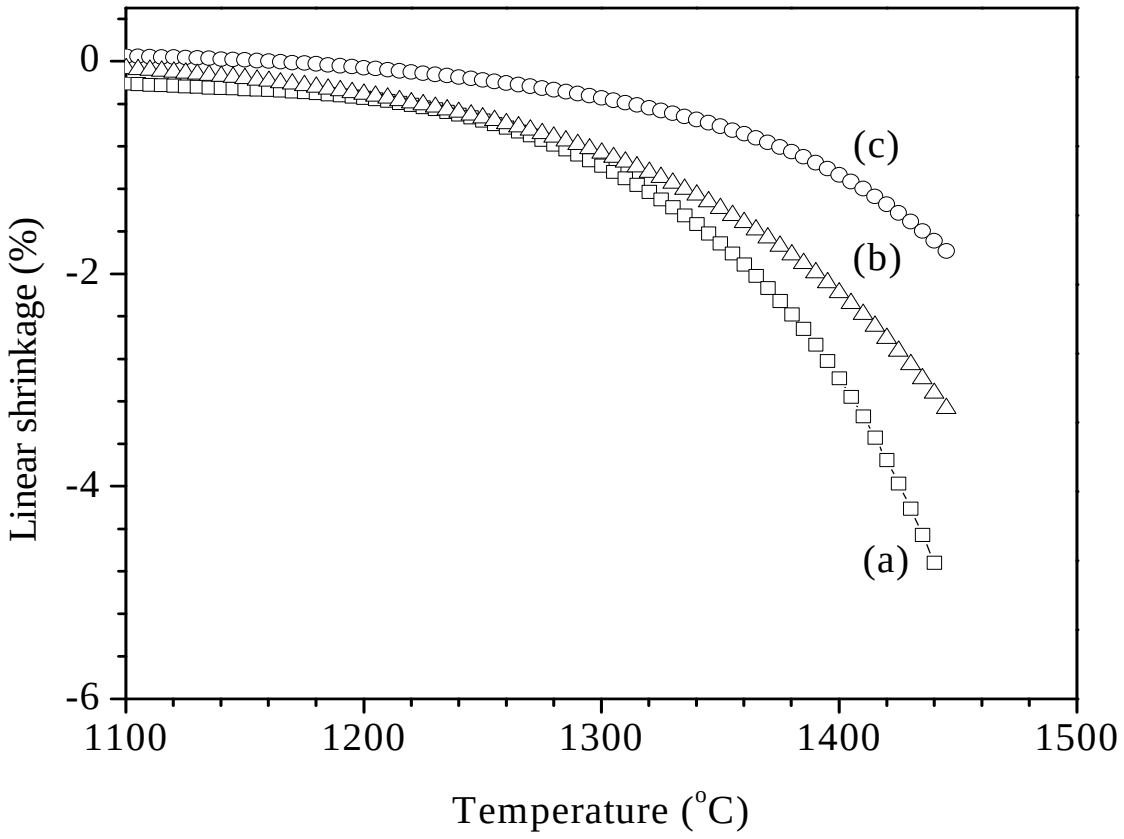

Fig.3.13. Shrinkage curves for the composition $Ba_{1-x}La_x(Ti_{0.6}Zr_{0.4})_{1-x/4}O_3$ with x values (a) 0, (b) 0.02 and (c) 0.1 at heating rate of 10^oC/min.

Similar shrinkage curves for $Ba_{0.9}La_{0.1}(Ti_{0.585}Zr_{0.39})O_3$ ceramics at different constant heating rates of 5^oC/min, 10^oC/min and 15^oC/min were found.

3.3.4 Conclusion

Lanthanum doped BTZ; $Ba_{1-x}La_xTi_{0.6}Zr_{0.4}O_3$ ceramics are synthesized with three compensation mechanisms viz. (a) Vacancy creation only at Ti (b) Vacancy creation only at Zr and (c) Vacancy creation both at Ti and Zr. BTZ is formed via the formation of $BaTiO_3$ and $BaZrO_3$ separately followed by inter-diffusion of two. The ionic size of La^{3+} is compatible with Ba^{2+}. Therefore lanthanum exclusively substituted at the Ba site. Lanthanum doped BTZ composition was found to be cubic. Reduced lattice parameter is obtained for higher substitution of lanthanum. A gradual shift of peak 2Ɵ angles to the higher angle with increasing lanthanum percentage reveals the contraction of perovskite lattice due to the smaller size of La^{3+} compared to Ba^{2+}. Sinterability of BTZ decreases with increasing lanthanum substitution.

CHAPTER 4

ELECTRICAL CHARACTERIZATION

4.1 Introduction

La- substituted $Ba(Zr_{0.4}Ti_{0.6})O_3$ based relaxor ceramics were prepared through modified solid state route. The influence of lanthanum on the dielectric properties, tan δ and dc resistivity of $Ba(Zr_{0.4}Ti_{0.6})O_3$ ceramics were examined. The effect of porosity on relative permittivity and tan δ was studied. The relaxor behavior of lanthanum doped samples was also analysed. The focus was on two conjugate effects which could be at the origin of the relaxor phenomena (1) the probable disorder exhibited, in appropriate scale regions, between the two tetravalent cations (2) the peculiar character of the rare-earth element which is known to induce an electronic "donor-doping" and/or an ionic compensation.

4.2 Dielectric properties

In this work, the influence of lanthanum on relative permittivity and tan δ were examined. The frequency dependence of dielectric permittivity and tan δ of the ceramics were studied.

4.2.1 Experimental procedure

Lanthanum doped compositions with x = 0.005, 0.01, 0.02, 0.05 and 0.1 in $Ba_{(1-x)}La_xTi_{0.6[1-(5x/12)]}Zr_{0.4}O_3$, $Ba_{(1-x)}La_x(Ti_{0.6}Zr_{0.4[1-(5x/8)]})O_3$ and $Ba_{(1-x)}La_x(Ti_{0.6[1-x/4]}Zr_{0.4[1-x/4]})O_3$ powders were prepared. The synthesis procedure has been described elaborately in the chapter 3. Calcined powders were used to fabricate pellets specimen for densification and then electrical characterization of all the dielectrics. A flow chart of fabrication, sintering and characterization is shown in Fig.4.1.

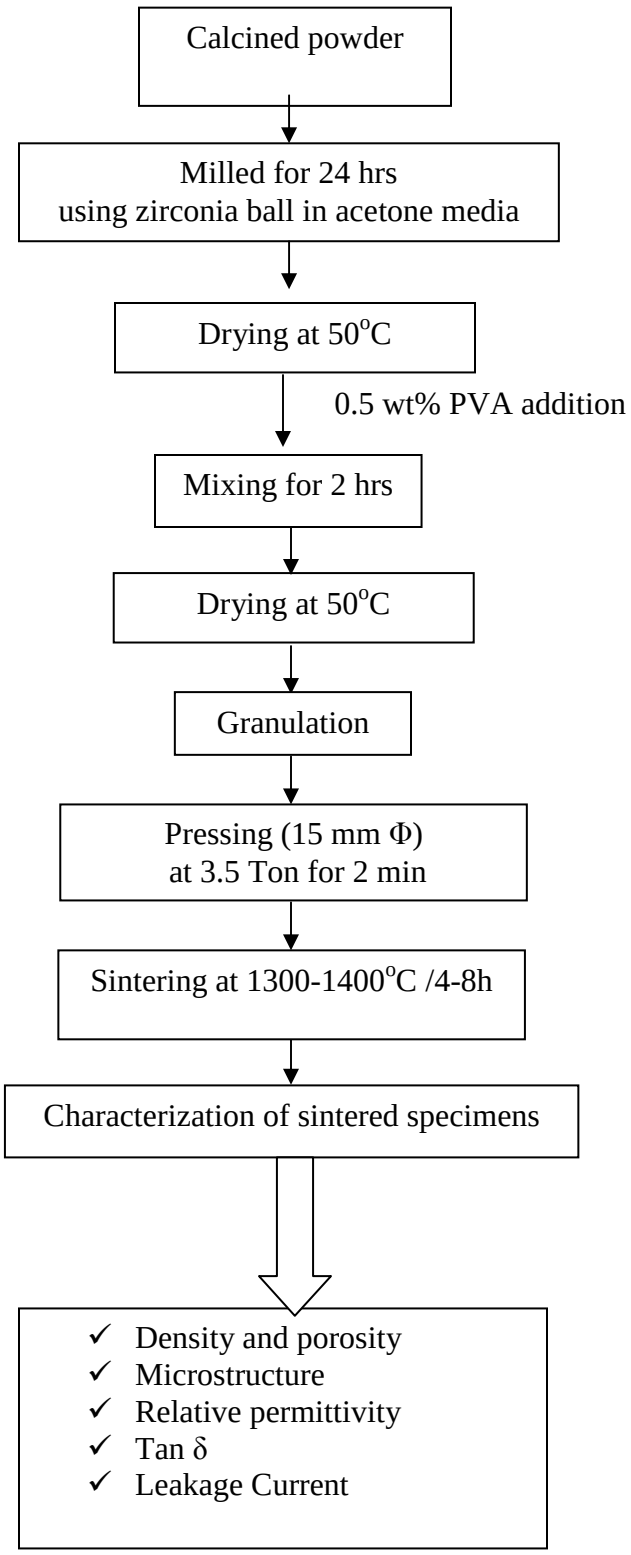

Fig.4.1. Flow chart for specimen fabrication, sintering and characterization

Fabrication: The calcined powder was ball milled for 24 hours inside polyethylene jar using zirconia balls and water as medium. The milled powder was dried at 50^{o}C. The dried powder was then mixed with 0.5 wt.% PVA. The powder was then granulated by sieving and the granules were uniaxially pressed to disk-shaped pellet (15 mm Φ) at 3.5 ton pressure by uniaxial hydraulic pressing.

Sintering: The pressed samples were sintered in an electrical furnace with super kanthal ($MoSi_2$) heating elements and alumina insulation boards as chamber walls (size of the chamber: 250x150x150mm). The thermal regime of the furnace was controlled through a "Eurotherm" programmer-cum-controller within ± 2°C accuracy. Fig. 4.2 shows the typical sintering profile. The compacted samples were heated from room temperature to 500^{o}C at a rate 2^{o}C/min followed by a soaking at 500^{o}C, 2h for binder burnout. Thereafter, the samples were heated at a rate 2°C/min to final sintering temperature 1300-1400°C with a soaking time of 4-8 hours depending on compositions. Then the specimen was cooled at a rate 1^{o}C/min to room temperature. A long sintering time was adopted to ensure a homogeneous dopant distribution in the final material. The usually adopted sintering times do not always guarantees the attainment of uniform distribution of temperature. Less sintering times indicates non-equilibrium and distorted states within the ceramic samples.

Density and apparent porosity measurement: Bulk density and apparent porosity of sinter specimens were determined by "Archimedes" principle. Samples were immersed in water and kept under a vacuum of 4mm of mercury for 5 hrs to ensure that water filled up the open pores completely. Then, soaked and suspended weights were measured at atmospheric pressure. The apparent porosity and bulk density were calculated as follows:

Dry weight of the sample = W_d, Soaked weight of the sample = W_s, Suspended weight of the sample = W_a

$$\% \text{ Apparent porosity} = \frac{W_s - W_d}{W_s - W_a} \text{x}100 \tag{4.1}$$

$$\text{Bulk density} = \frac{W_d}{W_s - W_a} \tag{4.2}$$

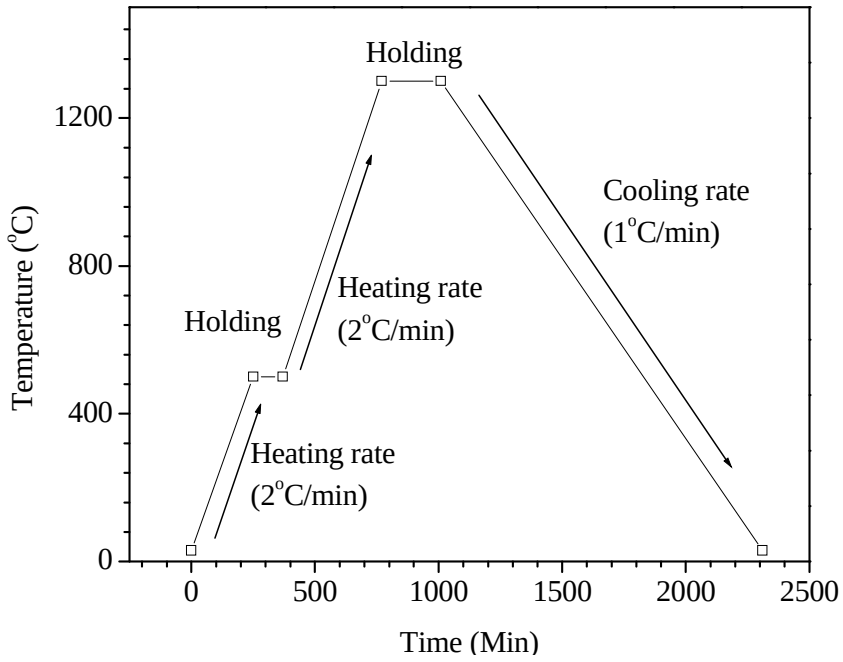

Fig.4.2. Typical sintering profile of BTZ specimens at 1300°C for 4hrs.

Microstructural analysis: Microstructures of the sintered specimens were analyzed by a Scanning Electron Microscope (SEM). In SEM, a hot tungsten filament electron gun under vacuum emits electrons which pass through a series of electromagnetic lenses. The sample is then bombarded with a fine beam of electrons having acceleration potentials range from 1-30 KV. A part of the beam is reflected as back scattered electrons (BSE) along with low energy secondary electron emission (SE), cathode luminescence, and x-ray excitation beam and electron transmission also take place.

Images formed from the (SE) beam were studied in the extrinsic mode of SEM. While the images appeared very real as if they are photographed by ordinary means, the apparent illumination was a function of particle emission rather than radiation. The emitted secondary electrons are detected and displayed on a scanning TV display. A bright image will be the result of high secondary electron emission, while the primary influence on high emission is the surface structure of the specimen. The end result is therefore brightness associated with surface characteristics and an image which looks very much like a normally illuminated subject.

Sample surfaces were ground with the help of a series of diamond grinding pad from 1200μm to 15μm on an automatic polishing machine. The samples were polished with 8μm diamond paste on a rotating disk. Final polishing was done with 6, 2 and 1μm diamond pastes to create a mirror finish on a lapping machine. Prior to microscopic analysis, the samples were thermally etched at 50^{o}C less than the respective sintering temperature.

The thermally etched samples were mounted on a metal stub with carbon paint. The samples were thin coated with palladium under vacuum of 0.01 torr to make the surface conducting for SEM. The mounted specimens were studied by SEM (JEOL-JSM840).

Capacitance and tan δ measurement: Capacitance and tan δ are the basic property of any capacitor. Electrodes were painted (Fig. 4.3) on the surface of the sintered sample using a conducting silver paste followed by firing at 700^{o}C for 10min, to form electrodes on both sides of the ceramic specimen for measurement purpose.

The Impedance Analyzer; Model 4192A, Hewlett Packard, USA, with the maximum frequency limit of the instrument 13MHz, was used to measure the capacitance and tanδ of the samples. The sample was placed in a special sample holder meant for such type of measurements. The relative permittivity (ε_r) was calculated using the following formula:

$$\varepsilon_r = \frac{cd}{\varepsilon_0 A} \qquad (4.3)$$

where ε_o is the permittivity of free space, c the capacitance, d the thickness and A the capacitor area.

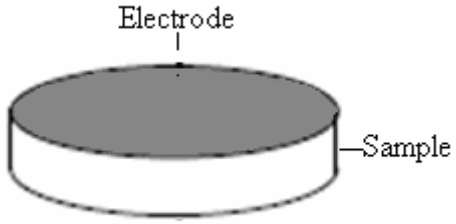

Fig. 4.3. Schematic electrode arrangement on the sintered pellet sample.

Variation of capacitance and tan δ with frequency was measured at room temperature.

4.2.2 Result and discussion

The bulk densities of the ceramics were as high as 90% of the theoretical density. Fig.4.4 and Fig.4.5 show the microstructure of $Ba_{(1-x)}La_xTi_{0.6[1-(5x/12)]}Zr_{0.4}O_3$ and $Ba_{(1-x)}La_x(Ti_{0.6}Zr_{0.4[1-(5x/8)]})O_3$ specimen. The grain size of samples decreases and then again increases with the increase of La concentration from 0 at.% to 10 at.%. These results reveal that small amount of La (≤2 at. %) doped in barium zirconate titanate ceramics, acts as grain growth inhibitor reducing grain size. However, grain growth is observed for higher La substitution. This is in accordance with the reported result of Chou *et.al* [31], who have prepared samples of the composition $Ba_{(1-x)}La_xZr_{0.2}Ti_{0.8-x/4}O_3$ in air, with x in the range of maximum 0.04.

Fig.4.6 shows the energy dispersive x-rays (EDX) spectra of undoped and 0.5 at.% lanthanum doped sample. Lanthanum doped samples show the evidence of lanthanum, barium, titanium, zirconium and oxygen where as undoped sample show the existence of barium, titanium, zirconium and oxygen.

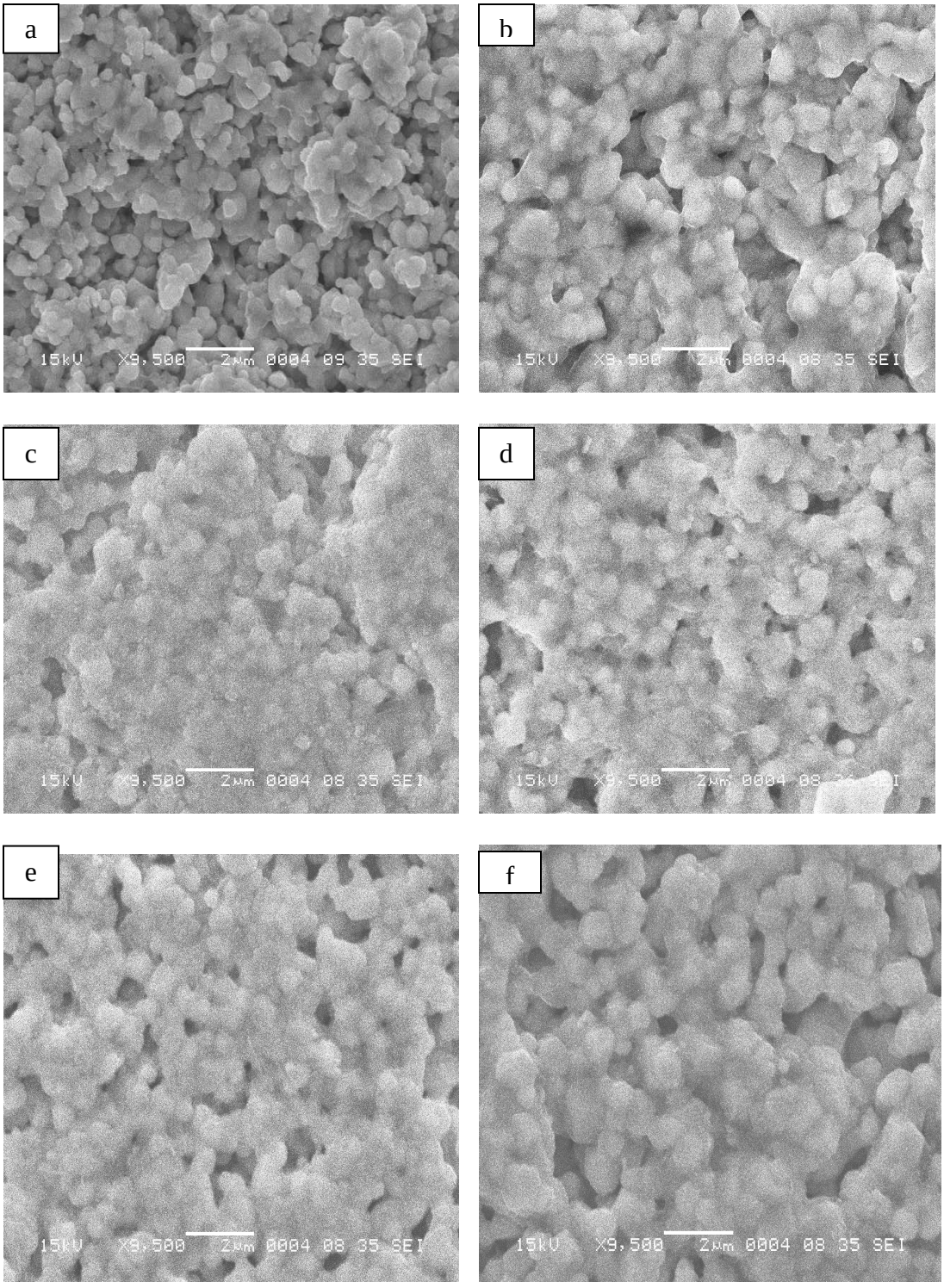

Fig.4.4. SEM micro structure of $Ba_{(1-x)}La_xTi_{0.6[1-(5x/12)]}Zr_{0.4}O_3$ with x values (a) 0, (b) 0.005, (c) 0.01, (d) 0.02, (e) 0.05 and (f) 0.1.

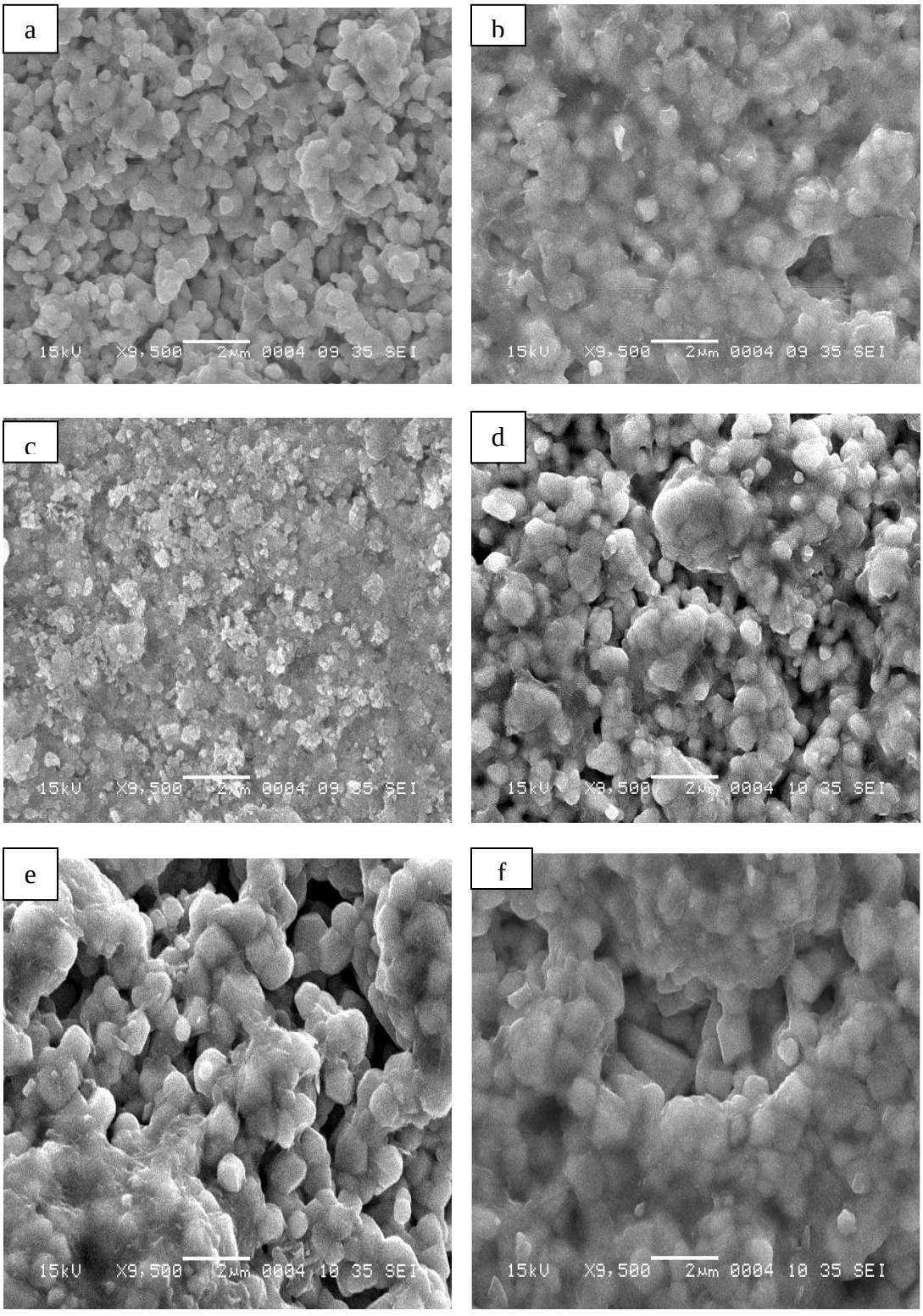

Fig.4.5. SEM micro structure of $Ba_{(1-x)}La_x(Ti_{0.6}Zr_{0.4[1-(5x/8)]})O_3$ with x values (a) 0, (b) 0.005, (c) 0.01, (d) 0.02, (e) 0.05 and (f) 0.1.

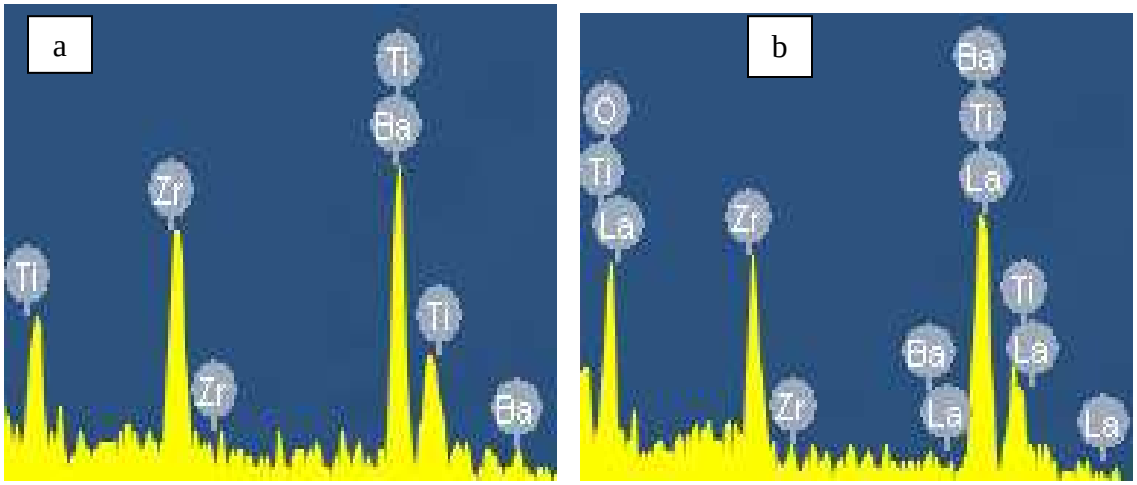

Fig.4.6. EDX spectra of $Ba_{(1-x)}La_xTi_{0.6[1-(5x/12)]}Zr_{0.4}O_3$ with x values (a) 0, (b) 0.005.

The relative permittivity (ε_r) at room temperature was measured for different samples. Fig.4.7 shows the frequency dependency of relative permittivity for the composition $Ba_{(1-x)}La_xTi_{0.6[1-(5x/12)]}Zr_{0.4}O_3$. The result shows a flat ε_r with frequency. It indicates high dielectric stability against change in frequency. It is in accordance with the result reported by Wu *et.al*. [27] and Aliouane *et.al*. [30]. Fig. 4.8 and Fig. 4.9 show the relative permittivity as a function of frequency for the composition $Ba_{(1-x)}La_x(Ti_{0.6[1-x/4]}Zr_{0.4[1-x/4]})O_3$ and $Ba_{(1-x)}La_x(Ti_{0.6}Zr_{0.4[1-(5x/8)])}O_3$. These figures also show the same pattern as that of Fig 4.7.

The permittivity value decreases with increasing lanthanum percentage. Permittivity of undoped sample was found to be around 900 where as for 10 atom % lanthanum doped, it was around 100. The ionic doping mechanism involves partial replacement of Ba^{+2} with the smaller La^{+3} ion on the A-site with creation of B-site vacancies. The B-site vacancy introduce void inside O_6 octahedra. It is known that in ABO_3 perovskite, ferroelectric phenomena are related to the shifting of B-site cation from its equivalent position. In the present case, both A-site replacement and B site vacancy reduce the permittivity. The unit cell parameters slightly decrease with La^{3+}, due to its smaller size.

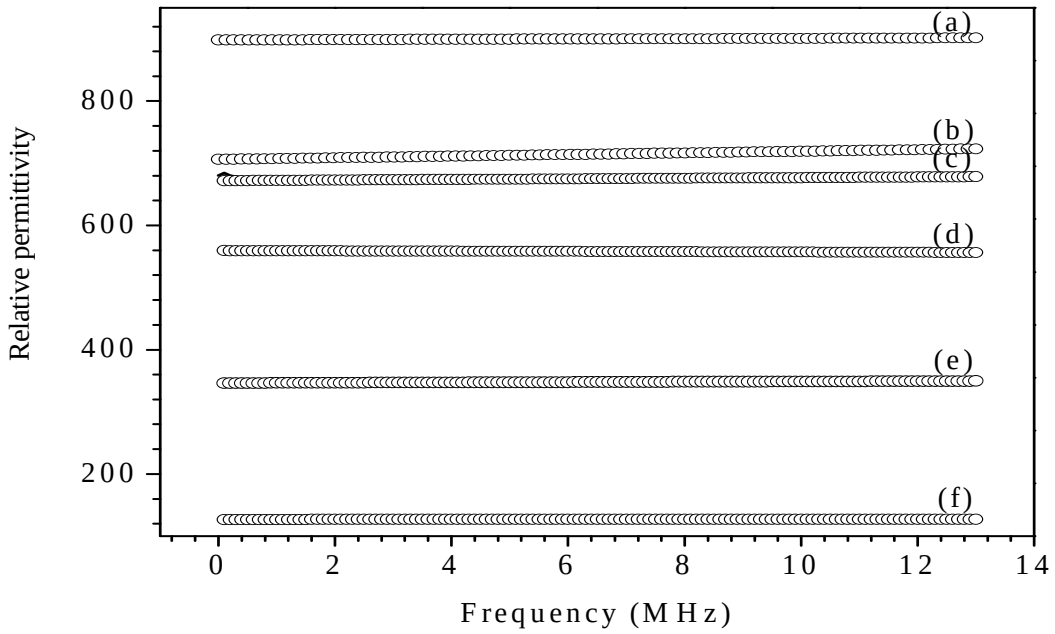

Fig.4.7. Relative permittivity of $Ba_{(1-x)}La_xTi_{0.6[1-(5x/12)]}Zr_{0.4}O_3$ as a function of frequency with x values (a) 0,(b) 0.005, (c) 0.01, (d) 0.02, (e) 0.05 and (f) 0.1.

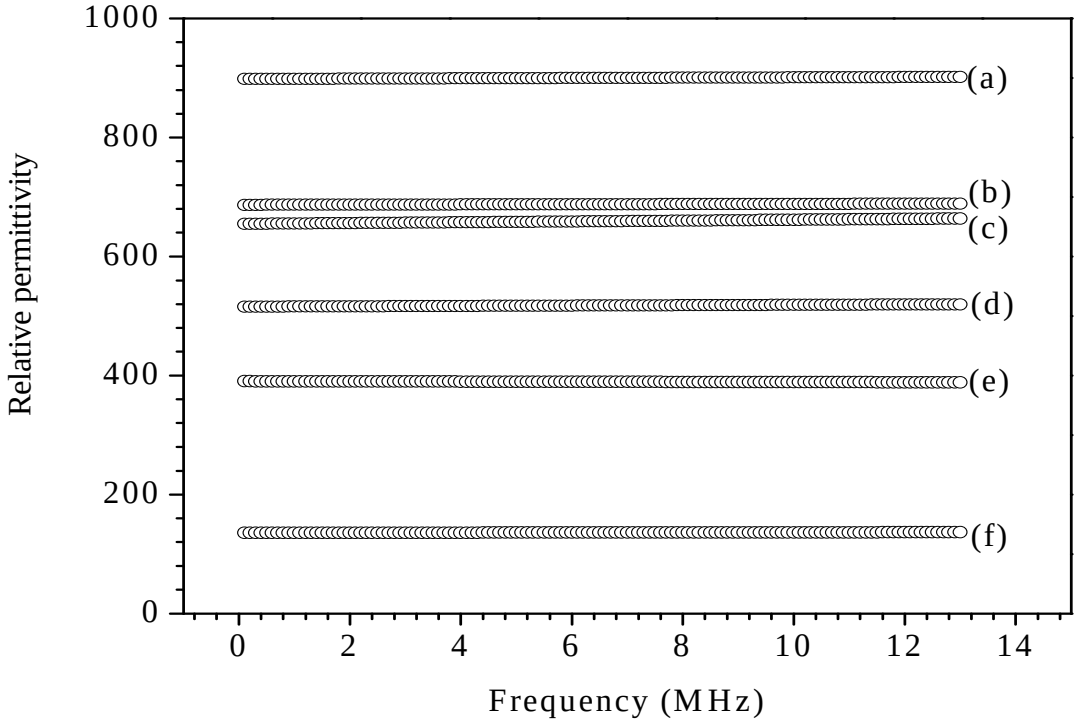

Fig.4.8. Relative permittivity of $Ba_{(1-x)}La_x(Ti_{0.6[1-x/4]}Zr_{0.4[1-x/4]})O_3$ as a function of frequency with x values (a) 0,(b) 0.005, (c) 0.01, (d) 0.02, (e) 0.05 and (f) 0.1.

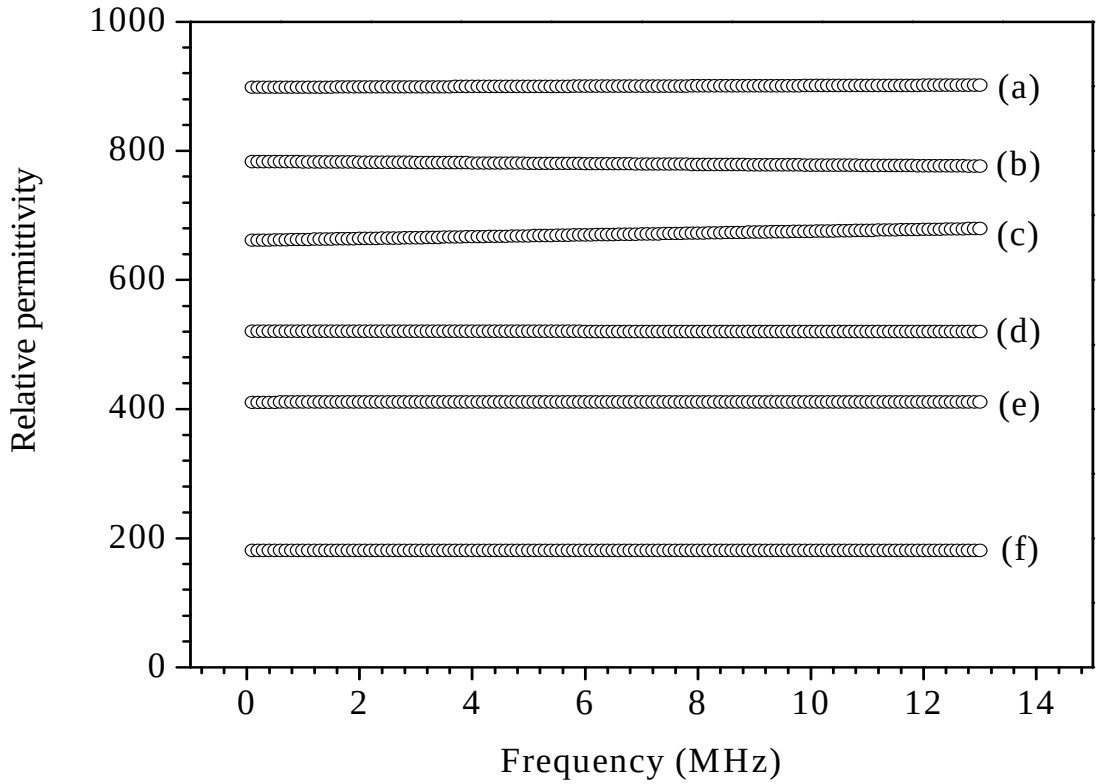

.

Fig.4.9. Relative permittivity of $Ba_{(1-x)}La_x(Ti_{0.6}Zr_{0.4[1-(5x/8)]})O_3$ as a function of frequency with x values (a) 0, (b) 0.005, (c) 0.01, (d) 0.02, (e) 0.05 and (f) 0.1.

Fig.4.10 shows the relative permittivity of the composition $Ba_{(1-x)}La_xTi_{0.6[1-(5x/12)]}Zr_{0.4}O_3$ with different lanthanum percentage at 5MHz. Similarly Fig.4.11 and Fig.4.12 show the same for other compositions. It may be observed that the relative permittivity decreases sharply for the small percentage of lanthanum compared to higher doped one. Decreased permittivity was due to the decrease in Ba content which is ferroelectrically more active than La.

The variation of tan δ as a function of frequency, for the composition $Ba_{(1-x)}La_xTi_{0.6[1-(5x/12)]}Zr_{0.4}O_3$ is shown in Fig.4.13. Similarly Fig.4.14 and Fig.4.15 show the same variation for the composition $Ba_{(1-x)}La_x(Ti_{0.6[1-x/4]}Zr_{0.4[1-x/4]})O_3$ and $Ba_{(1-x)}La_x(Ti_{0.6}Zr_{0.4[1-(5x/8)]})O_3$, respectively. Tan δ obeys a decreasing tendency with increasing lanthanum percentage. However, higher tan δ was noticed for 0.5 atom % doped samples in the composition $Ba_{(1-x)}La_x(Ti_{0.6[1-x/4]}Zr_{0.4[1-x/4]})O_3$ and $Ba_{(1-x)}La_x(Ti_{0.6}Zr_{0.4[1-(5x/8)]})O_3$.

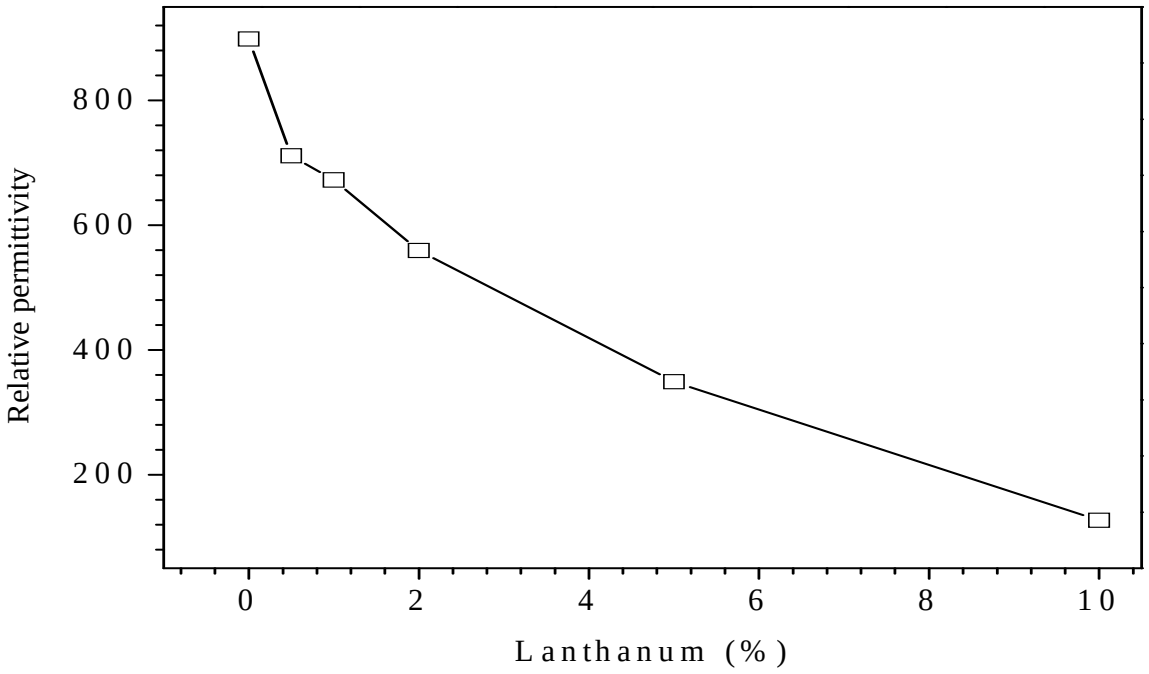

Fig.4.10. Relative permittivity at 5MHz of $Ba_{(1-x)}La_xTi_{0.6[1-(5x/12)]}Zr_{0.4}O_3$ with different lanthanum percentage.

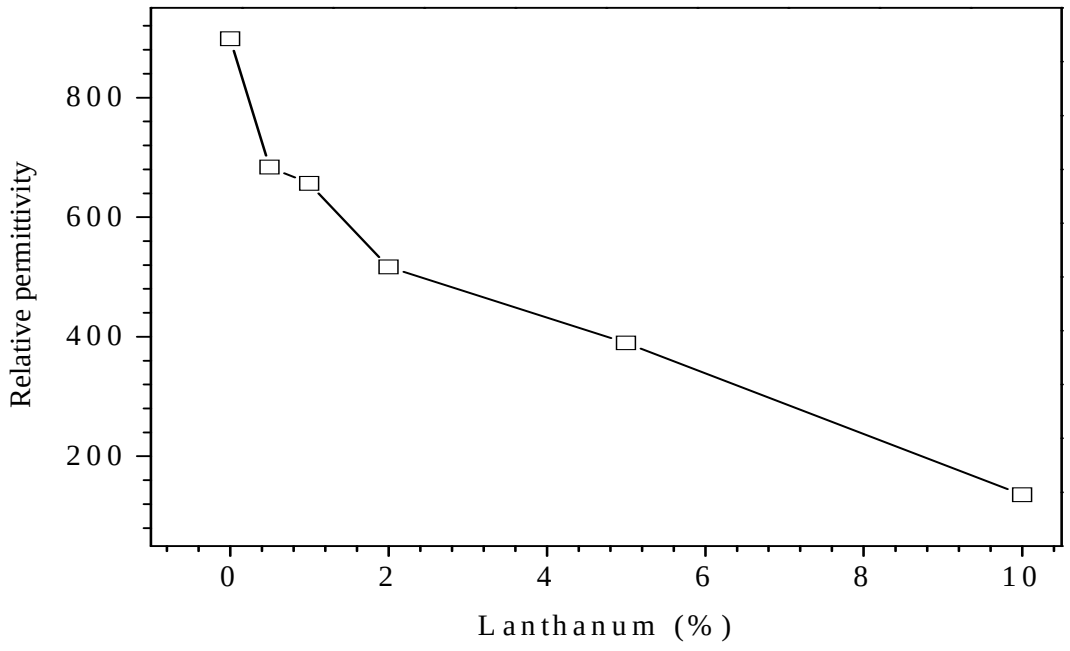

Fig.4.11. Relative permittivity at 5MHz of $Ba_{(1-x)}La_x(Ti_{0.6[1-x/4]}Zr_{0.4[1-x/4]})O_3$ with different lanthanum percentage.

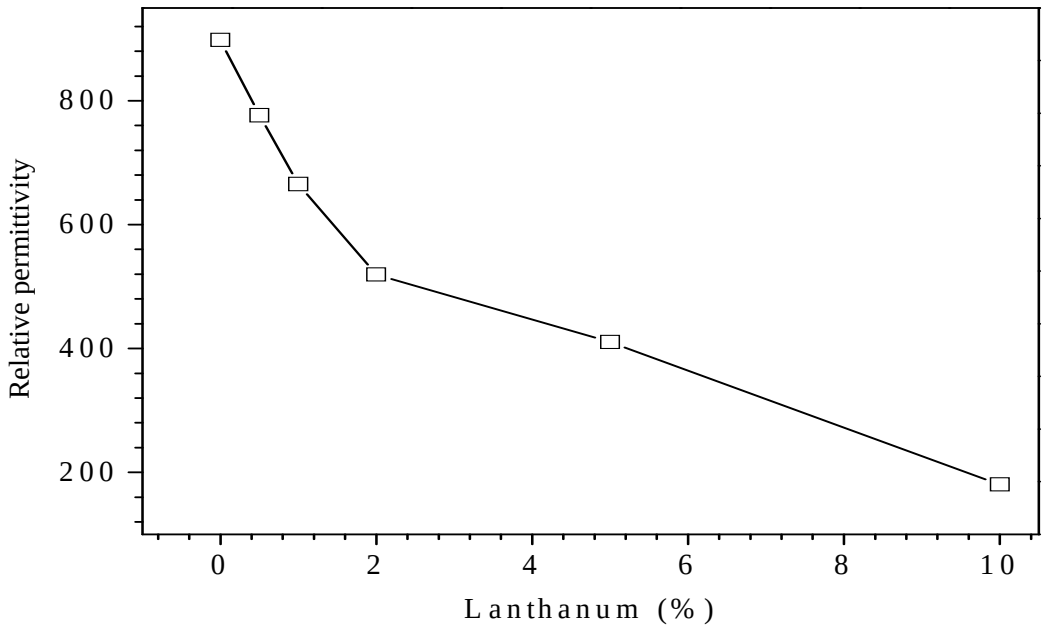

Fig.4.12. Relative permittivity at 5MHz of $Ba_{(1-x)}La_x(Ti_{0.6}Zr_{0.4[1-(5x/8)]})O_3$ with different lanthanum percentage.

There are numerous literatures available for the low percentage of lanthanum doping in perovskites like $BaTiO_3$. Lightly doped samples show semi-conducting properties with high dielectric losses [98]. This is attributed due to either switching from electronic compensation to ionic compensation or oxygen loss from the perovskite. So, in the present case, high tan δ at 0.5 atom % may be due to the advent of these phenomena. However, the composition $Ba_{(1-x)}La_xTi_{0.6[1-(5x/12)]}Zr_{0.4}O_3$ does not show the phenomena of high tan δ at 0.5 atom %. It may be due to the characteristics of Zr^{+4}, which is more stable (valency) than Ti^{+4}. Here, there is no vacancy is created at Zr site.

Fig.4.16 shows the variation of tan δ for the composition $Ba_{(1-x)}La_xTi_{0.6[1-(5x/12)]}Zr_{0.4}O_3$ at 5MHz. Fig.4.17 and Fig.4.18 show the same variation for the compositions $Ba_{(1-x)}La_x(Ti_{0.6[1-x/4]}Zr_{0.4[1-x/4]})O_3$ and $Ba_{(1-x)}La_x(Ti_{0.6}Zr_{0.4[1-(5x/8)]})O_3$ at 5MHz. It may be seen that the value of tan δ has been improved with increase in lanthanum percentage due to the lowering of permittivities by the substitutions. Tan δ for 10 atom % doped samples, were found to be as low as 0.005. This also supports the literature [31].

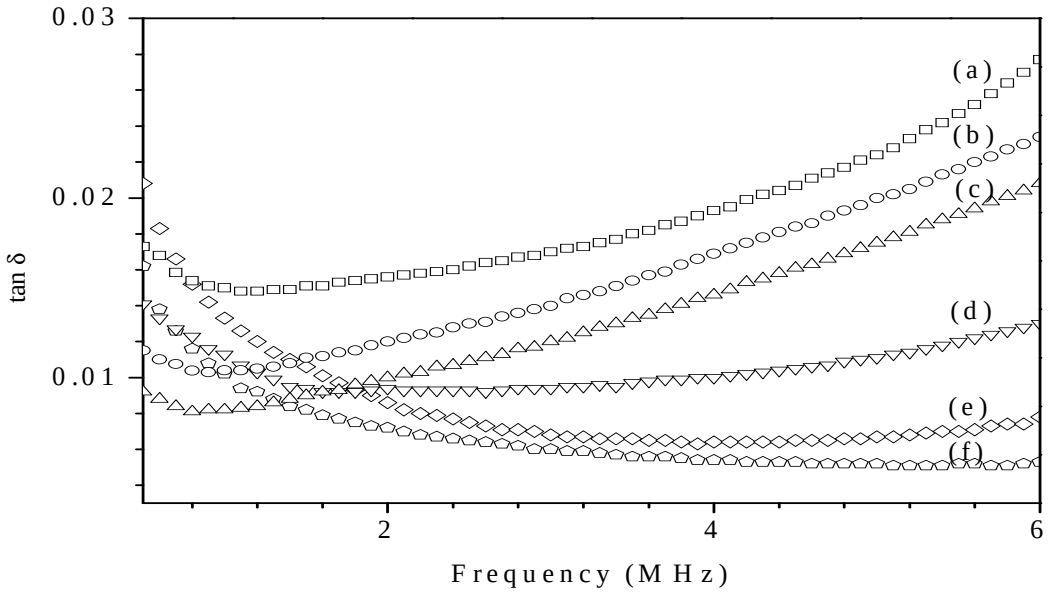

Fig.4.13. tan δ of $Ba_{(1-x)}La_xTi_{0.6[1-(5x/12)]}Zr_{0.4}O_3$ as a function of frequency with x values (a) 0,(b) 0.005, (c) 0.01, (d) 0.02, (e) 0.05 and (f) 0.1.

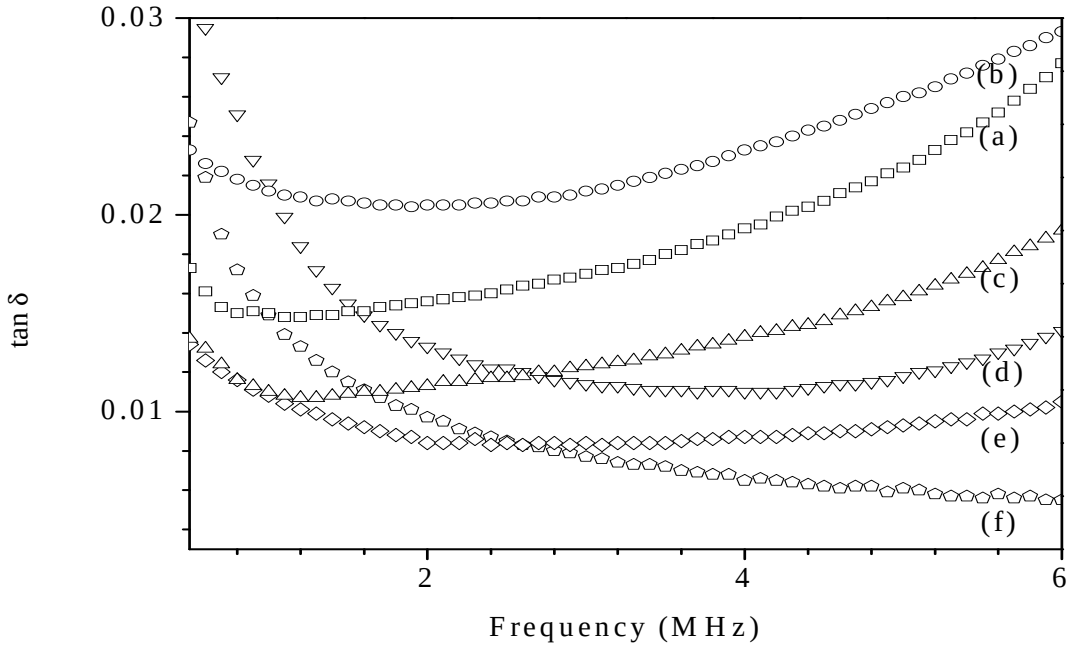

Fig.4.14. tan δ of $Ba_{1-x}La_x(Ti_{0.6[1-x/4]}Zr_{0.4[1-x/4]})O_3$ as a function of frequency with x values (a) 0,(b) 0.005, (c) 0.01, (d) 0.02, (e) 0.05 and (f) 0.1.

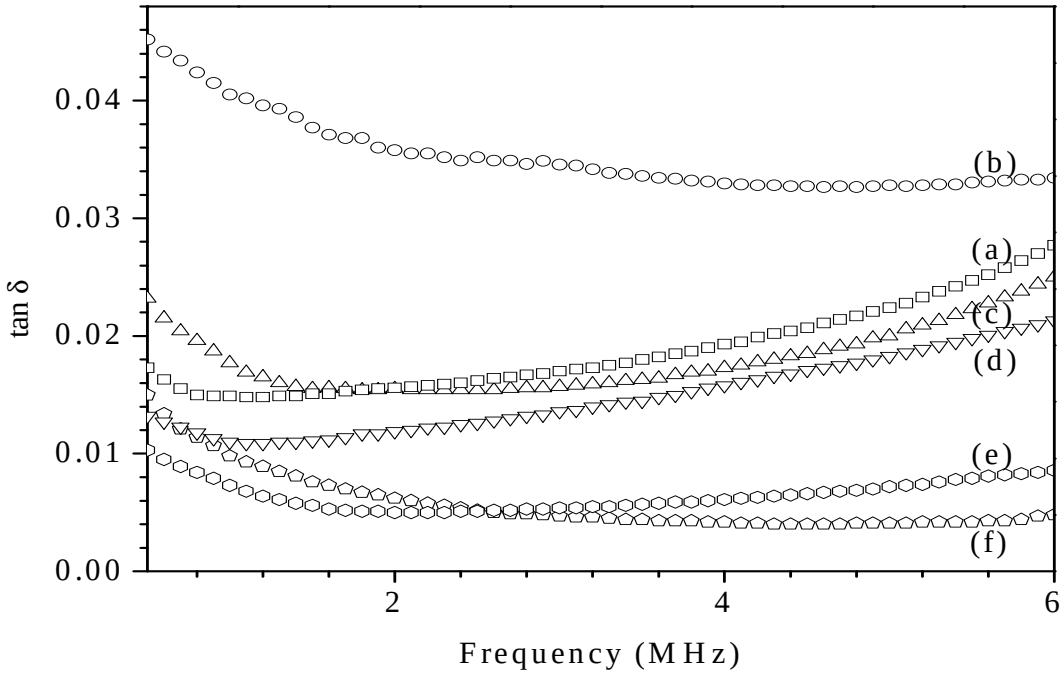

Fig.4.15. tan δ of $Ba_{1-x}La_x(Ti_{0.6}Zr_{0.4[1-(5x/8)]})O_3$ as a function of frequency with x values (a) 0, (b) 0.005, (c) 0.01, (d) 0.02, (e) 0.05 and (f) 0.1.

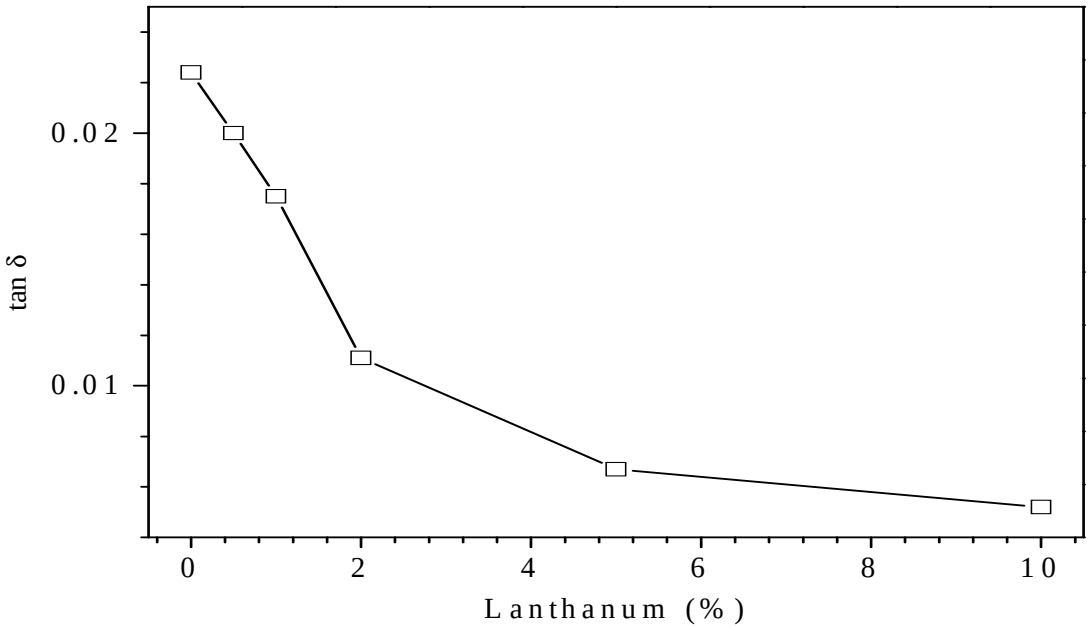

Fig.4.16. tan δ at 5MHz of $Ba_{(1-x)}La_xTi_{0.6[1-(5x/12)]}Zr_{0.4}O_3$ with different lanthanum percentage.

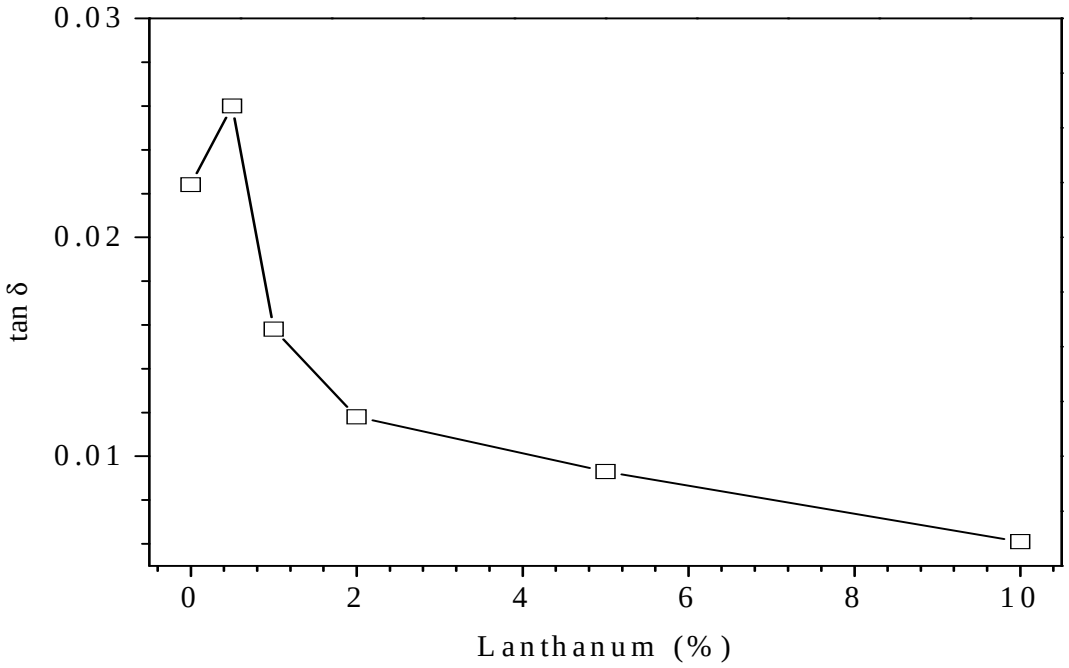

Fig.4.17. tan δ at 5MHz of $Ba_{1-x}La_x(Ti_{0.6[1-x/4]}Zr_{0.4[1-x/4]})O_3$ with different lanthanum percentage.

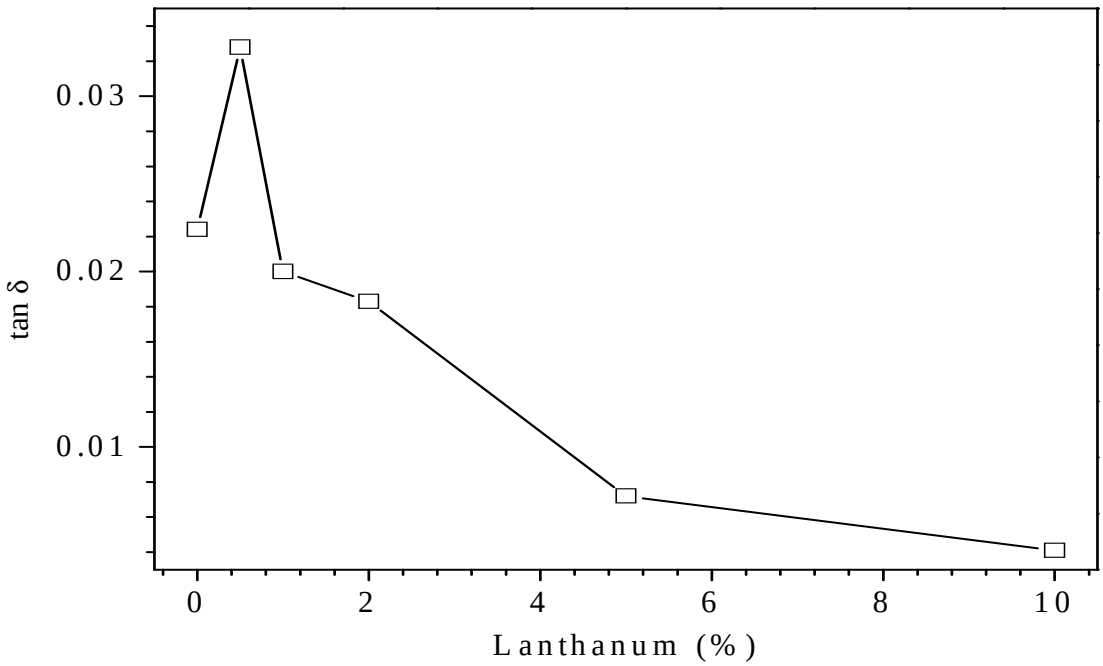

Fig.4.18. tan δ at 5MHz of $Ba_{1-x}La_x(Ti_{0.6}Zr_{0.4[1-(5x/8)]})O_3$ with different lanthanum percentage.

4.2.3 Conclusion

Lanthanum doped $BaTi_{0.6}Zr_{0.4}O_3$ composition x = 0.005, 0.01, 0.02, 0.05 and 0.1 in $Ba_{1-x}La_xTi_{0.6[1-(5x/12)]}Zr_{0.4}O_3$, $Ba_{1-x}La_x(Ti_{0.6}Zr_{0.4[1-(5x/8)]})O_3$ and $Ba_{1-x}La_x(Ti_{0.6[1-x/4]}Zr_{0.4[1-x/4]})O_3$ were prepared. The grain size is reduced upto small amount of La (≤2 at.%) and again increases as doping concentration increases. It is found that both dielectric permittivity (ε_r) and tan δ decreases with increase in lanthanum percentage. Slightly high tan δ at 0.5 atom % may be attributed due to either switching from electronic compensation to ionic compensation or oxygen loss from the perovskite. However, the composition $Ba_{(1-x)}La_xTi_{0.6[1-(5x/12)]}Zr_{0.4}O_3$ does not show the phenomena of high tan δ at 0.5 atom %. It may be due to the characteristics of Zr^{+4}, which is more stable (valency) than Ti^{+4}. High dielectric stability against change in frequency is achieved for the dielectrics.

4.3 Effect of porosity on dielectric properties

Porosity of ceramic materials is very important feature. Industrial processing route does not allow 100% pore free body. Undesired change in any processing parameter leads to porous ceramic body. It is inevitable and difficult to avoid. So it is common practice to study porosity problem in processing.

High material porosity is considered as an advantage only in few cases. For example, a ceramic material of high porosity is very resistant to temperature changes. However, porosity of a ceramic material is a serious defect in high-voltage insulating systems [99]. In many cases, different densities within a ceramic are used to provide a wide continuous range of dielectric constants. Using various levels of porosity in order to alter the effective dielectric constant in the same material allows patterning different dielectric constants into a single unit. It is well known that the relative permittivity decreases with increasing material porosity. Thus, controlling the porosity can yield a spectrum of dielectric constants from a single material [54].

The incorporation of pores significantly degrades the electrical characteristics and breakdown strength of the material. Enhanced electric field in the pores increases the probability of bond breakage on the pore walls and leads to the lowering of the overall breakdown strength [53]. In fact, the dielectric losses are a combined result of electric conduction and orientational polarization of the matter. Some authors tried to treat the effect of moisture on polarization [55]. It is established that the presence of moisture tends to increase the conductivity of material. Dielectric loss factor tan δ increases with the moisture level. In porous media, the porosity introduces in-homogeneity in the bulk, which alters the mechanisms of leakage and breakdown exhibited by the dense analog.

For this thesis work, samples with different density were prepared to investigate the effect of porosity on relative permittivity and dielectric loss.

4.3.1 Experimental procedure

The samples were prepared according to the process described in chapter 3. The sintering temperature was varied between 1200^{o}C to 1400^{o}C to get samples with different porosity. Silver paste was coated, on both sides of sintered ceramic specimen for measurement purpose. The bulk densities of the specimens were between 75%-90% of the theoretical density. The capacitance and loss tan δ of the samples were measured using an HP-4192A impedance analyzer. The dielectric permittivity (ε_r) was calculated using the equation 4.3.

4.3.2 Result and discussion

Dielectric and electrical properties of pore-containing barium titanate zirconate ceramic were studied. Porosity was controlled in the range of 10-25%. The gradual decrease of dielectric constant was noticed as porosity increases, which is quiet expected according to the rule of mixture or the property averaging principle.

The variation of relative permittivity with different apparent porosity at 5MHz for the composition $Ba_{(1-x)}La_xTi_{0.6[1-(5x/12)]}Zr_{0.4}O_3$ is shown in Fig. 4.19. The result shows that the relative permittivity decreases with porosity. Similarly Fig. 4.20 and Fig 4.21 show the relative permittivity variation with apparent porosity at 5MHz for the composition $Ba_{1-x}La_x(Ti_{0.6[1-x/4]}Zr_{0.4[1-x/4]})O_3$ and $Ba_{1-x}La_x(Ti_{0.6}Zr_{0.4[1-(5x/8)]})O_3$, respectively. It is evident, from the slope that the dielectric permittivity decreases slowly with porosity at higher percentage of lanthanum. The porous specimen contains air inside its pores. The relative permittivity of air is comparatively less than dielectrics. As the specimen contains open pores and capacitance measurements were done with silver paste on the surface, it is obvious that relative permittivity will decrease. Polar molecules play an important role in relative permittivity [100]. In low-density samples, the material content is less than the dense analog. When property averaging principle is applied, the mixture gives reduced value of dielectric constant.

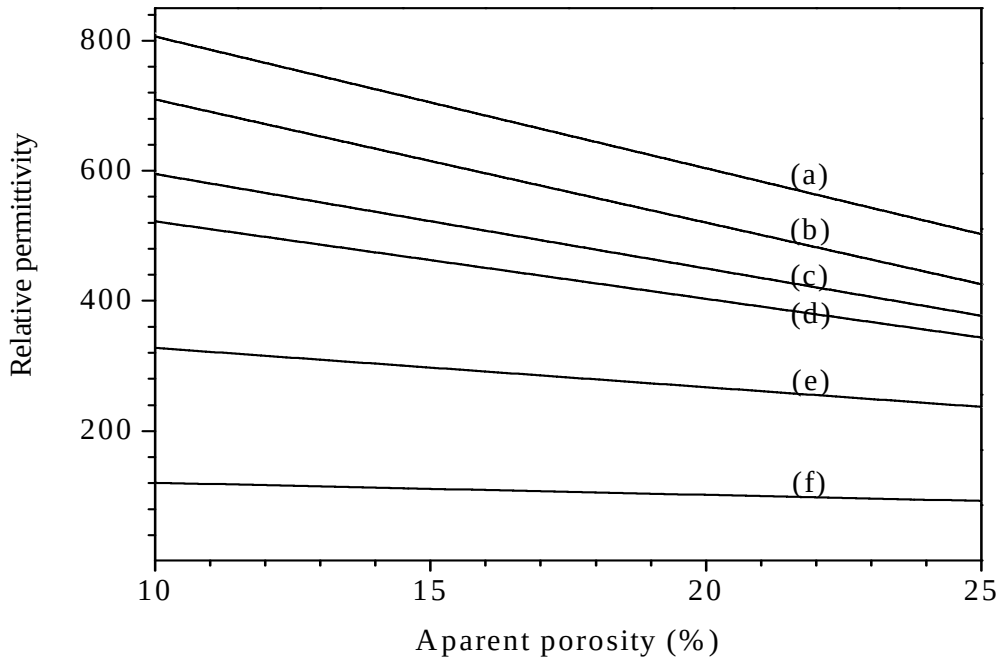

Fig.4.19. Variation of relative permittivity with porosity in $Ba_{(1-x)}La_xTi_{0.6[1-(5x/12)]}Zr_{0.4}O_3$ with x values (a) 0.0, (b) 0.005, (c) 0.01, (d) 0.02, (e) 0.05, (f) 0.1 at 5MHz.

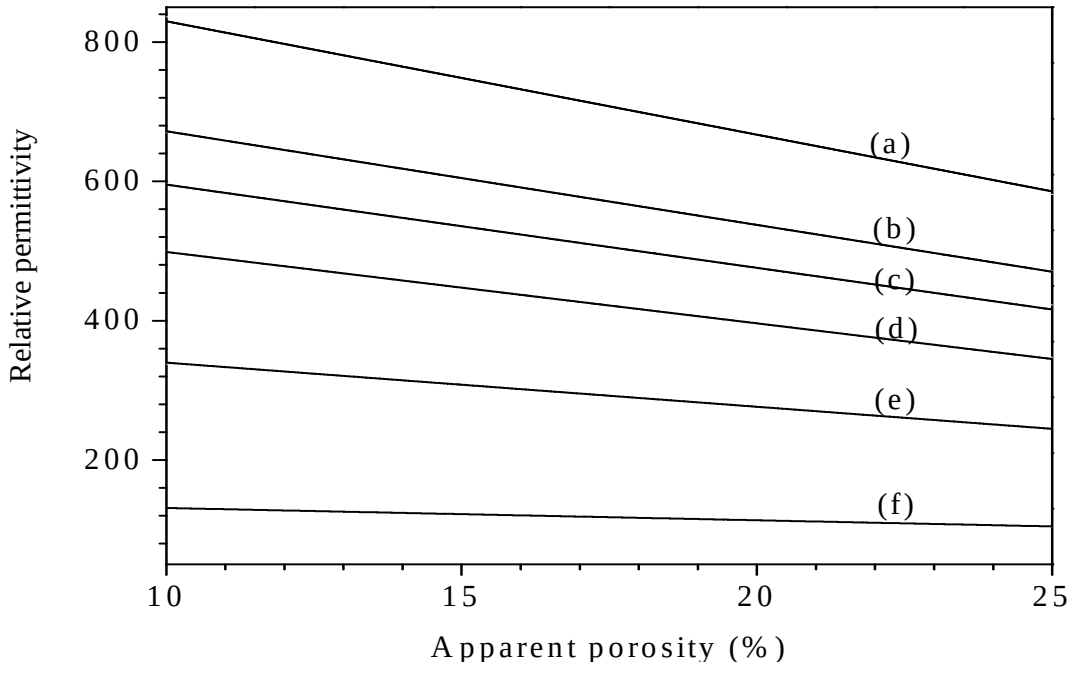

Fig.4.20. Variation of relative permittivity with porosity in $Ba_{1-x}La_x(Ti_{0.6[1-x/4]}Zr_{0.4[1-x/4]})O_3$ with x values (a) 0.0, (b) 0.005, (c) 0.01, (d) 0.02, (e) 0.05, (f) 0.1 at 5MHz.

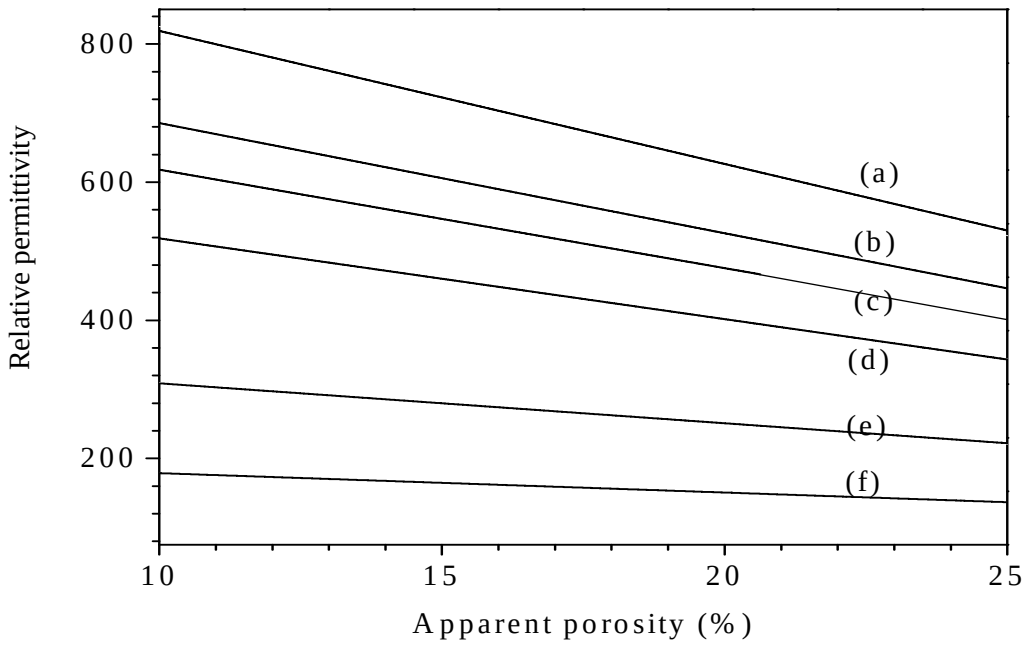

Fig.4.21. Variation of relative permittivity with porosity in $Ba_{1-x}La_x(Ti_{0.6}Zr_{0.4[1-(5x/8)]})O_3$ with x values (a) 0.0, (b) 0.005, (c) 0.01, (d) 0.02, (e) 0.05, (f) 0.1 at 5MHz.

Fig. 4.22 shows tan δ variation with porosity for the composition $Ba_{0.9}La_{0.1}Ti_{0.575}Zr_{0.4}O_3$. Loss increases with increase in porosity. The large number of holes means a large surface area with dangling bonds of the ceramic particles that tend to absorb species and moisture. These bonds absorb electrical energy, which leads to a high tan δ [101].

Fig.4.23. shows variation of tan δ with different porosity. Foreign specimen in pores helps to increase conduction, which in turn increase the loss.

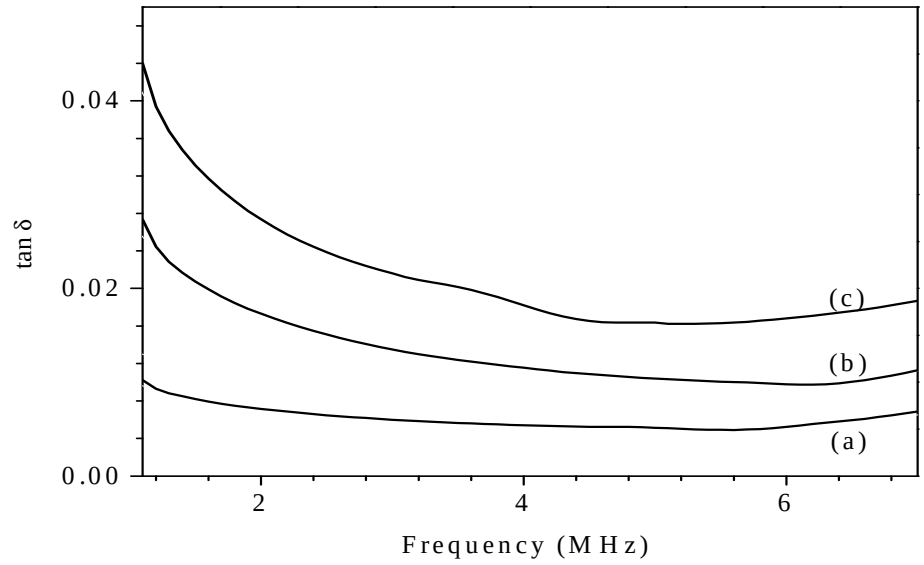

Fig.4.22. tan δ as a function of frequency for $Ba_{0.9}La_{0.1}Ti_{0.575}Zr_{0.4}O_3$ with apparent porosity of (a) 7% (b) 11% and (c) 30%.

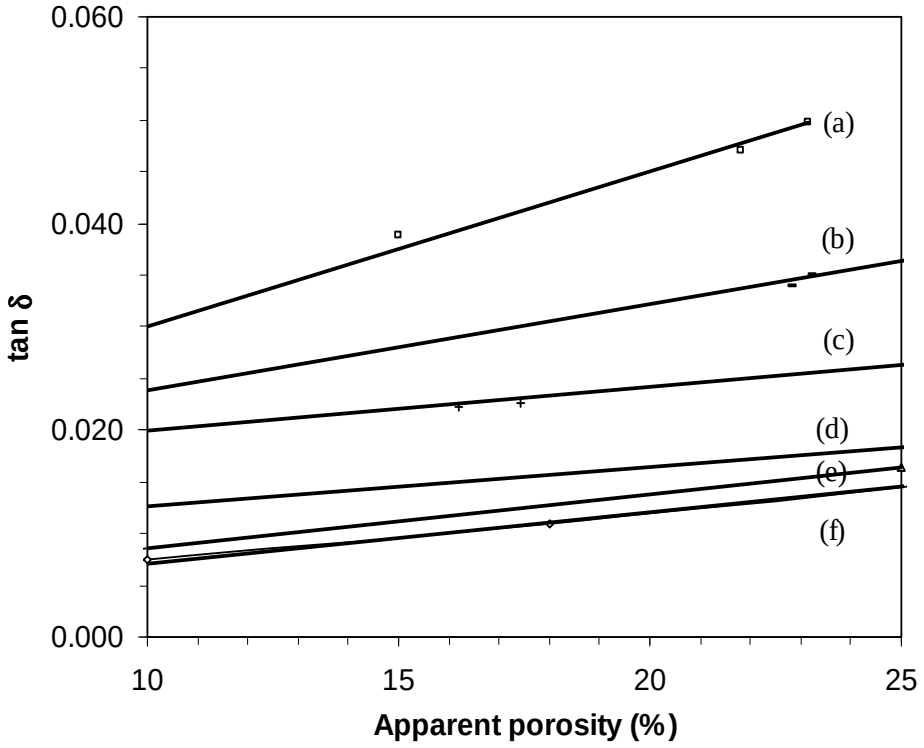

Fig.4.23. Variation of tan δ with porosity in $Ba_{1-x}La_x(Ti_{0.6}Zr_{0.4[1-(5x/8)]})O_3$ with x values (a) 0.0, (b) 0.005, (c) 0.01, (d) 0.02, (e) 0.05, (f) 0.1 at 5MHz.

4.3.3 Conclusion

The dielectric permittivity and tan δ of the ceramics for different porosity was investigated. It is noted that dielectric permittivity decreases and tan δ increases with increase in porosity.

4.4 Relaxor behaviour of lanthanum doped $BaTi_{0.6}Zr_{0.4}O_3$

In $Ba(Ti,Zr)O_3$ ceramics, at higher Zr content, the dielectric constant versus temperature curve becomes broad at the vicinity of the transition temperature T_m, which is caused by distribution of Zr ions in the Ti sites and mechanical stress in the grain. In this case, the macrodomains could be divided into the microdomains with increasing Zr concentration, which result in the appearance of the relaxor behavior [26]. The more the substitution is in the B-site, the greater is the relaxor effect [102]. Regarding the values of T_m, Ti substitution by Zr causes a decrease of it owing to the increasing of cation size [23, 103].

It has been reported that the Curie temperature in the materials shifted towards lower temperature with increased content of La substituted at Ba sites upto a critical concentration that varied with the sintering temperature for $BaTiO_3$ [104]. Tc decreases approximately linearly with increase in lanthanum percentage [105]. It is being anticipated as replacement of ferroelectric active TiO_6 octahedra by Ti vacancy (La doping) and by non-ferroelectric ZrO_6 octahedra disrupt the cooperative linking between TiO_6 unit [98].

In this work, the influence of lanthanum on the relaxor behavior of the system was investigated.

4.4.1 Experimental procedure

La_2O_3-doped barium zirconate titanate $Ba_{1-x}La_x(Zr_{0.4}Ti_{0.6[1-(5x/12)]})O_3$ ceramics with x= 0.005, 0.05 and 0.1 were prepared. The process has been described elaborately in chapter 3. Silver paste was coated on both sides of sintered ceramic specimen for dielectric measurement.

Liquid nitrogen was used for achievement of low temperature. The sample was placed inside a special airtight chamber and the chamber was put in the liquid nitrogen environment. The temperature was recorded with a temperature indicator at every 10 K

interval. The capacitance and tan δ at different frequencies was measured using impedance analyzer.

4.4.2 Result and discussion

The temperature dependence of relative permittivity of the ceramics was investigated. Fig. 4.24 shows the relative permittivity and tan δ variation as a function of temperature for the composition $Ba_{0.995}La_{0.005}Ti_{0.59875}Zr_{0.4}O_3$. Similarly Fig. 4.25 and Fig. 4.26 show the temperature dependence of relative permittivity and tan δ for the composition $Ba_{0.95}La_{0.05}Ti_{0.5875}Zr_{0.4}O_3$ and $Ba_{0.9}La_{0.1}Ti_{0.575}Zr_{0.4}O_3$, respectively.

The results show that the phase transition temperature T_m is suppressed with increasing La content. However, for 5 and 10 at.% doped samples below 120^oK could not be performed due to the limitation of the instrument used. The measurement frequency range was from 5.3 KHz to 1.1 MHz. The results show that the temperature T_m corresponding to the maximum value of the relative permittivity is decreased with increasing La content. The transition temperature T_m of 0.5 at.% doped sample is located at 203 K where as 5 at.% doped sample is located at 149 K at 1.1 MHz frequency.

The dielectric response of the ceramics at various frequencies shows a diffuse phase transition around the transition temperature T_m. A diffuse phase transition is generally characterized by broadening in the dielectric constant versus temperature curve, relatively large separation between the maximum of the real and imaginary parts of the dielectric spectrum, deviation from Curie Weiss law in the vicinity of T_m and frequency dispersion of both relative permittivity and tan δ [14, 20, 106].

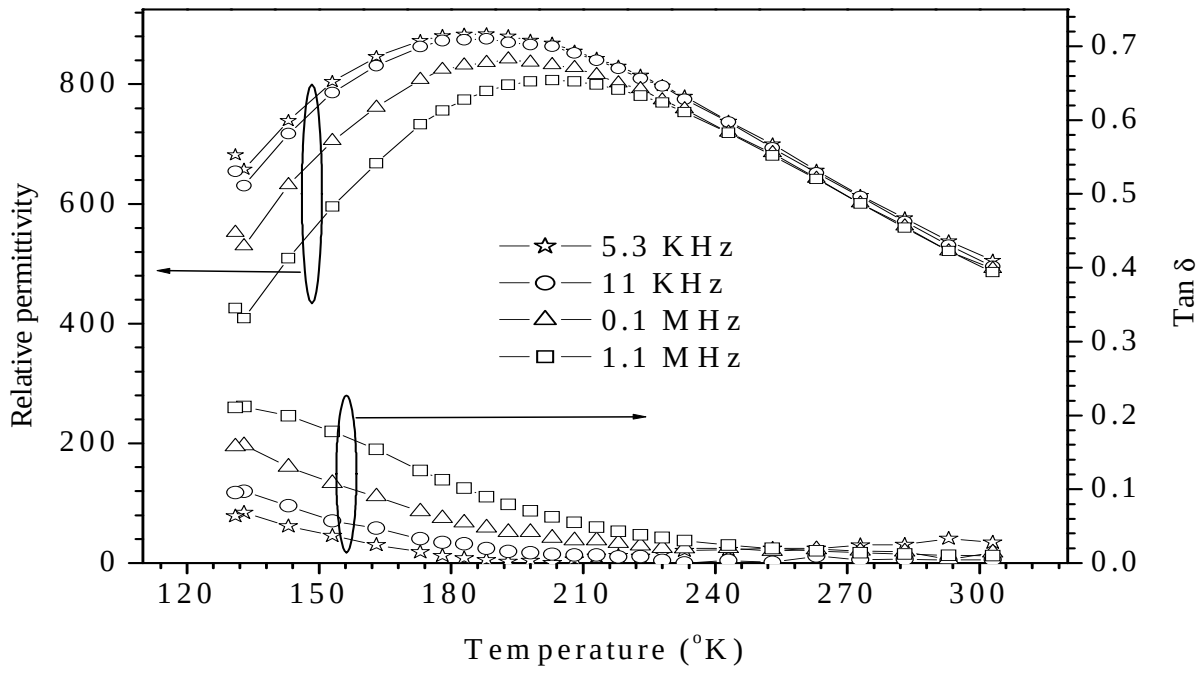

Fig.4.24. Relative permittivity and tan δ as a function of temperature for the composition $Ba_{0.995}La_{0.005}Ti_{0.59875}Zr_{0.4}O_3$.

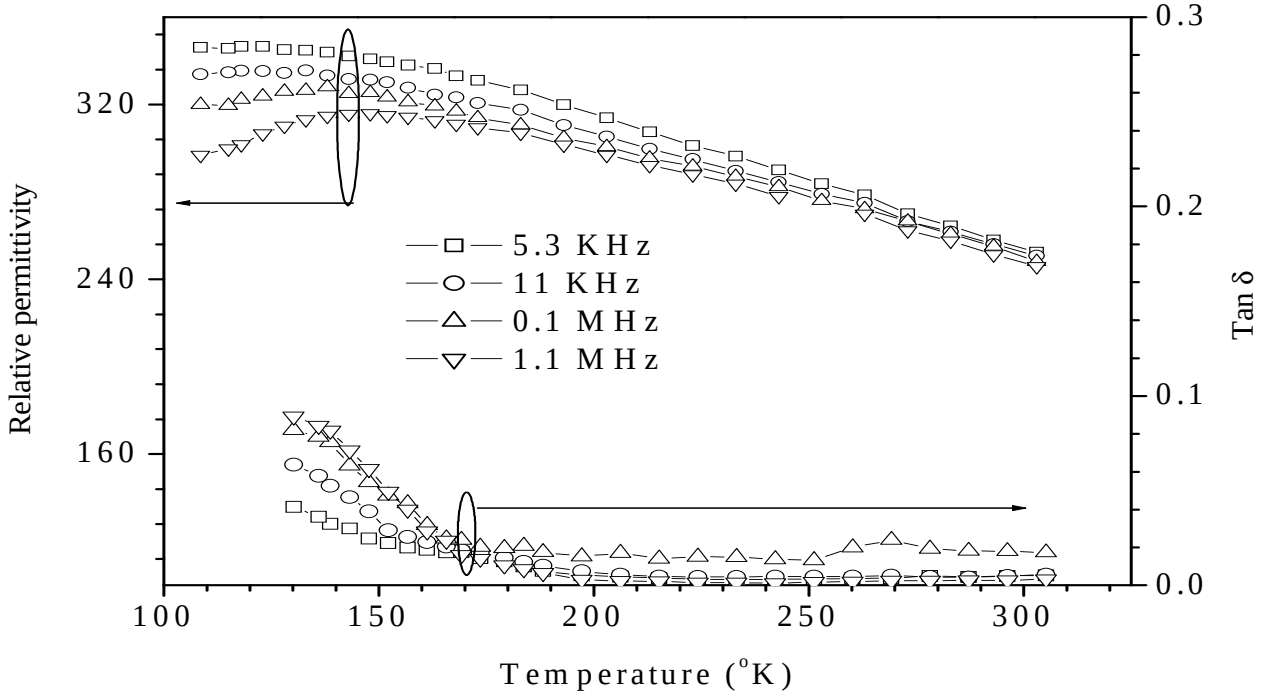

Fig.4.25. Relative permittivity and tan δ as a function of temperature for the composition $Ba_{0.95}La_{0.05}Ti_{0.5875}Zr_{0.4}O_3$.

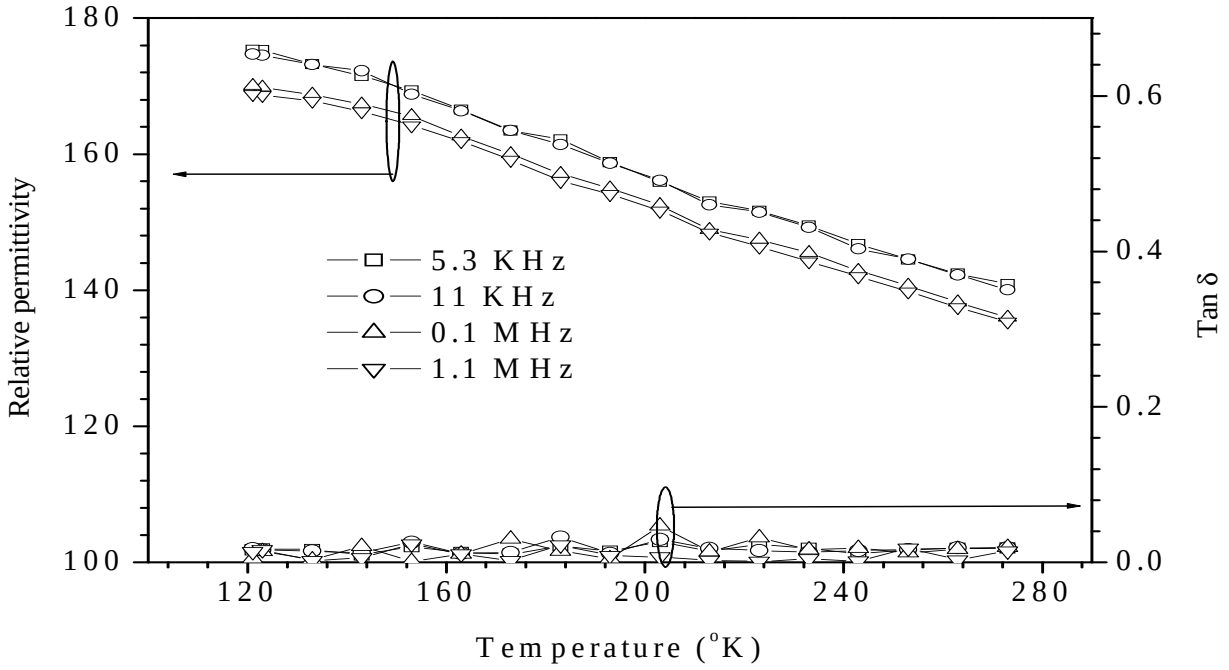

Fig.4.26. Relative permittivity and tan δ as a function of temperature for the composition $Ba_{0.9}La_{0.1}Ti_{0.575}Zr_{0.4}O_3$.

At temperature near to the transition temperature, the permittivity becomes high. Looking at the dielectric behavior, the low-temperature (temperatures below T_m) frequency dispersion of the dielectric maximum clearly demonstrates a relaxation nature, namely, a relaxor-type diffused permittivity, for the ceramics. The T_m of 5 at.% La-doped sample increases from 119 K at 5.3 KHz to 149 K at 1.1 MHz. Similarly 0.5 atom % La-doped sample increases from 185 K at 5.3 KHz to 203 K at 1.1 MHz. It is known that dielectric permittivity of normal ferroelectric above Curie temperature follows the Curie-Weiss law. A modified Curie–Weiss law [107-109] has been proposed to describe the diffuseness of a phase transition as follows:

$$\frac{1}{\varepsilon} - \frac{1}{\varepsilon_r} = \frac{(T - T_m)^{\gamma}}{C'}, \qquad (4.4)$$

where γ and C' are assumed to be constant. The parameter γ gives information on the character of the phase transition: for $\gamma = 1$, a normal Curie–Weiss law is obtained, $\gamma = 2$ describe a complete diffuse phase transition.

The plots of $\ln(\frac{1}{\varepsilon}-\frac{1}{\varepsilon_m})$ as a function of $\ln(T\text{-}T_m)$ for 0.5 atom % and 5 atom % La-doped samples are shown in Fig. 4.27. A linear relationship is observed with γ value of 1.89 and 1.94 respectively for the above compositions. For the sample $Ba_{0.995}La_{0.005}Ti_{0.59875}Zr_{0.4}O_3$, the values of γ decreases from 1.94 to 1.89 when frequency increases from 5.3 KHz to 11 KHz, which clearly implies a strong diffuse phase transition.

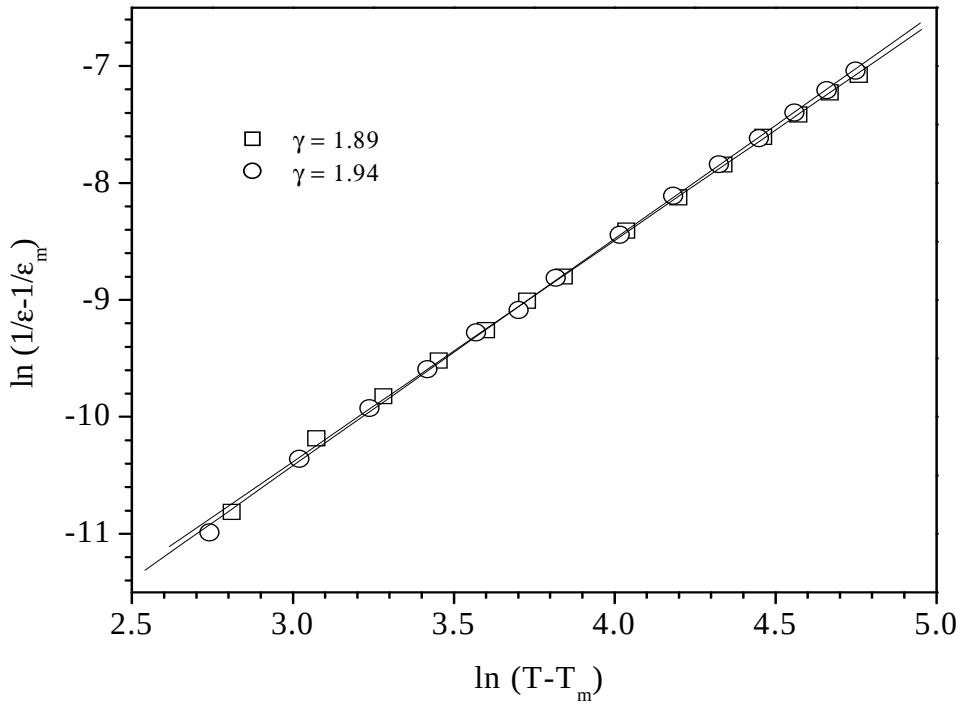

Fig.4.27. $Ln(1/T\text{-}1/T_m)$ Vs $Ln(1/\varepsilon\text{-}1/\varepsilon_m)$ for the composition $Ba_{0.995}La_{0.005}Ti_{0.59875}Zr_{0.4}O_3$ ( ) and $Ba_{0.95}La_{0.05}Ti_{0.5875}Zr_{0.4}O_3$ (O) at 11KHz.

The plot of ln (v) versus T_m is shown in Fig. 4.28 for 0.5 atom % and 5 atom % La-doped samples. The nonlinear ln (v) versus T_m curve indicates that the data cannot be fitted with a simple Debye equation. In order to analyze the relaxation features of the ceramics, the experimental data were fitted using the Vogel–Fulcher formula [107, 108]:

$$v = v_o \exp[\frac{E}{k_B(T-T_f)}] \qquad (4.5)$$

where v_o is the attempt frequency, E is a measure of average activation energy, and k_B is the Boltzmann's constant, and T_F is the freezing temperature.

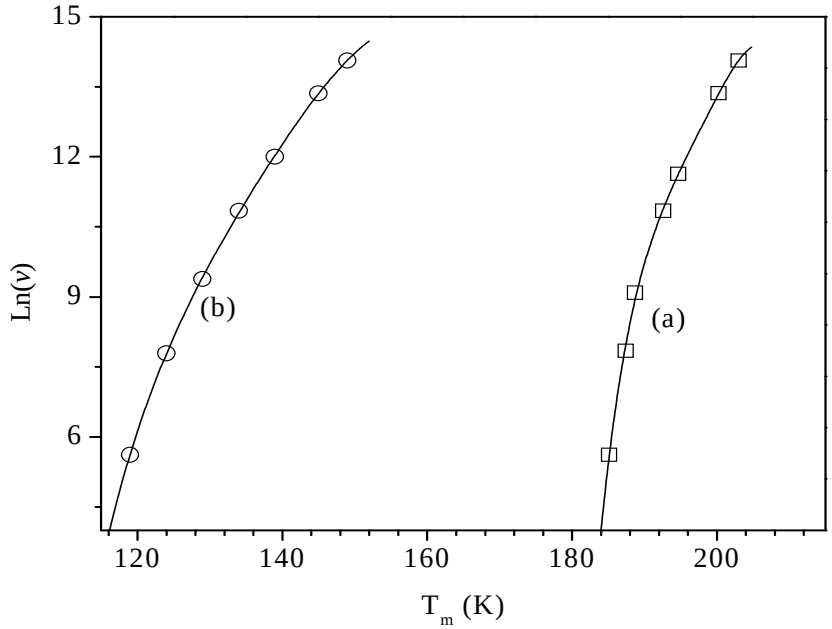

Fig.4.28. T_m versus Ln(ν) for (a) $Ba_{0.995}La_{0.005}Ti_{0.59875}Zr_{0.4}O_3$ and (b) $Ba_{0.95}La_{0.05}Ti_{0.5875}Zr_{0.4}O_3$.

The empirical relaxation strength describing the frequency dispersion of T_m, is defined by the equation:

$$\Delta T_{res} = T_{m(1\ MHz)} - T_{m(5..3KHz)} \qquad (4.6)$$

where ΔT_{res} is the difference of T_m at two different frequencies. The values of ΔT_{res} for 0.5 at.% and 5 at.% La-doped samples were 18 and 30 K, respectively, indicating a relaxor-like ferroelectric.

The solid solution of La doped $Ba(Ti,Zr)O_3$, contains two kinds of substitutions, isovalent and heterovalent. Ba^{+2} and La^{+3} ions occupy the A-site of the structure. Similarly Zr^{+4} and Ti^{+4} ions occupy the B-site. The ionic radius of Zr^{4+} is larger than that of Ti^{4+}. T_m shifts to lower temperature as lanthanum percentage increases. The relaxor behavior as observed in these ceramics can be induced by many reasons such as a microscopic composition fluctuation, the merging of micropolar regions into macropolar regions, or a coupling of order parameter and local disorder mode through the local strain

[5, 14, 106]. Vugmeister *et.al.* [110] reported that the randomly distributed electrical field/or strain field in a mixed oxide system was the main reason leading to the relaxor behavior. Concerning the off-valent substitutional A-site solid solutions, replacement of Ba^{2+} by the smaller La^{3+} involves concomitant vacancy due to the requirement of charge neutrality. The number of vacancies increased with La^{3+} content. The unit cell parameters slightly decrease with La, due to the smaller size of La^{3+}. The resulting shrinkage of the unit cell gives rise to smaller shift of the tetravalent cation out of the octahedron centre, leading to a strong decrease of T_m, according to the empirical relation [21], where T_m and $(\Delta z)^2$ are directly correlated. (Δz is the displacement of the cation from the centre of the B-site to its position in the polar phase).

When the incorporation of La^{3+} in the lattice is via Ti-vacancies and ionic compensation mechanism, a partial disconnection of the ferroelectric-active corner shared TiO_6 octahedra [98], results, a compositionally more disordered state and the ferroelectric phase transition becomes smeared out by the chemical inhomogeneity. Besides, the charge defects generated by partially substituted A-site, may affect the Zr^{4+}–Ti^{4+} substitution, enhancing the intrinsic homogeneous disorder, which exists even in perovskites with iso-valent substitutions in A-site. It is this homogeneous disorder which results in a diffused phase transition [111]. The strong decrease in T_m with increasing La^{3+} content comes from the La^{3+}– Ba^{2+} substitution, like other alkaline-earth small cations [112]. The shrinkage of the cell gives rise to smaller shift out of the octahedron, accentuated by the greater size of Zr^{4+}, comparatively to that of Ti^{4+}, which limits the displacement, leading to a decrease of Δz and, consequently, of T_m.

In the heterovalent substitutions, the number of vacancies increases with increasing lanthanum. In *B*-site vacancies, the degree of ordering in *B*-site is modified and the coherence length decreases. The relaxor effect is probably due to this coexistence of B-site disordered domains and ordered vacancy-cation clusters. Concerning the value of T_m, as was the case for BT–BZ system with high substitution rates, it decreases. However, this decreasing when the substitution rate of La^{3+} for Ba^{2+} increase is accompanied with an increase of ΔT_m. The relaxor effect is then enhanced, even though

the corresponding relaxor parameters are somewhat less good than comparative compositions with ions having a lone pair like Bi^{3+} or Pb^{2+} [113, 114].

It has been reported that as La-dopant content increase, all the variation tendencies point to larger departures from classic ferroelectric behavior. The degree of the diffuseness of the phase transition behavior is enhanced with the adding of La_2O_3 dopant. The phenomena can be expected that the site-occupation ratio of A/B equals $1/(1-x/4) > 1$. The substitution of La^{3+} for A-site Ba^{2+} ions results in the disordered distribution of A-site ions. Therefore, the chemical inhomogeneity of the ceramics and the distortion of the lattice of perovskite structure are originated. The random electric field is enhanced and the degree of ferroelectric relaxor behavior is increased with increasing of Lanthanum [31].

4.4.3 Conclusion

The La substitution in $BaTi_{0.6}Zr_{0.4}O_3$ affects the transition temperature T_m by shifting the T_m to a lower temperature region with increasing La content. A γ value of 1.89 implies diffuse transition behaviour of the ceramics and show relaxor-like behavior with a strong frequency dispersion of the (T_m). The relative permittivity is suppressed by addition of Lanthanum. The ceramics obey the empirical Vogel–Fulcher relation, which confirms the relaxor behavior.

4.5 Resistivity and current density at low electric field

4.5.1 Introduction

For many years, A and B site dopants have been used to modify the electrical properties (dielectric, resistivity, etc.) of ABO_3 based ceramics. However, in many cases the doping mechanism(s) and defect chemistry remain poorly understood and/or controversial.

In particular, the doping mechanism of La in $BaTiO_3$ has been widely debated [115-117]. $BaTiO_3$ can be converted to n-type semiconductor when it is doped with a small portion (< 0.5 at.%) of trivalent or pentavalent cations, such as La^{+3},Y^{+3} or Nb^{+5}, in the general formula $Ba_{1-z}A_zTiO_3$ [118]. Lightly-doped $BaTiO_3$ ceramics, prepared in air and quenched from 1350^{o}C has led to the belief that La can act as a 'donor' dopant [115, 116] according to the equation:

$$Ba^{2+} = \dot{L}a^{3+} + e^{-} \qquad (4.7)$$

with general formula $Ba_{1-x}La_xe_xTiO_3$ with [Ba + La] / [Ti] = 1. In contrast, when $BaTiO_3$ was doped with 0.53 at.% of La, it was converted to a semiconductor by sintering at 1540^{o}C for 2 h in air [104]. More heavily doped samples (>0.5 atom%) prepared in air were electrically insulating and this has been attributed to a 'switch' from the electronic 'donor-doping' to an ionic compensation mechanism, where

$$Ba^{2+} + 1/4Ti^{4+} = \dot{L}a^{3+} \qquad (4.8)$$

of general formula $Ba_{1-x}La_xTi_{1-x/4}O_3$ with [Ba+La]/ [Ti]>1 [115, 116].

Compositions prepared according to the electronic compensation mechanism give phase mixtures. No evidence for the precipitation of secondary phases for any $Ba_{1-x}La_xTi_{1-x/4}O_3$ composition heated in O_2, Ar or air at 1400^{o}C, suggesting the primary mode of incorporation of La into $BaTiO_3$ at all concentrations is via Ti vacancies. Such materials are expected to be electrical insulators at room temperature given the immobility of Ti-vacancies [29, 119, 120]. However, in many cases semi-conductivity is observed. An alternative mechanism was proposed by Morrison *et.al*.[29], namely, oxygen loss which is responsible for semiconductivity. The amount of oxygen loss is too small to detect using thermo-gravimetry but has a significant influence on the colour and

electrical properties of La-doped $BaTiO_3$ ceramics. It is noteworthy, that oxygen loss in other dielectric-based barium titanates, e.g. $Ba_2Ti_9O_{20}$ and $BaTi_4O_9$ is readily accepted [121] and is known to enhance dielectric losses through the introduction of electrical conductivity via:

$$O^{2-} = 1/2O_2 + 2e^- \quad (4.9)$$

Oxygen deficiency can occur at high temperature (>1350^{o}C, in air) and/or in reducing atmosphere [122, 123] The electron generated reduce Ti^{+4} ion to Ti^{+3} and produced dark coloured, n-type semiconducting material of general formula $BaTi^{+4}_{1-y}Ti^{+3}_yO_3$-$y_{/2}$ [120]. However, heating the samples in air > 1350^{o}C caused a change to leaky dielectric behaviour, attributed to oxygen loss. Oxygen nonstoichiometry / deficiency within the ceramics sintered in air were avoided by heating at 1200^{o}C, instead of 1350^{o}C. Alternatively oxygen lost from ceramics heated in air at 1350^{o}C was regained by post-annealing in oxygen at 1350^{o}C [120].

The electrical properties are very sensitive to oxygen non-stoichometry and room temperature resistance is heavily dependent on degree of re-oxidation that occur during cooling and therefore on kinetic variable such as the cooling rate. Thus semiconductivity can be obtained only by the rapid quenching of lightly doped (<1 atom %) samples from high temperature >1350^{o}C, where as slow cooled sample exhibit much higher room temperature resistance. In contrast to this a semi-conducting barium titanate ceramics doped with 0.53% La was obtained by sintering at 1540^{o}C where as sintering at 1460^{o}C yield only insulating materials for this composition. Semi-conducting-insulating transition closely relates to incorporation of donor into the grains and to the resultant grain size, which were significantly affected by sinterability of the barium titanate starting powders and sintering conditions used [104].

However in general, greater addition of donor elements over a certain critical concentration (about 0.3-0.4 atom %) barium titanate has been found to revert back to an insulator [97]. Several models has been proposed, to account for this interesting phenomenon: precipitation of non conducting phases [124, 125], grain size effect arising

from kinetic processes during firing and cooling [126], compensation of the donors by cation vacancies [127, 128] and segregation of dopants at grain boundaries [129].

Rare-earth doped material become more insulative when Ba/Ti >1 and grain size reduced with increase in rare-earth accompanied by grain growth inhibition [94, 130]. In addition to the above complexities in the characterization technique and methodologies, La-doped barium titanate ceramics show two unusual properties neither of which has been fully explained. First the resistance passes through a minimum with increasing rare-earth contain, the minimum supposedly coincides with a change in doping mechanism, from an electronic donor doping mechanism at small rare-earth content which leads to the reduction in resistance, to an ionic compensation mechanism (Ti vacancy), at high rare earth content which result in subsequent increase in resistance.

In this work, different La doped $BaTi_{0.6}Zr_{0.4}O_3$ was prepared with ionic compensation mechanism. The effect of Lanthanum in the resistivity and current density characteristics were studied.

4.5.2 Experimental procedure

The samples were prepared according to the process described in chapter 3. The cooling was controlled to be very slow to avoid oxygen loss from the samples. The bulk densities of the specimens were as high as 90% of the theoretical density.

Resistivity study: Sintered pellets samples were used to determine resistivity. Electrodes were painted on the surface of the sample using a conducting silver paste. The High Reistance Meter (model: 4339 B, Agilent Technologies USA), with a maximum voltage 1KV, was used to measure the DC resistivity. A special sample holder with 1mm diameter electrode was used for the measurement purpose.

The current density was measured according to the formula:

$$J = \frac{I}{A} \qquad (4.10)$$

where J is the current density, I the current and A the capacitor area.

The resistivity was calculated using formula:

$$\rho = \frac{V * A}{I * L} \qquad (4.11)$$

where ρ is the resistivity, A the capacitor area, V the applied voltage, L the thickness and I the leakage current.

4.5.3 Result and discussion

The colour of 0.5 atom % doped samples for all the compositions were slightly bluish white compared to yellowish white in case of higher % La-doped samples.

The current was measured at an interval of 25 volts. The samples were put in the electric field for 60 seconds and then the current values were noted down at each step. The current densities and resistivity were calculated according to the equation 4.10 and equation 4.11 respectively.

Fig.4.29 shows the resistivity of the composition $Ba_{(1-x)}La_xTi_{0.6[1-(x/4)]}Zr_{0.4(1-(x/4)]}O_3$ with different Lanthanum percentage at 2.5 KV/cm. Resistivity was lowest in 0.5 atom % lanthanum composition and then resistivity increases rapidly with lanthanum concentration.

Current density and resistivity with electric field for the composition $Ba_{0.9}La_{0.1}Ti_{0.585}Zr_{0.39}O_3$ is shown in Fig.4.30. At low electric field the current density displays nearly ohmic behaviour. Current densities increases with applied electric field due to the increase in field assisted charges.

Current density and resistivity with electric field for the composition $Ba_{0.95}La_{0.05}Ti_{0.5925}Zr_{0.395}O_3$ and $Ba_{0.98}La_{0.02}Ti_{0.597}Zr_{0.398}O_3$ has been shown in Fig.4.31 and Fig.4.32, respectively. They show same behavior as stated above for Fig. 4.30.

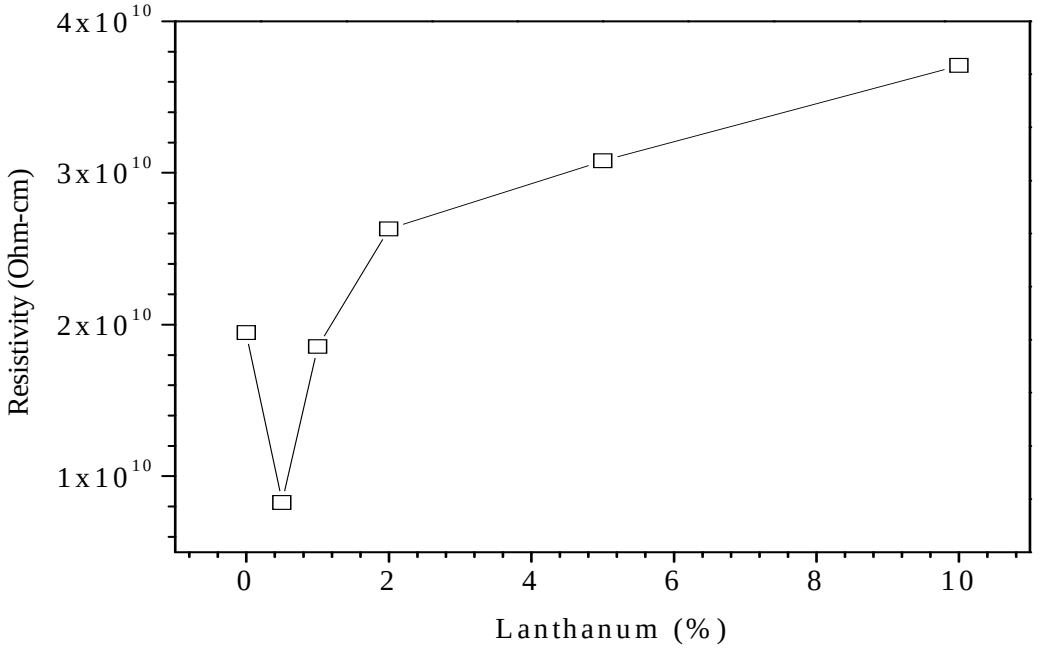

Fig.4.29. Resistivity of the composition $Ba_{(1-x)}La_xTi_{0.6[1-(x/4)]}Zr_{0.4(1-(x/4)]}O_3$ with different lanthanum percentage at an electric field of 2.5 KV/cm.

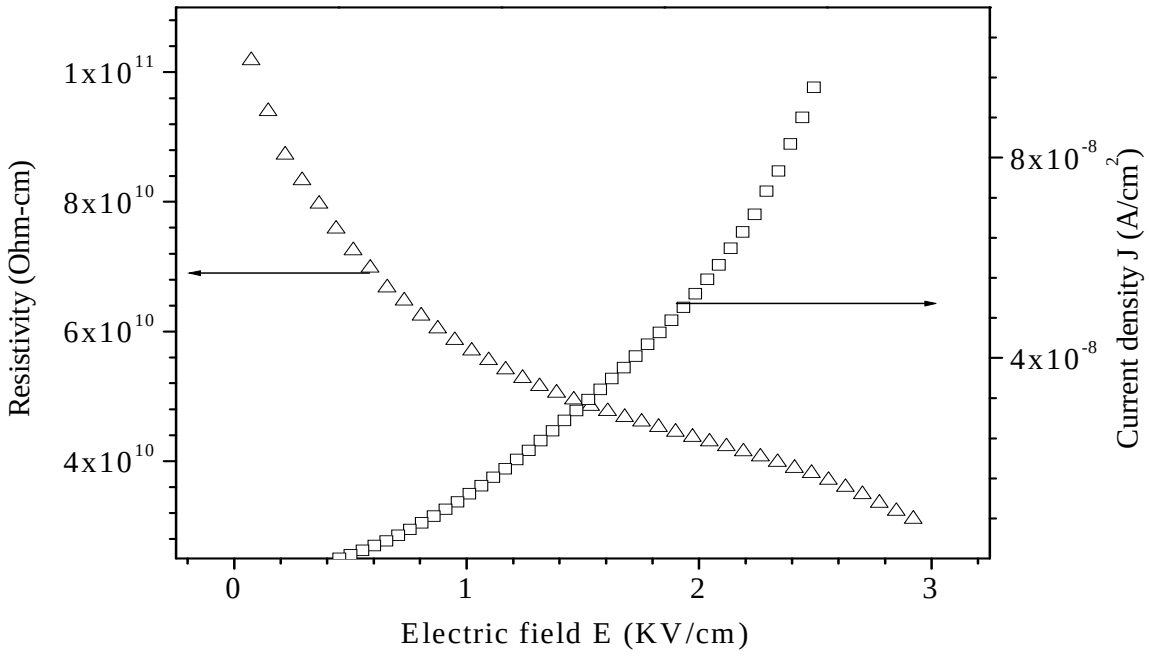

Fig.4.30. Current density and resistivity with electric field for the composition $Ba_{0.9}La_{0.1}Ti_{0.585}Zr_{0.39}O_3$.

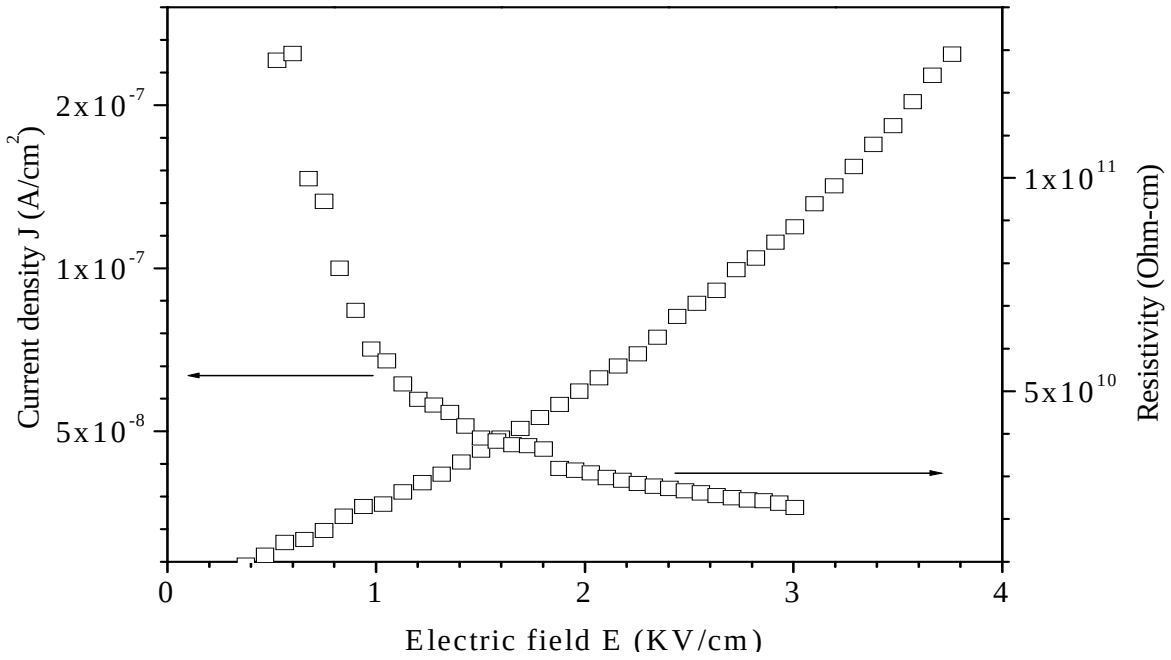

Fig.4.31. Current density and resistivity with electric field for the composition $Ba_{0.95}La_{0.05}Ti_{0.5925}Zr_{0.395}O_3$.

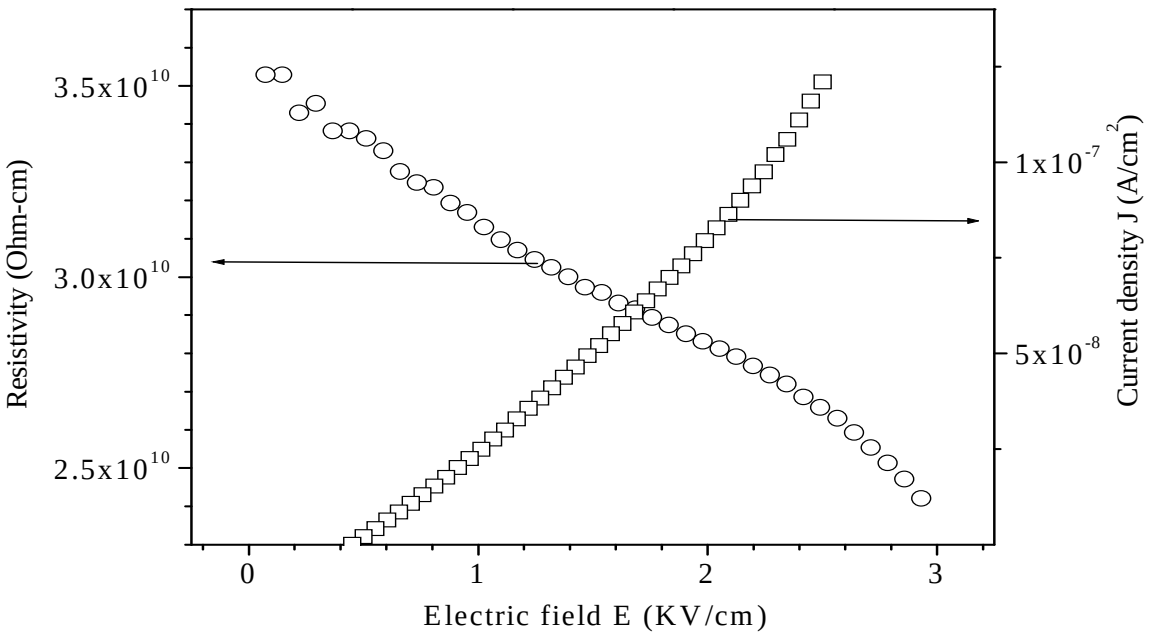

Fig.4.32. Current density and resistivity with electric field for the composition $Ba_{0.98}La_{0.02}Ti_{0.597}Zr_{0.398}O_3$.

4.5.4 Conclusion

The compositions were formulated according to the formula $A_{1-x}La_xB_{1-x/4}O_3$. However, semiconductive properties were not found in the lightly doped samples. Resistivity is slight increased for higher lanthanum substitutions. At low electric field the current density displays nearly ohmic behaviour.

CHAPTER 5

ARTIFICIAL NEURAL NETWORK MODELLING

5.1 Introduction

Artificial Neural Network (ANN) with adaptability and nonlinearity are well suited to estimate tasks, particularly where the equation describing the function is unknown. In function estimation application ANN acts as a model, which stands for the system it represents, typically to predict or control it. This chapter employs a Multilayer Feedforward Network (MFN) with Back Propagation Algorithm (BPA) to model the dielectric properties of $BaTiZrO_3$ based system. It seems to be of great interest, in particular, when a rigid theoretical basis or mathematical relationship is not available in advance.

ANN typically consists of a set of processing elements called neurons that interact by sending signals to one another along weighted connections. The connection weights, which can be determined adaptively, specify the precise knowledge representation. Usually it is not possible to specify the connection weights beforehand, because knowledge is distributed over the network. Therefore, a learning procedure is necessary in which the strengths of the connections are modified to achieve the desired form of activation function. The learning procedure is divided into three types: supervised, reinforced and unsupervised. The type of error signal used to train the weights in the network defines these three types of learning. In supervised learning, an error scalar is provided for each output neuron by an external ‘teacher’, while in reinforced learning the network is given only a global punish or reward signal. In unsupervised learning, no external error signal is provided, but instead internal errors are generated between the neurons, which are then used to modify the weights. In supervised learning the weights connecting neurons, are set on the basis of detailed error information supplied to the network by an external teacher. In most cases, the network is trained using a set of input-output pairs, which are examples of the mapping that the network is required to learn to compute. The learning process may therefore be viewed as fitting a function and its

performance can thus be judged on whether the network can learn the desired function over the interval represented by the training set and to what extent the network can successfully generalize away from the points that it has been trained on.

5.2 Multilayer Feedforward Network

The simplest network capable of supervised learning is a two-layer feedforward network consisting of input layer and output layer. Each neuron of the output layer receives a signal from other neurons along connections with modifiable weights. But such two-layer feed forward networks can compute only linearly separable functions [131]. However, it has also been shown that a feedforward network with more than one layer of adaptive weights can compute very complex functions [132]. Fig.5.1 shows the schematic diagram of a multilayer feedforward network. The neurons in the network can be divided into three layers: input layer, hidden layer and output layer.

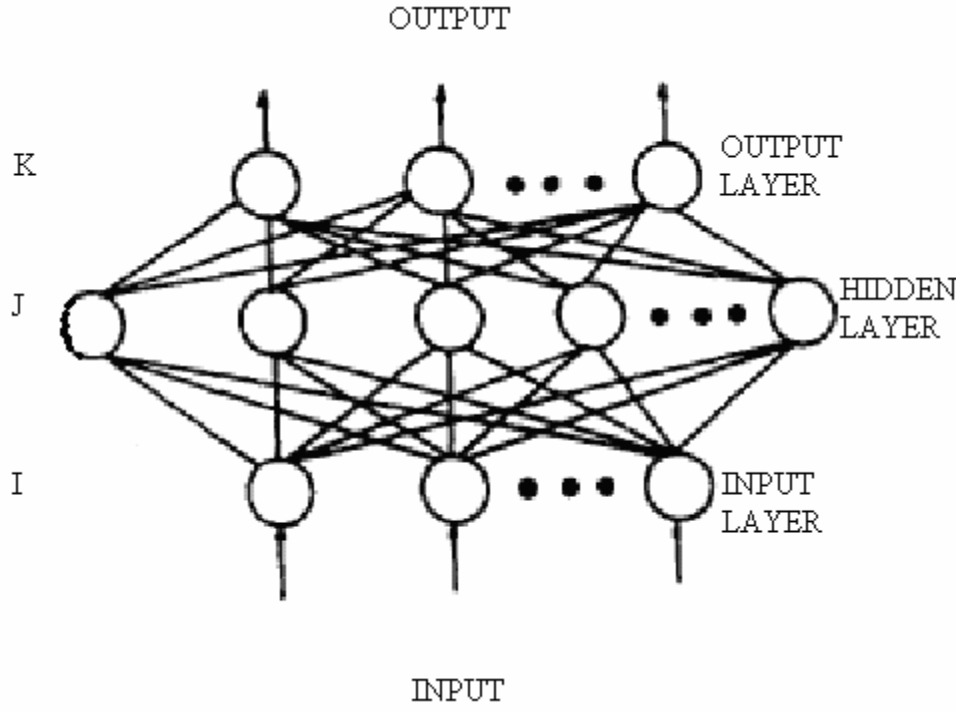

Fig. 5.1. A schematic multilayer feedforward network.

It is important to note that in feedforward networks signals can only propagate from the input layer to the output layer via one or more hidden layers. Hidden layer is

composed of neurons, called the hidden processing units. Both input and hidden layers have an additional node called bias. Processing proceeds from the input neurons to the output neurons via the hidden neurons. Each of them in the network is closely linked with those neurons to which it is connected, and the degree of influence is dictated by a quantity called connection weight being adjusted during training. It should also be noted that only the nodes in the hidden layer and the output layer, which use activation function, are called ordinary neurons. Since the nodes in the input layer simply pass on the signals from the external source to the hidden layer, they are often not regarded as ordinary neurons [133].

The neural network can identify input pattern vectors once the connection weights are adjusted by means of a learning process. The BPA [79], which is a generalization of the Widrow-Hoff error correction rule [134], is the most popular method in training the neural network and is employed here. This learning algorithm is presented below in brief.

For each neuron in the input layer, the neuron outputs are given by

$$o_i = n_i \qquad (5.1)$$

where n_i is the input of neuron i, and o_i the output of neuron i. Again for each neuron in the output layer, the neuron inputs are given by

$$n_k = \sum_{j=1}^{N_j} w_{kj} o_j \quad k = 1, 2\ldots\ldots N_k \qquad (5.2)$$

where w_{kj}, is the connection weight between neuron j and neuron k, and N_j, N_k the number of neurons in the hidden layer and output layer, respectively. The neuron outputs are given by

$$o_k = \frac{1}{1+\exp[-(n_k+\theta_k)]} = f_k(n_k, \theta_k) \qquad (5.3)$$

where θ_k is the threshold of neuron k, and the activation function f_k is a sigmoid function. For the neurons in the hidden layer, the inputs and the outputs are given by relationships similar to those given in equation 5.2 and equation 5.3, respectively.

The connection weights of the feedforward network are derived from the input-output patterns in the training set by the application of generalized delta rule [79]. The algorithm is based on minimization of the error function on each pattern 'p' by the use of steepest descent method [79]. The sum of squared errors 'E_p' that is the error function for each pattern is given by

$$E_p = \frac{1}{2}\sum_{k=1}^{N_k}(t_{pk} - o_{pk})^2 \qquad (5.4)$$

where t_{pk} is the target output for output neuron k, and O_{pk} the calculated output for output neuron k. The overall measure of the error for all the input-output patterns is given by

$$E = \sum_{p=1}^{N_p} E_p \qquad (5.5)$$

where N_p is the number of input-output patterns in the training set. When an input pattern p with the target output vector t_p is presented, the connection weights are updated by using the following equations.

$$\Delta w_{kj}(p) = \eta \delta_{pk} o_{pj} + \alpha \Delta w_{kj}(p-1) \qquad (5.6)$$

$$\delta_{pk} = (t_{pk} - o_{pk}) o_{pk}(1 - o_{pk}) \qquad (5.7)$$

where η is the learning rate, and α the momentum constant.

Again, the connection weights between input layer neuron i hidden layer neuron j can be updated by using the following equations

$$\Delta w_{ji}(p) = \eta \delta_{pj} o_{pj} + \alpha \Delta w_{ji}(p-1) \qquad (5.8)$$

$$\delta_{pj} = o_{pj}(1 - o_{pj}) \sum_{k=1}^{N_k} \delta_{pk} w_{kj} \qquad (5.9)$$

It is important to note that the threshold θ of each neuron is learned in the way same as that for the other weights. The threshold of a neuron is regarded as a modifiable connection weight between that neuron and a fictitious neuron in the previous layer.

It has been shown that a feedforward network with more than one layer of adaptive weights can compute very complex functions [132]. In MFNs one of the most important issues is the selection of number of hidden layers. It is shown by Rumelhart *et.al.* [135], that for a MFN with sigmoidal functions, two hidden layers are sufficient to

compute an arbitrary output even for a complex problem. The choice of optimal number of hidden neurons is perhaps the most interesting and challenging aspect in designing MFNs. One approach to this problem is presented by Hecht-Nielsen [136], which is the basis for the present work. He uses neural network interpretation of Kolmogorov's theorem to arrive at the upper bound on the number of hidden neurons for a single hidden layer network as $2(N_i + l)$, where N_i is the number of input neurons. Choice of the learning rate parameter and the momentum constant has a very significant effect on speed of the network. A large value of learning rate parameter results in faster convergence but often leads to oscillation, whereas, a small value, stabilizes the process but results in slower convergence and increases the susceptibility of getting entrapped in a local minimum. Similarly, a decrease in momentum, when connection weights are updated in the correct directions, will improve convergence. On the other hand, if the update direction is wrong, the value should be increased.

Scaling of the input-output data has a significant influence on the convergence property and also on the accuracy of the learning process. It is obvious from the sigmoid activation function given in equation 5.3 that the range of the output of the network must be within 0 to 1. Moreover, the input variables should be kept small in order to avoid saturation caused by the sigmoid function. Thus, the input-output data must be normalized before the initiation of the training of the neural network. Some of the different ways of normalization of input output data has been described below.

Normalization scheme 1

In this scheme of normalization, the maximum values of the input and output vector components are determined as follows:

$$n_{i,\max} = \max(n_i(p)) \;\; p=1,\ldots.N_p \quad i = \text{i},\ldots..N_i \qquad (5.10)$$

where N_p is the number of patterns in the training set and N_i is the number of neurons in the input layer. Again,

$$o_{k,\max} = \max(o_k(p)) \;\; \text{p} = \text{i},\ldots\ldots N_p, \quad \text{k} = 1,\ldots..N_k \qquad (5.11)$$

where, N_k is the number of neurons in the output layer. Normalized by these maximum values, the input and output variables are given as follows.

$$n_{i,nor}(p) = \frac{n_i(p)}{n_{i,\max}} \quad \text{p = 1,.....}N_p,\ \text{i = 1,.....}N_i \qquad (5.12)$$

and

$$o_{k,nor}(p) = \frac{o_k(p)}{o_{k,\max}} \quad \text{p = 1,.....}N_p,\ \text{i = 1,.....}N_k \qquad (5.13)$$

After normalization, the input and output variable lay in the range of 0 to 1 [137].

Normalization scheme 2

In this scheme, the output variables are normalized by using Equations (5.11) and (5.13) to get a range within 0 to 1. But the input variables are normalized as follows.

$$n_{i,nor}(p) = \frac{n_i(p) - n_{i,av}}{\sigma_i} \qquad p = 1,.....Np, \qquad \text{i =1,.....}Ni \qquad (5.14)$$

where $n_{i,av}$ and σ_i are the average value and the standard deviation of the I-th component of the input vector respectively. In this scheme after normalization, the input variable range is ($-K_1$ to K_2), where K_1 and K_2 are real positive numbers. These input variables can then be easily made to fall in the range -1 to 1 by dividing these variables by the larger of the two numbers, i.e. K_1 or K_2 [138].

Normalization scheme 3

The input data and the output data were normalized to give values between around 0.05 and 0.95 through the following equations:

$$X'_i = \frac{(X_i - \overline{X_i})}{\sigma} \qquad (5.15)$$

where $\overline{X_i} = \sum_{i=1}^{p} X_i$, $\sigma = \sqrt{\frac{(X_i - \overline{X_i})^2}{p}}$, X_i is the original input data, and p is the number of training samples.

$$y_i = 0.05 + 0.9 \times \frac{y_i - y_{\min}}{y_{\max} - y_{\min}} \qquad (5.16)$$

where *Yi* is the original output data. *Ymin* and *Ymax* are the minimum value and maximum one in the original output data, respectively [139].

5.3 ANN Modeling

The network employed in this modeling consisting of three layers, that is, input layer, hidden layer and output layer. The input and output layers consist of some neurons where the input information is presented to the network and the response of the network is registered, respectively. Key steps for calculations in the network have been explained in equation 5.1 to equation 5.9. The iteration continues from equation 5.1 to 5.9 with different sets of input patterns, until the overall error between calculated and target outputs are approaching to the pre-set error criteria. The algorithm, as mentioned above, was realized in MATLAB platform of Microsoft Windows XP.

The experimental data for Lanthanum doped $BaTi_{0.6}Zr_{0.4}O_3$ composition with x = 0.005, 0.01, 0.02, 0.05 and 0.1 in $Ba_{(1-x)}La_xTi_{0.6[1-(5x/12)]}Zr_{0.4}O_3$ were obtained using procedure discussed in Chapter 3. As discussed, the capacitance and loss tan δ of the samples were measured at different frequencies and composition and the values were used to train the network.

5.4 Results and discussions

The architecture of the network used in this modeling is shown in Fig. 5.2. As may be seen, the network consists of four input neurons and two output neurons, as there are four inputs and number of outputs is two. The inputs were; atom % Barium, Lanthanum, Titanium in a unit crystal of composition $Ba_{(1-x)}La_xTi_{0.6[1-(5x/12)]}Zr_{0.4}O_3$ with different values of x and frequency. The outputs are relative permittivity and tan δ.

In the work, the procedure as stated in reference [139], was adopted for normalization. The inputs were normalized using mean and standard deviation of the input training samples (equation 5.15). Similarly, the outputs were normalized using equation 5.16 to lie in between 0.05 and 0.95. The number of training samples was 350.

Determination of appropriate numbers of hidden neurons is an important factor as it determines the network's performance. From trials, using different numbers of hidden neurons from 7 to 11, the minimum value of root mean square error were obtained for 10

numbers of hidden neurons. The learning rate parameter and the momentum constant were optimized to 0.9 and 0.3, respectively to get best performance. The initial connection weights were set to be random. The training continued in sequential mode up to 1000 iterations.

The error values as a function of iteration, during training has been shown in Fig. 5.3. It converges slowly till 1000 iteration where root mean square error was below 0.001.

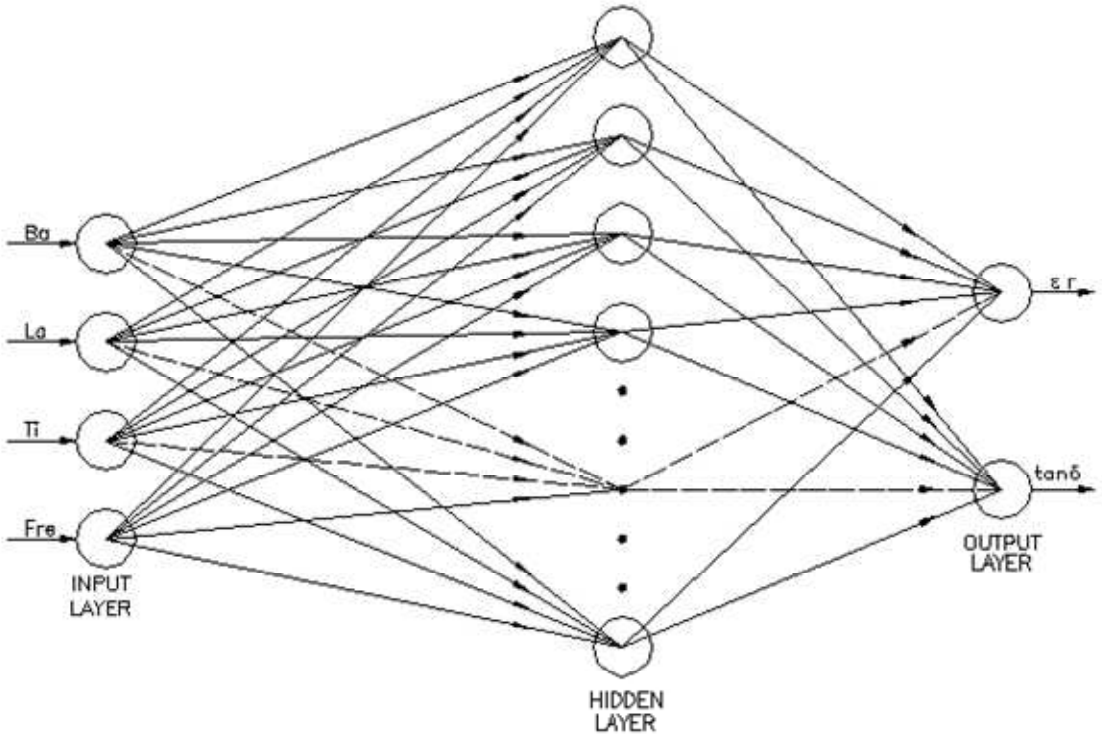

Fig. 5.2. Feedforward network used in modeling.

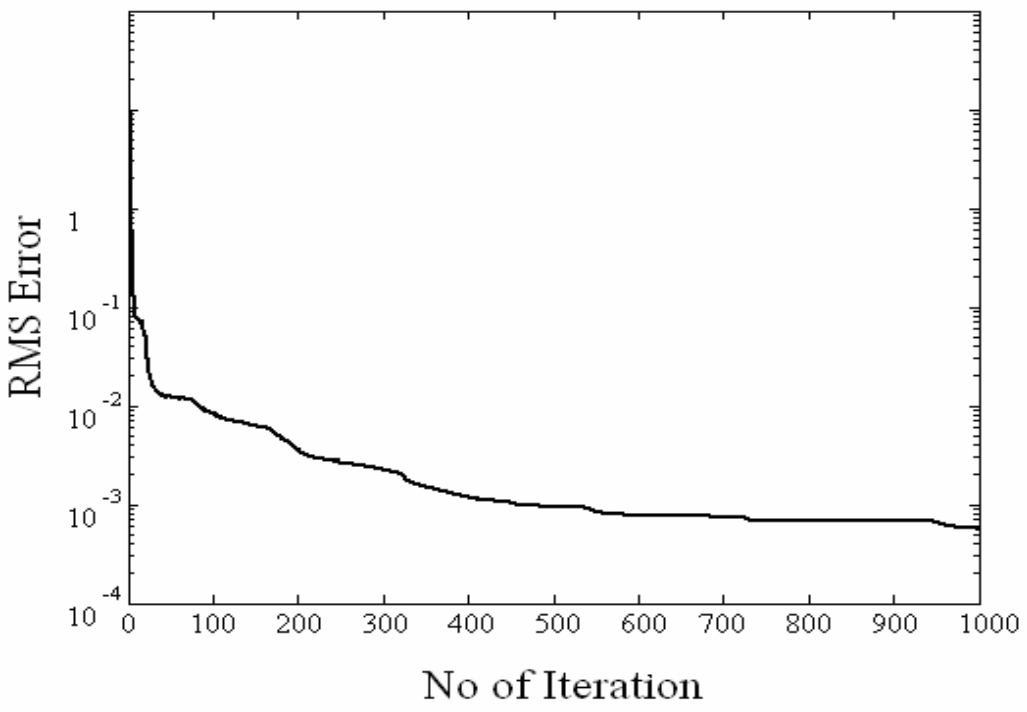

Fig.5.3. RMS error as a function of number of iteration

Finally, after the network was trained, the relative permittivity and loss tangent values are estimated for, initially with the same sets of data which were used for training and later with test data sets (these data sets were not included during training process) simply by passing the input data in the forward path of the network and using updated weights of the network.

Comparison of estimated output with the measured value of relative permittivity and loss tangent: The modeled outputs along with experimental values were plotted against different frequencies, shown in Fig. 5.4. The enlarged view of 0.5 at.% doped $BaTi_{0.6}Zr_{0.4}O_3$ with estimated value of ANN has been shown in Fig.5.5. It may be seen that the estimated values, shown by dotted lines, closely follows the experimental values. Further, it may be seen that relative permittivity decreases with increasing Lanthanum percentage.

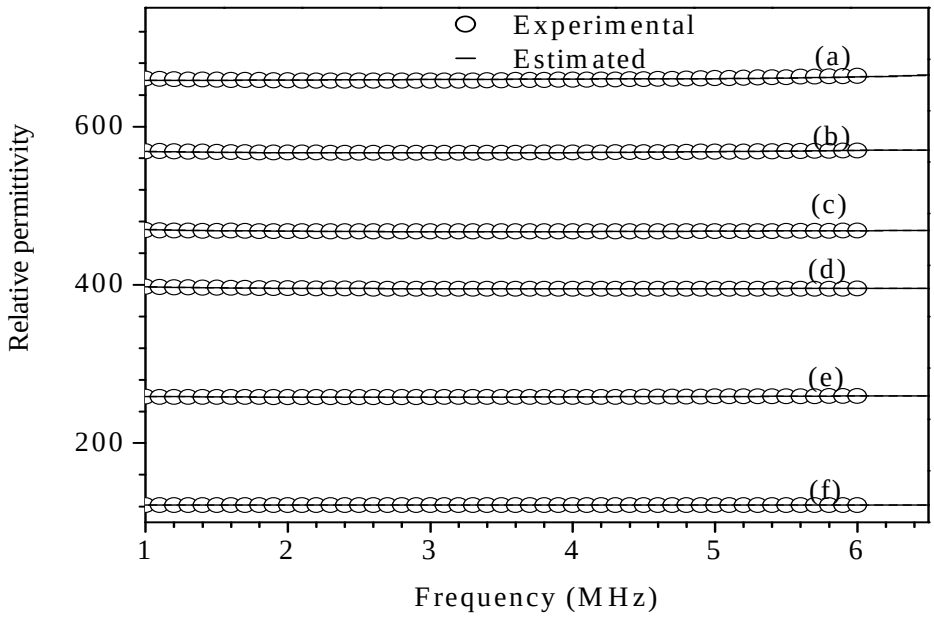

Fig.5.4. Relative permittivity as a function of frequency for $Ba_{(1-x)}La_xTi_{0.6[1-(5x/12)]}Zr_{0.4}O_3$ with x value (a) 0, (b) 0.005, (c) 0.01, (d) 0.02, (e) 0.05 and (f) 0.1.

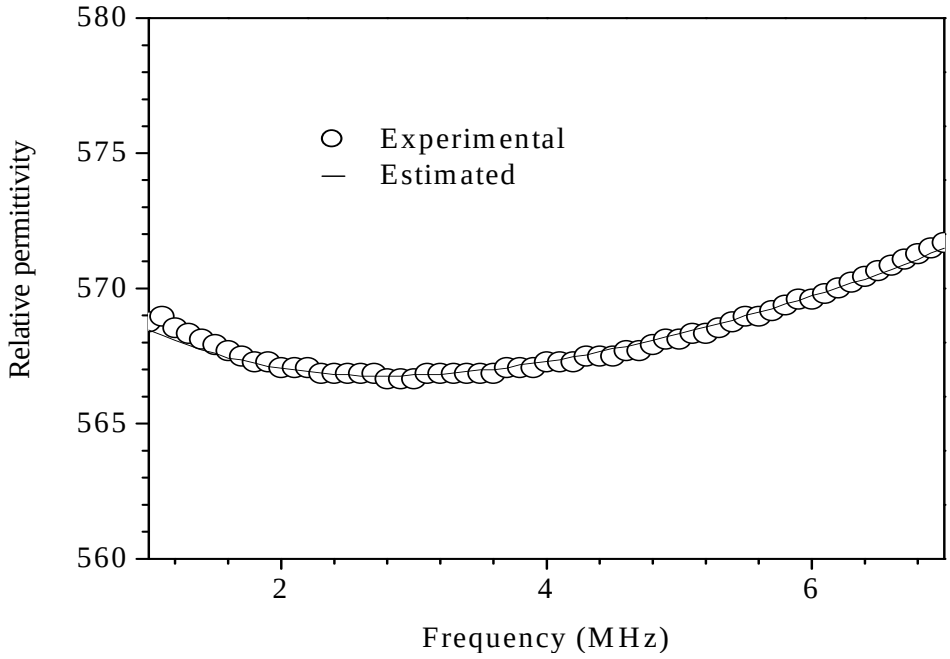

Fig.5.5. Enlarged view of relative permittivity as a function of frequency for $Ba_{(1-x)}La_xTi_{0.6[1-(5x/12)]}Zr_{0.4}O_3$ with x value 0.005.

Fig.5.6 shows the variation of tan δ as a function of frequency for various Lanthanum percentages. As may be seen, loss tangent values decreases with increase in Lanthanum percentage. Again, the neural output is closely following the experimental output.

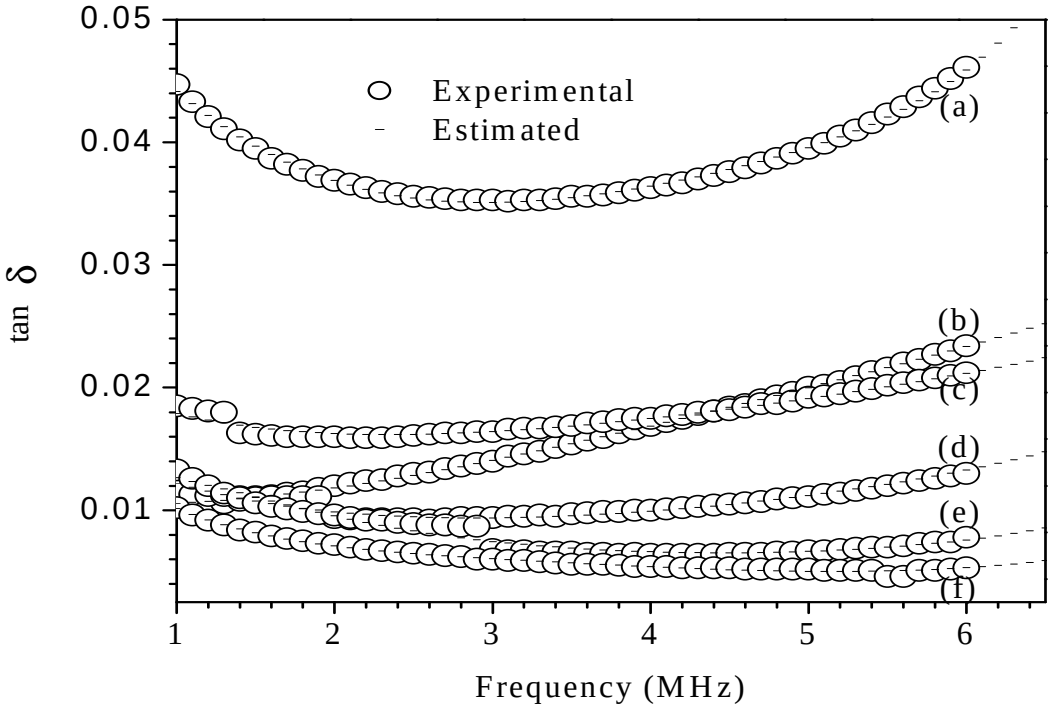

Fig.5.6. tan δ as a function of frequency for $Ba_{(1-x)}La_xTi_{0.6[1-(5x/12)]}Zr_{0.4}O_3$ with x value (a) 0, (b) 0.005, (c) 0.01, (d) 0.02, (e) 0.05, (f) 0.1.

Fig. 5.7 shows the estimated outputs of relative permittivity as a function of frequency for different Lanthanum %. Different Lanthanum doped (0.5%, 1%, 2%, 5% and 10%) data were used to train the network. After the network was trained, estimations were done for 3%, 4%, 6%, 7% and 8% of La (these data sets were not included during training process). The estimated values of relative permittivity for the test data sets follow the same pattern and decreases as the Lanthanum percentage increases with a flat profile with frequencies.

Comparison of experimental and estimated relative permittivity for $Ba_{(1-x)}La_xTi_{0.6[1-(5x/12)]}Zr_{0.4}O_3$ with different x values, at 5MHz has been shown in Fig.5.8. The results are in good agreement with our experimental results. When correlation was made for experimental and estimated values, a straight line was found.

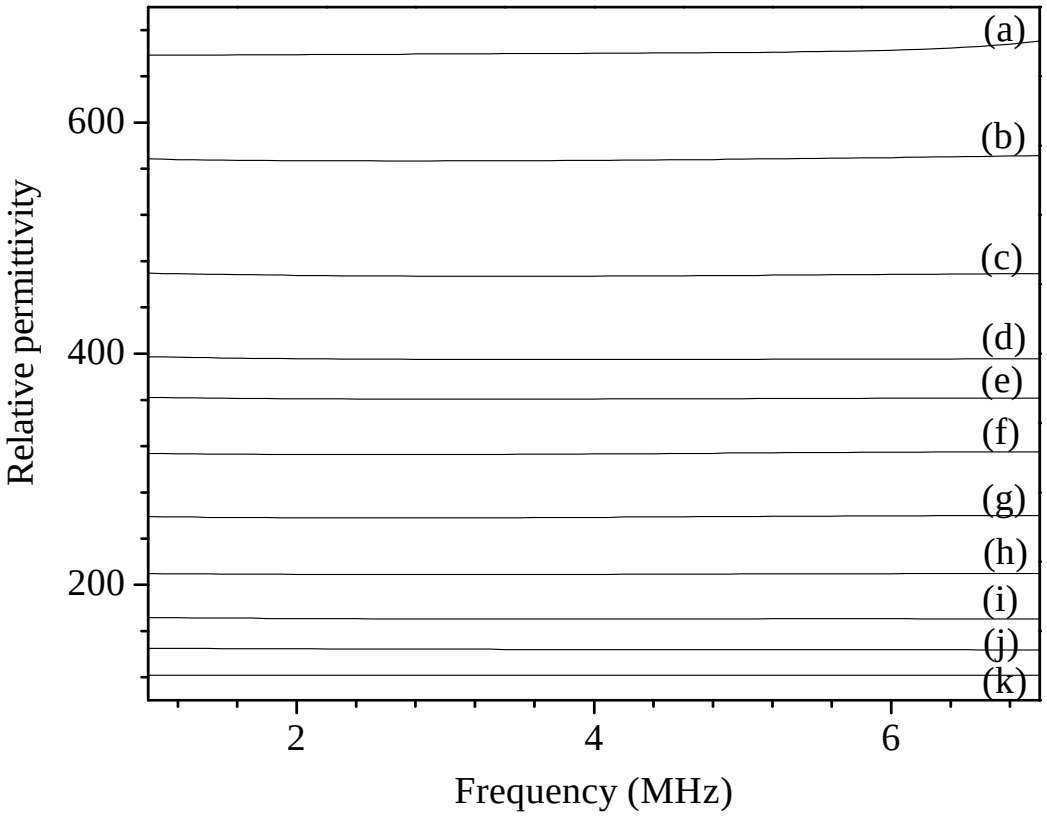

Fig.5.7. Estimated values of relative permittivity as a function of frequency for $Ba_{(1-x)}La_xTi_{0.6[1-(5x/12)]}Zr_{0.4}O_3$ with x value (a) 0, (b) 0.005, (c) 0.01, (d) 0.02, (e) 0.03, (f) 0.04, (g) 0.05, (h) 0.06, (i) 0.07, (j) 0.08 and (k) 0.1.

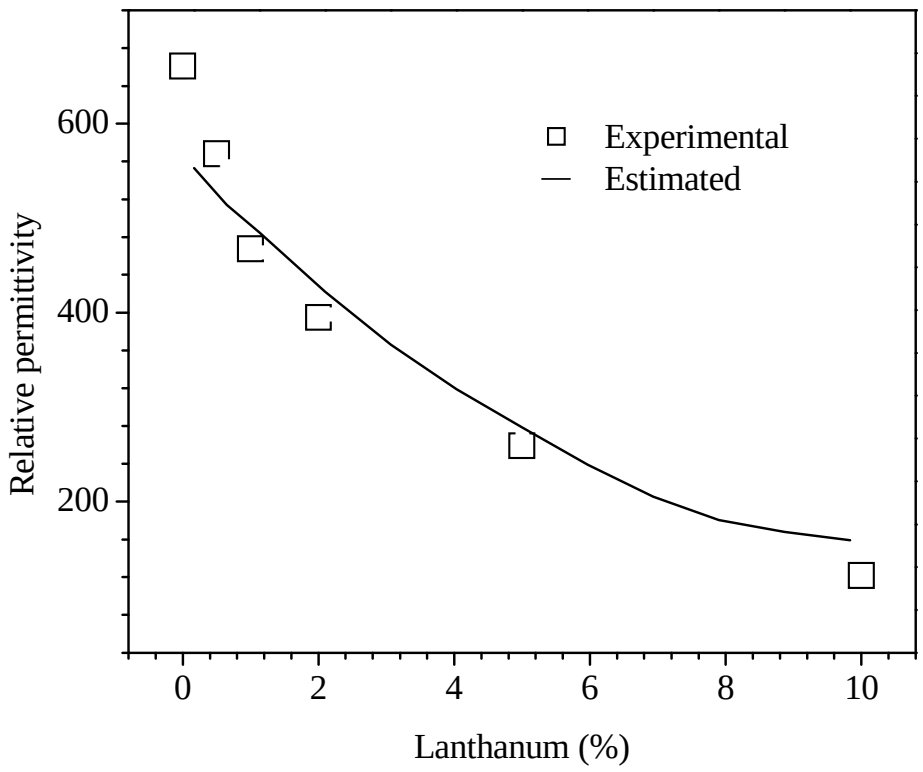

Fig.5.8. Comparison of experimental and estimated relative permittivity at 5MHz for $Ba_{(1-x)}La_xTi_{0.6[1-(5x/12)]}Zr_{0.4}O_3$.

5.5 Conclusions

Artificial Neural Network is a very useful tool in dealing with problems in formulation design of dielectric ceramics particularly where equation describing the function is unknown. The following conclusions can be drawn based on the discussion:

1. The combination of ANN parameters for best result in modeling is identified.

2. The modeled values closely follow the experimental values suggesting the effectiveness of the proposed modeling and indicate that the ANN with BPA can be used for estimation of electrical properties of undoped and lanthanum doped $BaTi_{0.6}Zr_{0.4}O_3$.

Thus, ANN based modeling proved to be a very useful tool in dealing with problems encountered in dielectric ceramics.

CHAPTER 6

MAJOR CONCLUSIONS AND FUTURE WORK

6.1 Introduction

The present work deals with the synthesis and electrical characterisation of lanthanum doped barium titanate zirconate. Detailed discussion and conclusions have been given at the end of each chapter. Therefore, the concluding chapter is devoted to the summarization of the main contributions of the work and arriving at general conclusions.

6.2 Summary

The present work focused on modified solid state synthesis of $BaTi_{0.6}Zr_{0.4}O_3$ and lanthanum substituted $BaTi_{0.6}Zr_{0.4}O_3$. The influence of lanthanum on the dielectric properties, tan δ and dc resistivity of the ceramics were examined. The effect of porosity on relative permittivity and tan δ was studied. The relaxor behavior of lanthanum doped samples was analysed. At the end, the electrical properties of undoped and lanthanum doped $BaTi_{0.6}Zr_{0.4}O_3$ was modeled by artificial neural network using back propagation algorithm.

6.3 Conclusions

Before the thesis draws to a close, the general conclusions that emerge out from the work are highlighted. These conclusions are arrived at based on the effect of lanthanum doping on the behaviour of the material concerned. This finally leads to an outline of the future directions for research and development efforts in this area.

The main conclusions drawn are:

- $BaTi_{0.6}Zr_{0.4}O_3$ perovskites has been synthesized from the mixture of barium oxalate hydrate, titanium dioxide and zirconium oxy-hydroxide. Studies on phase formation mechanism show that, the BT and BZ phases are formed separately in the system. Then, $BaTi_{0.6}Zr_{0.4}O_3$ was formed by the reaction between BT and BZ. BT formation activation energy, 134 KJ mol^{-1}, was lower than BZ formation energy, 167.5 KJ mol^{-1}. That may be due to the difference in their ionic radius. BT–BZ solid solution was formed mainly by the diffusion of titanium from BT

into the BZ lattice, where the latter phase acts as diminishing core. Activation energy for BTZ solid solution formation was 503.6 KJ mol^{-1}, which may be due to the diffusion of Ba and/or O ions through solid solution interface. The mean activation energy for sintering of compact powder was evaluated to be 550 KJ mol^{-1}.

- Lanthanum doped $BaTi_{0.6}Zr_{0.4}O_3$ compositions $Ba_{1-x}La_xTi_{0.6[1-(5x/12)]}Zr_{0.4}O_3$, $Ba_{1-x}La_x(Ti_{0.6}Zr_{0.4[1-(5x/8)]})O_3$ and $Ba_{1-x}La_x(Ti_{0.6[1-x/4]}Zr_{0.4[1-x/4]})O_3$ with x = 0.005, 0.01, 0.02, 0.05 and 0.1 were synthesized. Perovskite phases were observed for all compositions without existence of any secondary phases. A gradual shift of diffraction peak to the higher angle with increasing lanthanum percentage reveals the contraction of perovskite lattice. Sinterability of the dielectrics decreases with increasing lanthanum substitution.

- It is found that dielectric permittivity (ε_r) and tan δ decreases with increase in lanthanum percentage. Room temperature permittivity of lanthanum doped dielectrics was highly stable against change in frequency.

- It is noted that dielectric permittivity (ε_r) decreases and tan δ increases with increase in porosity.

- The La substitution in $BaTiZrO_3$ shifts the transition temperature T_m to a lower temperature region with increasing substitution. A γ value of 1.89 implies relaxor-like behavior with a strong frequency dispersion of the T_m. The ceramics obey the empirical Vogel–Fulcher relation, which again confirms the relaxor behavior.

- Resitivity is slightly decreased at 0.5 atom % lanthanum substitution and then gradually increases with increasing substitutions. At low electric field the current density displays nearly ohmic behaviour.

- The combination of ANN parameters for best result in modeling was identified. The modeled values closely follow the experimental values suggesting the effectiveness of the proposed modeling and indicate that the ANN with BPA can be used for estimation of electrical properties of the dielectrics. Thus, ANN based modeling proved to be a very useful tool in dealing with problems encountered in dielectric ceramics.

6.4 Future work

Based on the observations in this thesis, the work may be extended in future as

1. Study of dielectrics and relaxor properties of lanthanum substituted BTZ at higher concentration of substitution ($0.10<x<0.35$).
2. Studies on barium vacancy mechanism with composition $(Ba_{1-x}La_{2x/3}\square_{x/3})(Ti_{1-y}Zr_y)O_3$.
2. Tunability characteristics of different lanthanum substituted dielectrics.

REFERENCES

[1] J. Valasek, *Phys. Rev*. 17, 475 (1921).

[2] J. F. Nye, Physical Properties of Crystals, *Oxford University Press*, Oxford 1957.

[3] D. D. Viehland, *Ph.D. Thesis*, The Pennsylvania State University, University Park, PA (1991).

[4] Y. Xu, Ferroelectric Materials and Their Applications, *North-Holland Elsevier Sci.Publ.*, Amsterdam 1991.

[5] L. E. Cross, *Ferroelectrics*, 151, 305 (1994).

[6] B. Wul and I. M. Goldman, *C. R. Acad. Sci. U. R. S. S.* 46, 177 (1945).

[7] M. E. Lines and A. M. Glass, *Principles and Applications of Ferroelectrics and Related Materials*, Clarendon Press, Oxford 1977.

[8] A.Safari, R. K. Panda, and V. F. Janas, *Key Eng. Mater*. 122-124, 35 (1996).

[9] B. Jaffe, W. R. Cook and H. Jaffe, *piezoelectric Ceramics*, London and New York 1971.

[10] D. Amjanovic, *Rep. Prog. Phys.* 61, 1267 (1998).

[11] W. J. Merz, *Phys. Rev.* 95, 690 (1954).

[12] V. A. Bokov and I. E. Mylnikova, *Sov. Phys.-Sol. State* 3, 613 (1961).

[13] T. R. Shrout and A. Halliyal, *Am. Ceram. Soc. Bull.*, 66, 704 (1987).

[14] L. E. Cross, *Ferroelectrics*, 76, 241 (1987).

[15] W. Kleemann and A. Clossner, *Ferroelectrics*, 150, 35 (1993).

[16] T. Mitsui and S. Nomura, *Ferroelectrics and Related Substances*, New Series, Vol. 16. *Springer-Verlag*, Berlin (1981).

[17] J. Chen, H. Chan and M. P. Harmer, *J. Amer. Ceram. Sot. 72,593 (1989).*

[18] W. K. Choo and H.J. Kim, *J. Phys. Condens. Matter* 4,2309 (1992).

[19] I. W. Chen, P. Li and Y. Wang, *J. Phys. Chem Solids* Vol 57. No. 10, pp. 1525-1536, 1996.

[20] A. Dixit, S.B. Majumder and R.S. katiyar, *Appl. Phys. Lett*. 82 (16), PP 2679-81, 2003.

[21] S.C. Abrahams, S.K. Kurtz and P.B. Jamieson, *Phys. Rev.* 172 (1968) 551.

[22] R.D. Shannon, *Acta Cryst. A* 32 (1976) 751.

[23] J. Ravez and A. Simon, *Eur. J. Solid State Inorg. Chem*. 34 (1997) 1199.

[24] P. Sciau, G. Calvarin and J. Ravez, *Solid State Commun*. 113 (2000) 77– 82.
[25] P.S. Dobal, A. Dixit, R.S. Katiyar, Z. Yu, R. Guo and A. Bhalla, *J. Appl. Phys*. 89, 12, (2001) 8085.
[26] X.G. Tang, K.-H. Chew and H.L.W. Chan, *Acta Materialia* 52 (2004) 5177–5183.
[27] T.B.Wu, C.M.Wu and M.L. Chen, *Appl. Phys. letter* 69 (18) (1996) 1259-1261.
[28] C. Hofera, R. Meyera, U. Bottgera and R. Wasera, *J. Eur. Ceram. Soc* 24 (2004) 1473–1477.
[29] F.D. Morrison, A.M. Coats, D.C. Sinclair and A.R. West, *J Electroceramics* [6] (2001) 219.
[30] K.Aliouane, A.Guehria-Laidoudi, A.Simon and J.Ravez, *SolidState Sciences* [7] (2005) 1324–1332.
[31] X. Chou, J. Zhai and Xi Yao, *Materials Chemistry and Physics* 109 (2008) 125–130.
[32] F. Moura, A.Z. Simoes, B.D. Stojanovic, M.A. Zaghete, E. Longo and J.A. Varela, *Journal of Alloys and Compounds* 462 (2008) 129–134.
[33] N. Nanakorn, P. Jalupoom, N. Vaneesorn and A. Thanaboonsombut, *Ceramics International* 34 (2008) 779–782.
[34] V. Reymond, S. Payan, D. Michau, J. Manaud and M. Maglione, *Thin Solid Films* 467 (2004) 54– 58.
[35] A. Dixit, S.B. Majumder, A. Savvinov, R.S. Katiyar, R. Guo and A.S. Bhalla, *Materials Letters* 56 (2002) 933– 940.
[36] J. Zhai, C. Gao, X. Yao, Z. Xu and H. Chen, *Ceramics International* 34 (2008) 905–910.
[37] M. Veith, S. Mathur, N. Lecerf, V. Huch, T. Decker and H. Pech, *J Sol–Gel Sci Tech* 2000;15:145.
[38] X.G. Tang, Q.F. Zhou and J.X. Zhang, *J Appl Phys* 1999;86:5194.
[39] L.G.A. Marques, L.S. Cavalcante, A.Z. Simoes, F.M. Pontes, L.S. Santos-Junior, M.R.M.C. Santos, I.L.V. Rosa, J.A. Varela and E. Longo, *Mater. Chem. Phys*. 105 (2007) 293–297.
[40] S. Bhaskar Reddy, K. Prasad Rao and M.S. Ramachandra Rao, *Scrip. Materia.* 57 (2007) 591–594.
[41] B.W. Lee and S.B. Cho, *J. Euro. Ceram. Soc*. 25 (2005) 2009–2012.

[42] A.K. Tagantsev, V.O. Sherman, K.F. Astafiev, J. Venkatesh and N. J. Setter *Electroceram*. 2003;11:501.

[43] S. Hoffmann and R.W. Waser. *Integr. Ferroelectr.* 1997;17:141.

[44] D. Hennings, A. Schnell and G. Simon. *J. Am. Ceram. Soc.* 1982;65:539.

[45] Y. Zhi, A. Chen, R. Guo and A.S. Bhalla, *Appl Phys Lett* 2002;81:1285.

[46] J. Ravez, C. Broustera and A. Simon, *J Mater Chem* 1999;9:1609.

[47] Z. Yu, R. Guo and A.S. Bhalla, *Appl Phys Lett* 2000;77:1536.

[48] X.G. Tang, H.L.W. Chan and A.L. Ding, *Thin Solid Films* 2004;460:227.

[49] U. Weber, G. Greuel, U. Boettger, S. Weber, D. Hennings and R. Waser, *J. Am. Ceram. Soc.* 2001;84:759.

[50] T. Tsurumi, Y. Yamamoto, H. Kakemoto and S. Wada, *J Mater Res* 2002;17:755.

[51] S. Hoffmann and R. Waser. *J Euro. Ceram. Soc.* 1999;19:1339.

[52] R. Farhi, M.E. Marssi, A. Simon and J. Ravez, *Eur. Phys. J., B Cond. Matter Phys*. 9 (1999) 599.

[53] K.Y. Yiang, W. J. Yoo and A. Krishnamoorthy, *IEEE Trans. Electr. Devices*, vol. 52, no.10, october 2005.

[54] X. Gong, W. H. She, E.E. Hoppenjans, Z.N. Wing, R.G. Geyer, J.W. Halloran and W.J. Chappell, *IEEE Trans. Micro. Theo. Tech*, vol. 53, no. 11, (2005).

[55] A. Bognar, L. Kalocsai, G. Csepes, E. Nemeth and J. Schmidt, *Rapports de la CIGRE, Tome I*, edition (1990).

[56] H. Kishi, Y. Okino, M. Honda, Y. Iguchi, M. Imaeda, Y. Takahashi, H. Ohsato and T. Okuda, *Jpn. J. Appl. Phys*. 36 (1997) 5954–5957.

[57] J. Zupan and J. Gasteiger, "*Neural Networks for Chemists*" An Introduction, Weinheim, VCH, Germany, 1993.

[58] P. C. Bressloff and D. J. Weir, *GEC Journal of Research*, Vol. 8, No. 3, pp. 151-169, 1991.

[59] K. Fukishama, *Neural Networks*, Vol. 1, pp. 119- 130, 1988.

[60] T. Kohonen, *IEEE Computer Magazine*, pp. 11-22, March, 1988.

[61] K. J. Lang, A. H. Weibel and G. E. Hinton, *Neural Networks*, Vol. 3, pp. 23-43, 1990.

[62] R. P. Gorman and T. J. Sejnowsky, *Neural Networks*, Vol. 1, pp. 75-89, 1988.

[63] N. H. Farhai and B. Bai, *Neural Networks*, Vol. 2, pp. 117-125, 1989.

[64] G. A. Carpenter, *Neural Networks*, Vol. 2, pp. 243-257, 1989.

[65] H. Miyamoto, M. Kawoto, T. Setoyama and R. Suzuki, *Neural Networks*, Vol. 1, pp. 251-265, 1988.

[66] Y. Y.Hsu and C. C. Yang, *Proc. IEE, Pt. C*, Vol. 138, NO. 5, pp. 414-418, 1991.

[67] K. Y. Lee, Y. T. Cha and J. H. Park, *IEEE Trans. on PWRS*, Vol. 7, No. 1, pp. 124-132, 1992.

[68] K. L. Ho, Y. Y. Hsu and C. C. Yang, *IEEE Trans. on PWRS*, Vol. 7, No. 1, pp. 141-149, 1992.

[69] T. M. Peng, N. F. Hubele and G. G. Karady, *IEEE Trans. On PWRS*, Vol. 7, NO. 1, pp. 250-257, 1992.

[70] D. J. Sobajic and Y. H. Pao, *IEEE Trans. on PWRS*, Vol. 4, NO. 1, pp. 220-228, 1889.

[71] M. E. Aggoune, M. A. El-Sharkawi, D. C. Park, M. J. Damborg and R. J. Marks 11, *Proc. 1989 IEEE-PICA Conference*, pp. 252-258, Seatle, USA, 1989.

[72] N. I. Santoso and O. T. Tan, *IEEE Trans. on PWRD*, Vol. 5, NO. 1, pp. 266-272, 1990.

[73] E. H. P. Chan, *Proc. 1989 IEEE-PICA Conference*, pp. 246-251, Seatle, USA, 1989.

[74] H. Suzuki and T. Endoh, *IEEE Trans. Electr. Insul.*, Vol. 27, No. 3, pp. 543-549, 1992. [75] N. Hozumi, T. Okamoto and T. Imajo, *IEEE Trans. Electr. Insul.*, Vol. 27, No. 3, pp. 550-556, 1992.

[76] S. Haykin, Neural Networks, *Maxwell Macmillan*, Ont., Canada, 1994.

[77] J.C. Patra, R.N. Pal, R. Baliarsingh and G. Panda, *IEEE Trans. Syst. Man Cybernet. Part B: Cybernet.* 29 (1999) 262 –270.

[78] J.C. Patra, R.N. Pal, B.N. Chatterji and G. Panda, *IEEE Trans. Syst. Man Cybernet. Part B: Cybernet.* 29 (1999) 254–261.

[79] D. E. Rumelhart, G. E. Hinton and R. J. Williams, *Parallel Distributed Processing*, Vol. 1, pp. 318-362, MIT Press, MA, 1986.

[80] R. Hechi-Nielsen, *Proceedings of IJCNN*, 1989, pp. 593–603.

[81] J. Bera and S.K. Rout, *Materials Letters* 59 (2005) 135–138.

[82] D.F.K. Hennings, B. Schreinemacher and H. Schreinemacher, *J. Eur. Ceram. Soc.* 13 (1994) 81– 88.

[83] S. Gopalan and A.V. Virkir, *J. Am. Ceram.* Soc. 82 (10) (1999) 2887.

[84] M. Veith, S. Mathur, N. Lecerf, V. Huch, T. Decker, H. P. Beck, W. Eiser and R. Haberkorn, *J. Sol–Gel Sci. Technol.* 17 (2000) 145 - 158.

[85] X.G. Tang, J. Wang, X.X. Wang and H.L.W. Chan, *Solid State Commun.* 131 (2004) 163–168.

[86] P.K. Roy and J. Bera, *Materials Research Bulletin* 40 (2005) 599–604.

[87] J. Bera and D. Sarkar, *J. Electroceram.* 11 (2003) 131-137.

[88] Terry A Ring, *Fundamentals of Ceramic Powder Processing and Synthesis,* Academic Press, Inc., California, 1996, pp. 191.

[89] S. Kumar and G.L. Messing, *J. Am. Ceram. Soc.* 77 (11) (1994) 2940.

[90] J. Bera, *J. Mater. Scie. Lett.* 12 (1993) 27-29.

[91] R. Pantou, C. Dubourdieu, F. Weiss, J. Kreisel, G. Kobernik and W. Haessler, *J. Mater. Sci. in Semi. Proc.* 5 (2002) 237-241.

[92] J. Jean and C.H. Lee, *J. Am. Ceram. Soc.* 82 [2] 343-350 (1999).

[93] S. Yamanaka, M. Fujikane, T. Hamaguchi, H. Muta, T. Oyama, T. Matsuda, S. Kobayashi and K. Kurosaki, *J. Alloy. Comp.* 359 (2003), 109-113.

[94] M.T. Buscaglia, M. Viviani, V. Buscaglia, C. Bottino and P. Nanni, *J. Am. Ceram. Soc*. 85[6] 1569-75, 2002.

[95] K. Takada, E. Chang and D.M. Smith, *Adv Ceram,* 19,147-52, 1987.

[96] L.A. Xue, Y. Chen and R.J. Brook, *Mater. Sci. Eng B1*, 193-201, 1988.

[97] T. Murakami, T. Miyashita, M. Nakahara and E. Sekine, *J. Am. Ceram. Soc*, 56, [6], 294-97 1973.

[98] F.D. Morrison, D.C. Sinclair and A.R. West, *International Journal of Inorganic Materials* 3 (2001) 1205–1210.

[99] J. Gielniak, T. Kalicki, H. Mogcicka-Grzesiak, J. Bielecki and J. Dziadkowiec, *IEEE international conference on High Voltage Engineering*, Symposium, 22-27 August 1999.

[100] F. Bitam-Megherbi, S. Osmani and M. Megherbi, *IEEE Internotional Conference on Solid Dielectrics*, France, July 5-9, 2004.

[101] A. Templeton, X. Wang, S. J. Penn, S. J. Webb, L. F. Cohen, and N. M. Alford, *J. Am. Cera. Soc*, vol. 83, no. 1, pp. 95–100, Jan. 2000.

[102] J. Ravez and A. Simon, *Eur. Phys. J. AP* 11 (2000) 90.

[103] A. Kerfah, K. Taibi, A. Guehria-Laidoudi, A. Simon and J. Ravez, *Mat.Lett.* 42 (2000) 189–193.

[104] N. Kurata and M. Kuabara, *J. Am. Ceram. Soc.* 76 [6] 1605-608, 1993.

[105] F.D. Morrison, D.C. Sinclair, J.M.S Skakle, and A.R.West, *J, Amer. Ceram. Soc.* 81 [7] 1957-1960 (1998).

[106] D. Viehland, M. Wuttig and L.E. Cross, *Ferroelectrics* 1991;120:71.

[107] H.T. Martirena and J.C. Burfoot, *Ferroelectrics* 1974;7:151.

[108] K. Uchino and S. Nomura, *Ferroelectr Lett Sect* 1982;44:55.

[109] H.Vogel, *Z Phys* 1921;22:645.

[110] B.E. Vugmeister and M.D. Glinichuk, *Rev Mod Phys* 1990;62:993.

[111] Z.G. Ye, *Key Engrg. Mater.* 155–156 (1998) 81–122.

[112] T. Ikeda, *J. Phys. Soc. Jpn.* 13 (1958) 335.

[113] J. Ravez, M. Pouchard and P. Hagenmuller, *Eur. J. Solid State Inorg.Chem.* 28 (1991) 1107.

[114] J. Ravez and A. Simon, *Solid State Sci*. 2 (2000) 525–529.

[115] J. Daniels, K.H. Hardtl, D. Hennings and R. Wernicke, *Philips Res Rep* 1976;31:487.

[116] N-H Chan and D.M Smyth, *J. Am. Ceram. Soc.* 1984; 67:285.

[117] J. Nowotny and M. Rekas, *Ceram. Intern.* 1994;20:265.

[118] P.W. Haayman, R.W. Dam and H.A. Klasens, *German Pat.* No. 929350. June 23, 1955.

[119] F.D. Morrison, *PhD Thesis*, University of Aberdeen, 1999.

[120] F.D. Morrison, D.C. Sinclair and A.R. West, *J. Am. Ceram. Soc.* 2001;84 [3]:531-538.

[121] T. Negas, G. Yeager, S. Bell, N. Coats and I. Minis, *Am Ceram Soc Bull* 1993;72:80.

[122] O. Saburi, *J. Phy. Soc. Jpn* 14[9] 1159-1174 (1959).

[123] A.B. Alles, V.R.W. Amarakoon and V.L.Bardick, *J. Am. Ceram. Soc.* 72[1] 148-151 (1989).

[124] H.A. Sauer and J.R. Fisher, *J. Am. Ceram. Soc.* 43 [6] 297-301 (1960).

[125] N. J. Tennery and R.L. Cook, *J. Am. Ceram. Soc.* 44 [4]187-93 (1961).

[126] R. Wernicke, *Phys. Status. Solid A*, 47, 139-44, (1978).

[127] G.H. Jonker, *Solid State Electronics* 7. 895-903, 1964.

[128] H.M. Chan, M.P. Hazmer and D.M. Smyth, *J. Am. Ceram. Soc.* 69 [6] 507-10 (1986).

[129] S.B. Desu, *J. Am. Ceram. Soc.* 73[11] 3407-15 (1990).

[130] H. Kishi, N. Kohzu, Y. Mizuno, Y. Iguchi, J. Sugino, H. Ohsato and T. Okuda, *Jpn. J. Appl. Phys*, 38, PP 5452-5456, 1999.

[131] M. Minsky and S. Pappert, *Perceptrons: An Introduction to Computational Geometry*, Cambridge, MA: MIT Press, expanded ed. 1988.

[132] S. Amari, *Proc. IEEE*, Vol. 78, No. 9, pp. 1443-1462, Sept, 1990.

[133] R. P. Lipmann, *IEEE ASSP Magazine*, pp. 4-22, April, 1987.

[134] B. Widrow and M. E. Hoff, *Parallel Distributed Processing*, Vol. 1,pp. 123-134, MIT Press, MA, 1986.

[135] D. E. Rumelhart and J. L. Mcclelland, Eds., *Parallel Distributed Processing Exploration in the microstructure of cognition, Vol. 1, MIT press, 1986.*

[136] R. Hecht-Nielsen, *Neurocomputing, Addison*-Wesley publishing Company, Inc., USA, 1990.

[137] S. Ghosh and N. K. Kishore, *IEEE Transactions on Dielectrics and Electrical Insulation* Vol. 6 No. 1, (1999) 131-134.

[138] S. Chakravorti and P. K. Mukherjee, *IEEE Transactions on Dielectrics and Electrical Insulation* Vol. 1 No. 2, (1994) 254-264.

[139] D. Guo, Y. Wang, C. Nan, L. Li, and J Xia, *Sensors and Actuators A, Phy* 102 (2002) 93–98.

RESEARCH PUBLICATIONS

1. M.S. Dash, J. Bera and S. Ghosh "Study on phase formation and sintering kinetics of $BaTi_{0.6}Zr_{0.4}O_3$ powder synthesized through modified chemical route," *J. Alloy. Comp*, 430 (2007), ***Elsevier***, PP. 212-216.
2. M.S. Dash, J. Bera and S. Ghosh "Electrical Properties of Undoped and Lanthanum Doped $BaTi_{0.6}Zr_{0.4}O_3$" ***IEEE*** *International conference on Industrial Technology* (ICIT) 2006, PP. 2993-2996, Dec 15-17, 2006.
3. M.S. Dash, J. Bera and S. Ghosh,"Effect of Porosity on Electrical Properties of Undoped and Lanthanum Doped $BaTi_{0.6}Zr_{0.4}O_3$" ***IEEE*** *International Conference on Solid Dielectrics (ICSD)*, PP. 281-284, July 8-13, 2007, UK.
4. M.S. Dash, J. Bera and S. Ghosh, "Diffuse phase transition of lanthanum doped $BaTi_{0.6}Zr_{0.4}O_3$" (Communicated).
5. M.S. Dash, S. Ghosh and J. Bera,"Application of Neural Network Technique to The Structural and Electrical Properties of Undoped and Lanthanum doped $BaTiZrO_3$" *International conference on polymeric materials in power engineering (ICPMPE)*, Oct 4-6, 2007, *Central Power Research Institute (CPRI)*, Bangalore, India.
6. M.S. Dash, S. Ghosh and J. Bera, "Microstructure-property correlation using ANN technique in lanthanum doped $BaTiZrO_3$" (In progress).